Microstructure and Small-Scale Deformation of $Al_{0.7}CoCrFeNi$ High-Entropy Alloy

Thesis by

Adenike M. Giwa

in Partial Fulfillment of the Requirement for

the Degree of

Doctor of Philosophy

CALIFORNIA INSTITUTE OF TECHNOLOGY

Pasadena, California

2019

(Defended, June 11, 2018)

Adenike M. Giwa

ORCID: 0000-0002-1229-7505

Acknowledgement

Firstly, I would like to thank my advisor Prof. Julia R. Greer for her patience, guidance and support. Her immense knowledge and advice helped me to keep on track and work at a smooth pace. I am also grateful to my committee members for their insightful comments and suggestions which have honed my research and critical thinking ability over the course of time.

My sincere thanks goes to the entire Greer group members for the knowledge sharing avenues especially the weekly group meetings. I am always intrigued to see science through diverse research projects. I am particularly grateful to Prof. Seok-Woo, Dr. Zach, Dr. Eric, Dr. David, Ottman, Jane and Anthony who helped with instrumentation, techniques, concepts and discussions for the successful completion of this work.

My appreciation goes to my collaborators; Prof. P.K. Liaw (University of Tennessee, Knoxville) for bulk sample fabrication and his *kind words*, Prof. K.A. Dahmen (University of Illinois, Urbana Champagne) for her data analysis, Dr. Z.H. Aitken, Dr. M. Jafary-Zadeh, and Dr. Y-W Zhang (Institute of High Performance computing, Singapore) for their modelling of the material system in this work. I am also grateful to Dr. C. Ma (Geology and planetary Science GPS, Caltech), C. Garland and Dr. M.S. Hunt (Kavli Nanoscience Institute KNI, Caltech) for utilizing their research expertise.

I would equally like to thank the Nigerian Government for the part funding of my Ph.D. under the Presidential Scholarship Scheme for Innovation and Development (PRESSID). My deep appreciation goes to Caltech, graduate office and Prof J.R. Greer for their financial support to ensure the successful completion of my Ph.D. program.

To my beloved husband, who is usually the first to listen to my ramblings, thank you for the encouragement all the way and my wonderful daughter, whose infectious smiles ease all worries, thanks for being there. To Mum, Dad and siblings, thanks for believing in me. I won't fail to appreciate the Ayuba, Alabi, Medupin, Adelakun, Adams, Giwa (extended) families for their support and love. Though there was infrequent communication during this period but I am always glad to have you all. To crown it all, I am thankful to God for the completion of this work.

Abstract

Novel engineering materials are continuously being designed for structural applications, particularly for improved mechanical properties such as high strength, enhanced ductility, and great thermal stability. High entropy alloys (HEAs) as an emerging material can be distinguished from other metal systems as a five-or-more-component alloy in which the constituents are in equiatomic or near equiatomic proportions, thereby maximizing the configurational entropy.

This thesis is focused on understanding the microstructure of an aluminum-containing HEA in relation to its small-scale mechanical properties. Physical phenomena such as size-effect, slip sizes, temperature effect, crystallographic orientation effect, influence of interface, and small perturbations in atom motions are studied.

Uniaxial compression experiments were conducted on nanopillars fabricated from the individual phases (i.e. Face Centered Cubic (FCC) and Body Cubic Centered (BCC) present in the $Al_{0.7}$CoCrFeNi HEA. We observed the presence of a size-effect in both phases, with smaller pillars having substantially greater strengths compared with bulk and with larger sized samples. The size-effect power law exponent m in $\tau_y \propto D^{-m}$ for the BCC phase was -0.28, which is lower than that of most pure BCC metals, and the FCC phase had $m = -0.66$, which is equivalent to most pure FCC metals. These results are discussed in the framework of nano-scale plasticity and the intrinsic lattice resistance through the interplay of the internal (microstructural) and external (dimensional) size effects.

In addition to higher stresses observed at cryogenic temperature in both phases, the microstructural analysis of the deformed pillar via Transmission Electron Microscopy (TEM) showed that FCC pillars undergo deformation by planar-slip dislocation activities even at temperatures of 40 K. Bulk FCC HEAs have been studied to deform via twinning mechanism at low temperatures. The BCC phase, however, confirms dislocation–driven plasticity and twinning at 40 K. These results are explained from the intrinsic nature of the dislocation structure of both phases at low temperatures.

The effect of an ‘interphase’ in micron-sized HEA pillars was studied from different orientation configurations of the BCC | FCC phases. Slip transmission across the phases was observed in high symmetry orientation combination of both phases.

Configurations having a mixture of both low and high symmetry orientations vary in deformation mechanisms. We explain these findings in relation to crystal orientation effect of the combining half pillars, competing plastic mechanisms, dislocation – boundary interactions and how these findings correlate with their mechanical response.

Also, we conducted dynamic mechanical analysis on the FCC and BCC HEA nanopillars to reveal their damping properties. Higher storage modulus and damping factor values were observed in FCC and BCC the nanopillars. Storage Moduli in the nano-sized HEAs are a factor of 2 greater than both bulk BCC and FCC HEA counterparts. The difference is due to greater surface contribution of the external atoms in the small-sized HEAs.

Published content

[1] **A. M. Giwa**, P. K. Liaw, K. A. Dahmen, and J. R. Greer, "Microstructure and small-scale size effects in plasticity of individual phases of Al0.7CoCrFeNi High Entropy alloy," *Ext. Mech. Let*.,vol.8 pp.220–228 (2016). DOI: /10.1016/j.eml.2016.04.013

Contributions: A.M.G characterized bulk sample (SEM, EDS, EBSD and TEM), fabricated nano-sized specimens, performed compression experiments, analyzed data, and participated in the writing of the manuscript.

[2] **A. M. Giwa**, Z. H. Aitken, M. Jafary-Zadeh, P. K. Liaw, Yong-Wei Zhang, J. R. Greer, "Temperature effect on Small-scale deformation on the phases of $Al_{0.7}$CoCrFeNiHigh Entropy Alloy HEA" (Manuscript in preparation).

Contributions: A.M.G characterized bulk sample (SEM, EBSD and TEM), fabricated nano-sized specimens, performed compression experiments, analyzed data, and participated in the writing of the manuscript.

[3] **A. M. Giwa**, Z. H. Aitken, P. K. Liaw, Yong-Wei Zhang, J. R. Greer, "Effect of Phase boundary as an interface in small-scale deformation of $Al_{0.7}$CoCrFeNi HEA'' (Manuscript in Preparation).

Contributions: A.M.G characterized bulk sample (SEM and EBSD), fabricated micro-sized specimens, performed compression experiments, analyzed data, and participated in the writing of the manuscript.

Table of Contents viii

List of Tables

List of Figures

Chapter 1 . Introduction

1.1 Materials Development: High-Entropy Alloys

Metallic systems are continuously being developed for improved properties such as high yield strengths, enhanced ductility, good thermal properties, etc. for various technological applications, for example in aerospace, energy and nuclear engineering [1], [2], [3], [4]. Alloying and precipitate inclusion enhances these properties via several strengthening mechanisms, such as precipitation, solid solution, and grain boundary strengthening[5], [6].

Traditional or conventional alloying involves one or two elements with similar chemistries with either interstitial or substitutional alloying following the Hume-Rothery rule of solvent-solute mixing [7], [8], [9]. Aluminum, copper and nickel alloys have been studied extensively, and they show good properties such as high strength, workability, electrical conductivity, and corrosion resistance [10], [11]. However, limitation exists in the number of compositions that can be fabricated from these conventional alloys [1].

Cantor et al [12] explored multi-component alloys of the composition $Fe_{20}Cr_{20}Ni_{20}Mn_{20}Co_{20}$ which gave a single FCC structure while Yeh et al [13] also explored different combinations of several elements such as Cu, Ti, V, F, Ni, Zr, Al, Mo, Co, which showed improved properties in hardness and strength when more elements were added. The multi-component alloys had strengths about three times greater than Hastelloy C, Stellite 6 and Ti-6Al-4V. Simple crystal structures, FCC, BCC or a combination of both, were also observed depending on the combining elements. These studies were conducted

independently and published in 2004 and were later referred to as High-Entropy Alloys (HEAs) [12], [13].

High-entropy alloys are described as a relatively novel class of material which have multiple principal elements in equi-molar or near equi-molar ratios (5 to 35 molar % of each components) that form stable solid solutions because of the large mixing entropies [13]. The mixing entropy is represented as:

$$\Delta S_{mix} = -R\, c_i\, ln \sum c_i \qquad (1.1)$$

where R is 8.31J/K mol, and c_i is the molar concentration of the *i*th constituent metal. When the entropy is maximized and there is an equal molar concentration of each element, Eq. (1) becomes

$$\Delta S_{mix} = R\, ln\, N \qquad (1.2)$$

where N is the number of constituent metals. As the number of constituent metals increases, the entropy of mixing also increases.

Table 1: N vs increase in configurational entropy [14]

N	1	2	3	4	5	6	7	8	9	10	11	12	13
ΔS_{conf}	0	0.69 R	1.1 R	1.39R	1.61 R	1.79 R	1.95 R	2.08 R	2.2 R	2.3 R	2.4 R	2.49 R	2.57 R

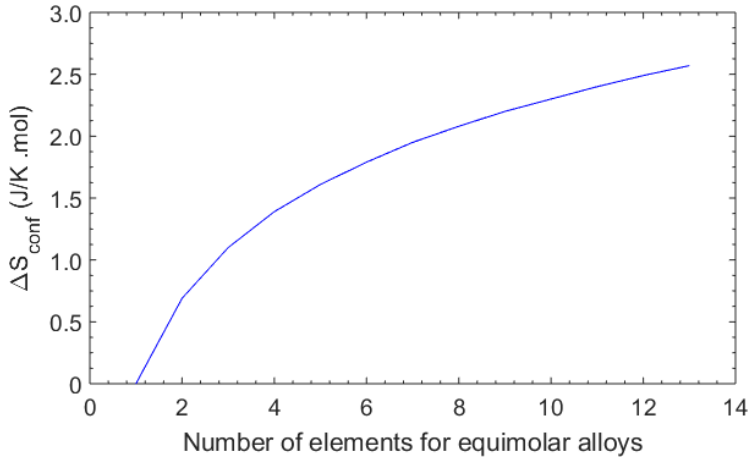

Figure 1.1: Plot of configurational entropy of multicomponent alloy versus the number of elements in alloys. This plot indicates a steady increase in configurational entropy from N = 5 [14].

Murty et al [14] discussed in their book, *High-Entropy Alloys* that conventional alloys have $\Delta S_{conf} \leq 1.5\,R$ based on entropy calculation of certain traditional alloys. HEAs have $\Delta S_{conf} \geq 1.5\,R$ when calculated for equiatomic constituents. This configurational entropy reduces as percentages of combining elements reduces. To establish a $\Delta S_{conf} \geq 1.5\,R$, constituent elements may exist in 5 to 35 molar percent.

Fig 1.1 and Table 1.1 show that there is a high increase in configurational entropy from 1.61 R to 1.79 R i.e. N = 5 to 6, which is an increase of 61%. Yeh et al [13], [15] established that beyond N = 13, the increase becomes minimal. Hence, it was suggested that HEAs can be defined as having 5 to 13 combining elements to maximize the increasing ΔS_{conf}.

High entropy alloys form simple crystal structures, a process which is a deviation from the Home-Rothery rule of solid solution alloy formation from similar combining elements, particularly their atomic size difference and crystal structure. It has been observed that the inclusion of Al, Ni which are FCC structures, enhances the formation of

the BCC crystal structure in the HEA [16], [17], [18]. The phase stability of HEA was predicted as that of a solid solution by relating the atomic size difference (δ), the enthalpy of mixing (ΔH_{mix}), and the configurational entropy ΔS_{conf} [16], [19] of the multi-component system. The atomic size difference (δ) is defined as

$$\delta = \sqrt{\sum_{i=1}^{N} c_i \left(1 - \left(r_i \,/\, \sum_{i=1}^{N} c_i \, r_i\right)\right)^2} \qquad (1.3)$$

Where r_i is the atomic radius of the ith component

$$\Delta H_{mix} = \sum_{i=1, i\neq j}^{N} (4\Delta_{mix}^{AB})\, c_i c_j \qquad (1.4)$$

Where $4\Delta_{mix}^{AB}$ is the mixing enthalpy of the binary (AB) alloy. A graphical representation in Figure 1.2 by Yang et al [20] combines these parameters to show how HEAs compare with other metallic systems.

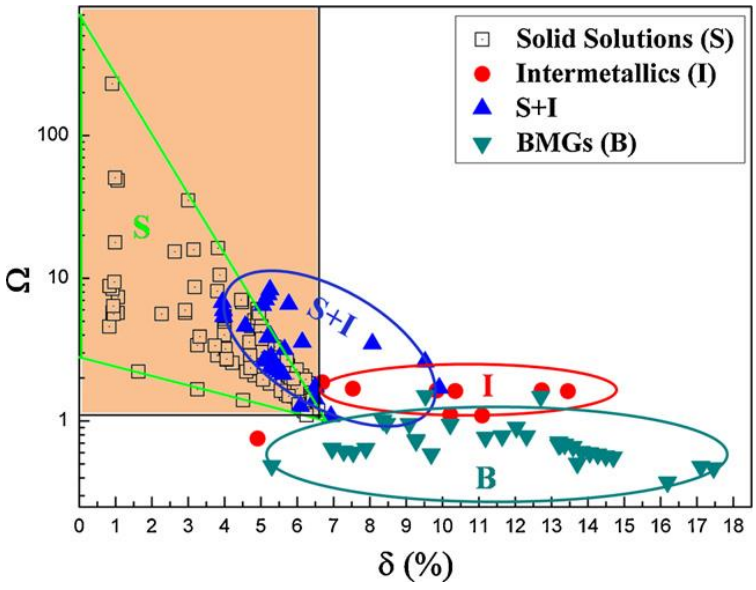

Figure 1.2: A graphical representation distinguishing HEAs from other metallic system by combining δ, ΔH_{mix} and ΔS_{conf} [20].

$$\Omega = \frac{T_m \, \Delta S_{conf}}{\Delta H_{mix}} \quad (1.5)$$

where T_m is the melting temperature. From Equation 1.5 and the graphical illustration above, it can be summarized that the quantitative criterion for the formation of a simple solid solution is -10 KJ/mol < ΔH_{mix} < 5 KJ/mol and δ< 4 % [2]. Apart from thermodynamically determining the phase stability, Guo et al [21] predicted the crystal structures of HEAs to be FCC and BCC based on the X-ray diffraction studies of some HEAs and suggested that the Valence Electron Concentration (VEC) can be used to predict the crystal structure. They discovered that where VEC < 6.8 corresponds to the BCC structure and VEC > 8.0 correlates with the FCC structure. The VEC is defined as:

$$VEC = \sum C_i \, (VEC_i) \quad (1.6)$$

where C_i is the atomic concentration of the *i*th element, and VEC_i is the VEC of the *i*th element. VEC counts the total number of electrons in the valence shell and for transition metals, accommodated in the valence band [27, 28].

HEAs have four core effects that set them apart from the conventional alloys. The core effects are high entropy effect, severe lattice distortion effect, sluggish diffusion effect, and cocktail effect [13], [19]. High entropy stabilizes the solid solution phase instead of complex phases such as intermetallics based on the principles of metallurgy. High entropy effect can be understood from multi-component alloys having medium ΔH_{mix} and highest ΔS_{conf} [14], [19], [22]. Enthalpy plays a role in the phase stability of HEAs, multi-component metallic system with systems having medium ΔH_{mix} causes unlike pairs in the solid solution, while systems with large positive ΔH_{mix} can lead to elemental phase separations, for example, in Cu- containing HEAs [14], [19], [22]–[24]. This further

indicates that the high entropy effect is essentially related to the interplay of enthalpy of mixing and configurational entropy.

The sluggish diffusion effect stems from the several interactions of the combining elements in the HEA. It was studied by Yeh et al that the diffusion rates in HEAs are the least when compared to stainless steel and pure metals [19], [25]. This can also be inferred by the formation of nanoprecipitates during nucleation and sometimes amorphous phases [19], [25].

Several principal elements have different atomic sizes occupying the lattice sites, and this leads to severe lattice distortions. It was observed in the XRD study of the individual combining metals of CuNiAlCoCrFeSi and the multi-principal alloy that decreasing XRD intensities occur as more principal elements were added. This is caused by deflections in the scattering [19]. These phenomena lead to the so-called cocktail effect, which is a result of inter-elemental interactions, composition change, and alloying [19], [26]. Improved properties of HEAs such as high strength and toughness, as well as high resistance to temperature, wear diffusion, radiation, and chemical reactions are observed. Figure 1.3 gives a summary of the core effects of the HEAs [22].

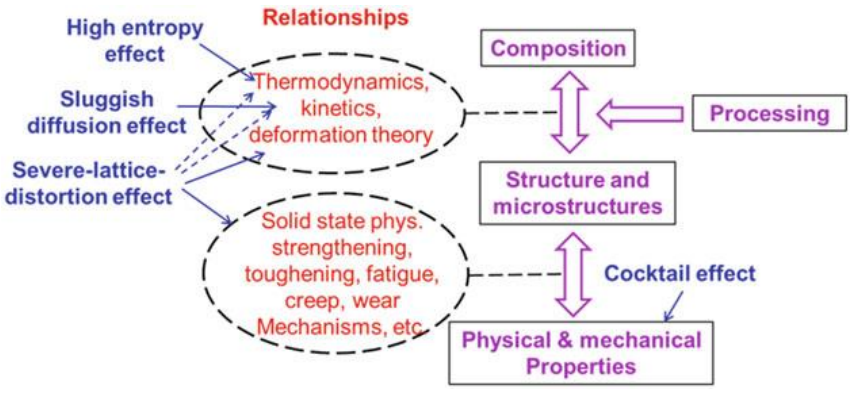

Figure 1.3: Schematic of the core effects of the HEAs [22].

In summary, the four core effects of HEAs: high entropy effect, related to its thermodynamics; the sluggish diffusion related to its kinetics; the severe lattice distortion related to its structure; and the cocktail effect sums the improved properties [25], [22].

HEAs are mostly classified based on their composition and functional properties. For example, the Al-containing HEAs are known to have single and/or dual phase microstructure. Refractory HEAs containing refractory metals such as Mo, Ta, Nb, W, etc. are also classified based on their functionalities. The illustration in Figure 1.4 below gives a layout of HEA classification based on their crystal structure [11]. Al-containing HEAs are flexible in adjusting their crystal structure; it is possible to vary the Al ratio in an alloy with other principal elements. Increasing the relative ratio of Al induces a larger lattice strain, and the ensuing distortion leads to relaxation via phase change in the crystal structure [13], [19], [27], [28], [29]. Figure 1.5 illustrates different Al-containing HEA systems and the lattice evolution associated with increase in Al ratio [28].

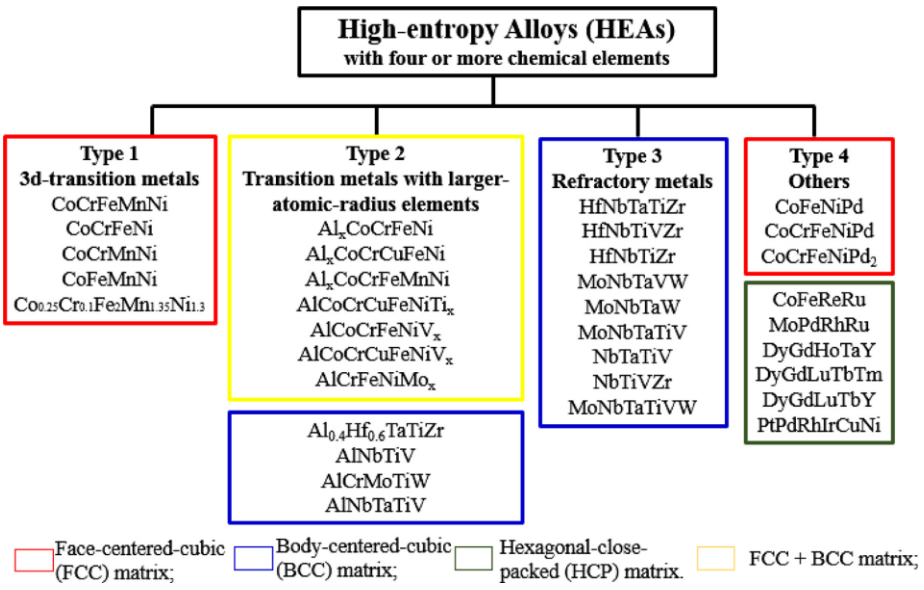

Figure 1.4: Classification of HEAs based on their crystal structure and compositions [11].

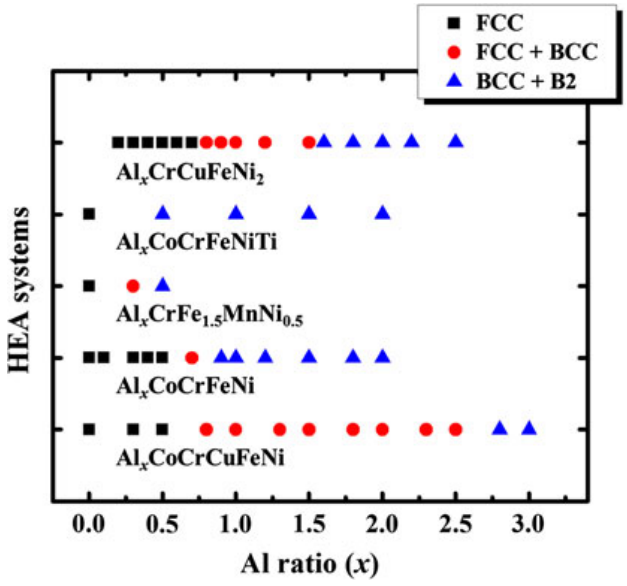

Figure 1.5: Al-containing HEA systems and the lattice evolution associated with increase in Al ratio [28].

In this thesis, we investigate the small-scale mechanical properties of $Al_{0.7}$CoCrFeNi HEA. The choice of HEA for this work stems from previous studies by Manzoni et al [23] and Singh et al [24], who observed that AlCoCrFeNi had no single element-rich phases, unlike its counterpart AlCoCrCuFeNi, thereby obscuring the possibility of the nanomechanical properties being studied as a function of a single element. Wang et al's high temperature XRD study of Al_xCoCrFeNi HEA (x = 0.1 to 2.0) concludes that when x = 0.7, i.e., HEA with the composition $Al_{0.7}$CoCrFeNi, there is a mixture of both the FCC and BCC phases, and the crystal structure does not change with increasing temperature [30], [17]. Therefore, $Al_{0.7}$CoCrFeNi is a strong candidate to study for the nanomechanical properties of each phase as a function of its composition.

1.2 Mechanical properties of metals and alloys

When force is applied to a material, deformation occurs and the mechanism is based on the intrinsic structure of the material relating to external influences [6]. These deformations enable the understanding of a material when used in real life or practical situations. Work hardening, i.e. strengthening under deformation, hardness, which is the resistance to penetration, tensile strengths, yield strength, elastic modulus, plastic deformation, ultimate strengths, and damping behavior are mostly used to characterized and quantify these deformations.

In crystalline metallic systems, the presence of defects such as vacancies, dislocation lines, interfaces, and voids enhance the ease of deformation [6], [5]. Without these defects, the theoretical strengths calculated in crystals are several orders of magnitude higher than strengths observed in experiments. The theoretical strength of a crystal was calculated by Frenkel using a sinusoidal function to be $\tau_{max} = \frac{G}{6}$, where G is the shear modulus. The elastic limit in which transition to plastic deformation can be defined as the yield strength (σ_y). 0.2% offset of the strain is usually taken for materials without sharp yield points.

The presence of dislocations, different grain sizes, and boundaries have been studied to understand crystal plasticity. Plasticity in crystalline materials can occur via slip as a result of dislocation motion as well as twinning when certain conditions such as low temperatures are introduced or a combination of slip and twinning. A critical stress value is required for plasticity to occur and this stress is unique to a specific plane. This is referred to as the Resolved Shear Stress RSS (τ).

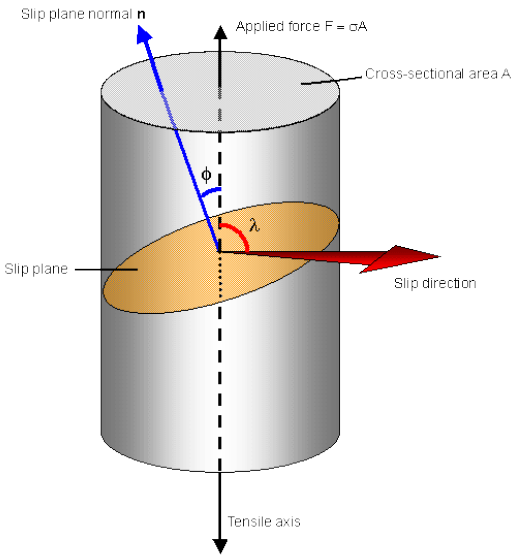

Figure 1.6: Geometry for resolving the shear component of a single crystal for tensile loading [31].

Figure 1.6 illustrates the geometry for calculating RSS which is obtained from the resolved force acting on the slip plane and the area of the slip plane. This is derived below as [31]:

$$\tau = \frac{resolved\ force\ acting\ on\ the\ slip\ plane}{area\ of\ the\ slip\ plane} = \frac{F\cos\lambda}{A\ /\cos\phi} = \frac{F}{A}\ cos\phi\cos\lambda$$

$$\tau = \sigma_y \cos\phi \cos\lambda \qquad (1.7)$$

where τ is the Resolved Shear Stress (RSS) in the slip plane and slip direction, σ_y is the yield strength, ϕ is the angle between the normal to the slip planes and the tensile axis, and λ is the angle between the tensile axis and the slip direction. $\cos\phi\cos\lambda$ is referred to as Schmid factor. Maximum shear stresses are obtained at ϕ and $\psi = 45°$.

Slip events occur on the slip plane that is most densely packed and in the most densely packed directions. FCC, BCC, HCP crystal structures have their unique slip systems for deformation. Slip bands are usually observed as a collection of slip lines, which are formed when dislocation lines reach the end of a crystal during deformation. The ease

of glide dislocation motion and cross slips of dislocations from one plane to another and the mobility of the screw and edge dislocations are characteristic phenomena attributed to the intrinsic dislocation structure of different crystal structures. During deformation, a change in stacking sequence can lead to the rearrangement of lattice structure. Half of the crystal lattice becomes a mirror image of the other half, a phenomenon known as twinning. In polycrystalline materials, deformation is governed by the crystal orientation, grain size, and grain boundary. The Resolved Shear Stress (RSS) plays a role in the yield, and crystals with higher RSS yield first. Grain boundaries serve as obstacles to slip, thereby enhancing work hardening and dislocation pile-ups. The Hall–Petch equation mathematically describes the relationship between strength and grain size:

$$\sigma_y = \sigma_0 + \frac{k_y}{\sqrt{d}} \qquad (1.8)$$

where σ_0 is the friction stress or resistance to glide, k_y is the measure of the degree of pile-ups in a boundary and d is the grain size. Equation 1.8 above indicates that as grain size reduces and the material strength increases, though a limit of 10 to 25 nm grain size has been established for this discontinuity in this phenomenon, which leads to another type of deformation called the grain boundary sliding [32].

Multi-component metallic systems are known to have higher strengths due to solid solution strengthening. Interactions occur between dislocations and solute atoms in slip planes and planes in close proximity. Dislocation motion is reduced, leading to increased lattice resistance which increases the overall yield strength of the system [5], [33].

High Entropy alloys as an interesting class of metallic system has shown superior mechanical properties as shown in Figure 1.7 due to the aforementioned four core effects.

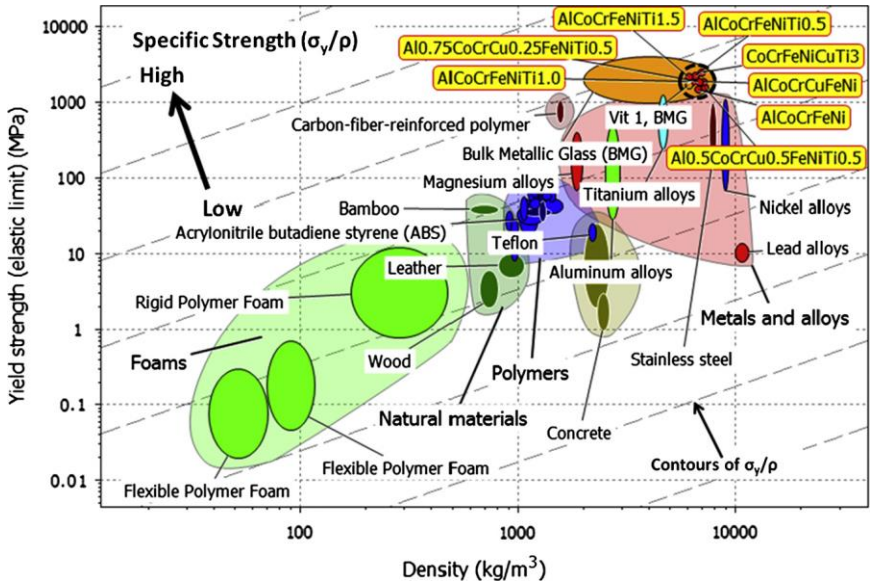

Figure 1.7: Materials property chart of engineering materials showing the HEAs on the top right of the chart with high yield strengths and high density.

CoCrFeNiTiAl, a BCC HEA has shown to have excellent mechanical properties at room temperature, a yield strength of 2.28 GPa and elastic modulus of 147.6 GPa [34]. Wu et al [35] studied the temperature dependence of FCC HEAs in comparison with Ni and observed yield strengths of the solid solution alloys greater than that of Ni by a factor of 3 to 5 at cryogenic temperatures. They related this to thermal influences in dislocation width [35]. At 77 K, the CrMnFeCoNi gave a fracture toughness of 200 MPa.m$^{1/2}$, indicative of exceptional damage tolerance. Generally, FCC HEAs are known to undergo dislocation to twinning transition during deformation as the temperature reduces to 77 K [36]. At elevated temperatures up to 873 K, it was observed by Senkov et al [37] that TaNbHfZrTi refractory HEA had a temperature-independent strain hardening with good ductile behavior. Diao et al summarized that FCC HEAs have similar yield strengths with conventional alloys such as Haynes 230, Hastealloy X alloy, Inconel alloy 600, and type 304 stainless steel [11]. Al-

containing HEAs and refractory HEAs are generally known for improved mechanical properties.

In this thesis, our focus is to understand deformation mechanism of HEAs at the nanoscale, particularly by comparing them with pure metals with a focus on yield strength, size effect, and strain hardening.

1.3 Small-scale mechanical behavior

Mechanical properties of small-scale materials are different from their bulk counterparts. To understand this phenomenon in single crystals, the flow stresses are converted to shear stresses and normalized with shear modulus. This is then related to the pillar diameter of the specimen and normalized by the Burgers vector. A power law relationship is established as:

$$\frac{\tau}{G} = A\left(\frac{D}{b}\right)^{-m} \tag{1.9}$$

where τ is the RSS, G is the shear modulus, D is the pillar diameter, and m is the size effect exponent. Figure 1.8 shows the size dependence plot $\tau/G \ vs \ D/b$ plot for commonly studied FCC metals (Cu, Al, Au, Ni), size effect has an exponent of m = 0.66 which is universal for all FCC metals [38] [39].

Dislocation starvation at the onset of plasticity and subsequent nucleation have been described as the two mechanisms governing the deformation in FCC single crystals, which leads to higher stresses [6], [38]. As initial dislocations leave the pillar, dislocation nucleation is required for plasticity to occur. Dislocation annihilation to the free surface causes discrete strain burst in the sample surface. This universal size effect is attributed to the ease of glide dislocation motion in the FCC single crystals.

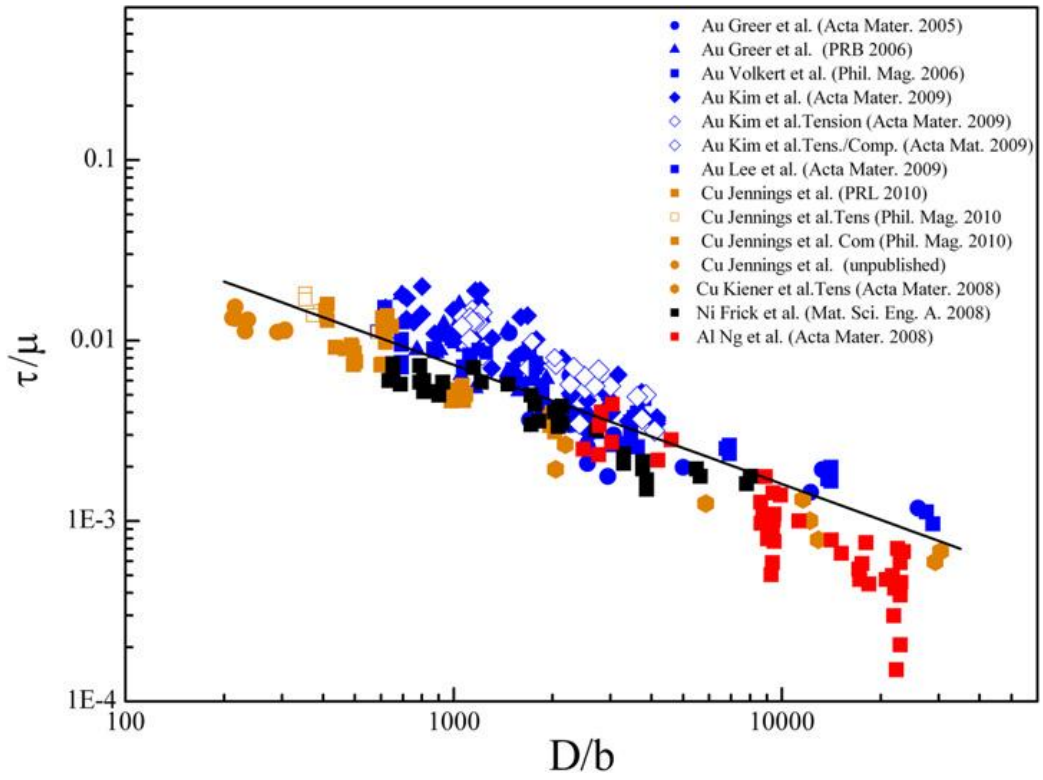

Figure 1.8 showing the universal scaling of commonly studied FCC single crystals [38].

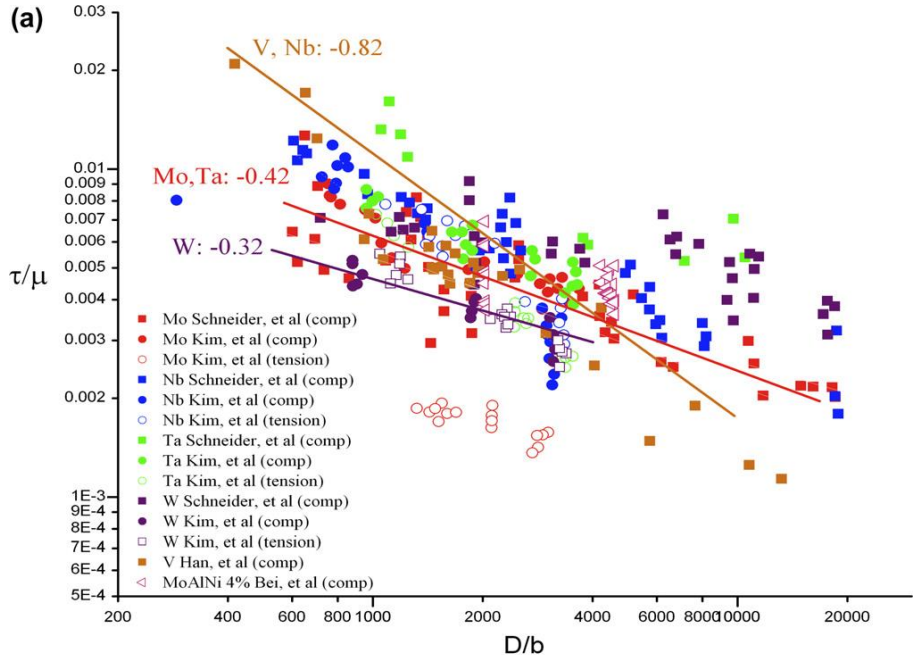

Figure 1.9 shows the size effect scaling of commonly studied BCC single crystals [38].

BCC single crystals also exhibit the 'smaller is stronger' size effects but have a more complex nanoplasticity mechanism. In this type of crystal structure, individual dislocations can form kinks, with each component interacting with one another, forming junctions, all of which lead to greater dislocation densities, sessile junctions, and forest-like hardening upon the application of force [40], [41]. Figure 1.9 shows the size dependence plot $\tau/G \ vs \ D/b$ plot for commonly studied BCC metals (V, Nb, Mo, Ta, W). The size effect exponent *m* vary from 0.21 to 0.93 [38]. This variation of size- effect in the BCC metals is attributed to the differences in the Peierls barrier and the critical temperature of the BCC single crystals [38], [40], [41]. BCC metals with lowest Peierls barrier and critical temperatures close to room temperatures have a high size effect exponent *m* such as Nb, m = 0.93 [42] and for V, m = 0.79 [43]. W and Mo have been reported to have reduced size dependence of m = 0.21 [42] and 0.44 [44], respectively, which is directly related to the higher Peierls barrier [38].

1.4 Small-Scale mechanical testing

Structural integrity is important in all devices, particularly in small-scale devices such as NEMS/MEMS since their properties are size dependent [45]. Small-scale testing is essentially important for designing or tailoring macroscopic properties of materials with their microstructural variables [46]. Nanomechnanical testing of metals and alloys can be used to investigate discrete events during the deformation process, for example, events like onset of plasticity which may be denoted from pop-in or pop-out behavior [47].

Generally, sub-microscale specimen can be fabricated using different approaches such as lithography, deposition, etching, and micromachining techniques [48]. Most metallic specimens are fabricated using the Focused Ion Beam (FIB), in which the Ga^+

source at high current is used to mill or etch away the surface of the bulk material; different patterns can be used to achieve the desired specimen geometry. Specimen damage by FIB fabrication process has been reported in several metals specimen due to Ga^+ implantation within 20 - 60 nm of the specimen depth [49], [50], [51]. It has been reported that the microstructure of the specimen controls the mechanism of deformation and not the fabrication techniques [52], [53]. Small-scale metallic specimens can also be fabricated using e-beam lithography by patterning PMMA resist and subsequently metal electrochemical deposition into the resist template [53], [54].

Most small-size crystalline alloys are fabricated using the FIB milling process described above and not via electrochemical deposition due to different deposition rates of the combining elements and also the formation of amorphous alloys. Zou et al [55] was successful in fabricating polycrystalline small-sized HEAs using the co-sputtering technique and Ion-Beam Assisted Deposition (IBAD) of the HEA films.

For small-scale mechanical testing, ex-situ or in-situ approaches can be used. For the ex-situ testing, uniaxial compression tests were carried out in a nanoindenter (Triboscope, Hysitron Inc.) equipped with the transducer (connecting the diamond tip) and optical lens. This set-up functions using a tip to optical lens calibration to ensure precise location of the specimen in the bulk material during experiments.

The nanomechanical experiments can also be performed using an in-situ vacuum set-up, Scanning Electron Microscope (SEM) can be used to aid visualization during the experiment as well as understand certain deformation events. The indenter as the nanomechanical equipment can be mounted to a port on the SEM. This set up can be also used for contact stiffness measurements during testing [56].

1.5 Objective and outline

This thesis is focused on understanding the microstructure and small-scale mechanical properties of a new class of metallic system (High-Entropy Alloys or HEAs) which has shown superior and unusual properties at the bulk scale.

In Chapter 3, we analyzed the microstructure of $Al_{0.7}$CoCrFeNi using several microscopic techniques such as the Scanning Electron Microscope (SEM); to probe surface features with emphasis on feature dimensions such as width and forms for example, the presence or and absence of nanoprecipitates in the multiphase system. Electron Back Scatter Diffraction (EBSD), and Transmission Electron Microscopy (TEM) were also conducted for a detailed understanding of the material system to include; the phases identification, lattice parameters calculation and crystallographic orientation mapping. These microstructures were further related to their chemistries by probing their elemental composition. The small-scale mechanical properties of the individual phases of $Al_{0.7}$CoCrFeNi HEA were probed to show their distinct behavior such as strength, size effect, strain hardening. These differences were explained in relation to their intrinsic microstructure, i.e. lattice resistance and extrinsic factor, which is size.

Chapter 4 focuses on the effect of cryogenic temperatures on the individual phases of the HEA. Increased strengths, reduced work hardening, and longer bursts regimes were observed. The size effect investigated at low temperatures differs from commonly studied metals. The BCC phase shows an isothermal size effect which stems from minimal or no effect of temperature on Peierls barrier, while the size effect of the FCC phase at cryogenic temperature reveals more contributions from the Peierls stress explained from the contraction of the dislocation line width. We also investigated that the microstructural

analysis of the deformed pillars via TEM shows distinct deformation mechanisms of both phases. Dislocation driven plasticity occurs in the FCC at all the temperatures studied while the BCC phase undergoes additional twinning deformation at 40 K.

Chapter 5 focuses on the effect of phase boundary on the mechanical response of vertically aligned bi-phase pillars of different combining orientations of the BCC and FCC half-pillars. We observed slip transmission from the FCC to the BCC in the high symmetry bi-phase configuration. It is suggested that the boundary serves as no impedance to dislocations motion. We observed different mechanical responses from the low/high orientation configurations of the bi-phase pillars and this is explained in the framework of single crystal orientation effect on the mechanical properties and competing contribution of the different dislocation structure to plasticity as they undergo simultaneous deformation.

Finally in Chapter 6, we focus on understanding the damping capacity of nano-sized HEAs. The storage modulus and loss tangent significantly increased when compared to the bulk counterparts. This is explained in relation to surface contribution to atoms motion and the effect on dislocation pinning points.

References

[1] S. Chikumba and V. V. Rao, "High Entropy Alloys: Development and Applications," *7th Int. Conf. Latest Trends Eng. Technol. Nov. 26-27, 2015 Irene, Pretoria (South Africa)*, pp. 1–5, 2015.

[2] Y. F. Ye, Q. Wang, J. Lu, C. T. Liu, and Y. Yang, "High-entropy alloy: challenges and prospects," *Mater. Today*, vol. 19, no. 6, pp. 349–362, 2016.

[3] S. Praveen and H. S. Kim, "High-Entropy Alloys: Potential Candidates for High-Temperature Applications - An Overview," *Adv. Eng. Mater.*, vol. 1700645, pp. 1–22, 2017.

[4] D. Miracle, J. Miller, O. Senkov, C. Woodward, M. Uchic, and J. Tiley, "Exploration and Development of High Entropy Alloys for Structural Applications," *Entropy*, vol. 16, no. 1, pp. 494–525, 2014.

[5] T. H. Courtney, *Mechanical behavior of materials*. Waveland Press, 2005.

[6] J. Pelleg, "Mechanical properties of materials," *Solid Mech. its Appl.*, vol. 190, pp. 1–634, 2013.

[7] W. Callister and D. Rethwisch, *Materials science and engineering: an introduction*, vol. 94. 2007.

[8] "Solid Solutions: The Hume-Rothery Rules." [Online]. Available: http://www.phase-trans.msm.cam.ac.uk/2004/titanium/hume.rothery.html. [Accessed: 12-Apr-2018].

[9] "Solid Solutions:The Hume Rothery Rules" http://www.nptel.ac.in/courses/113106032/8%20-

%20Solid%20Solutions.pdf
[10] "Aluminum Alloys 101 | The Aluminum Association." [Online]. Available: http://www.aluminum.org/resources/industry-standards/aluminum-alloys-101. [Accessed: 12-Apr-2018].
[11] H. Y. Diao, R. Feng, K. A. Dahmen, and P. K. Liaw, "Fundamental deformation behavior in high-entropy alloys: An overview," *Current Opinion in Solid State and Materials Science*, vol. 21, no. 5. pp. 252–266, 2017.
[12] B. Cantor, I. T. H. Chang, P. Knight, and A. J. B. Vincent, "Microstructural development in equiatomic multicomponent alloys," *Mater. Sci. Eng. A*, vol. 375–377, no. 1–2 SPEC. ISS., pp. 213–218, 2004.
[13] J. W. Yeh, S. K. Chen, S. J. Lin, J. Y. Gan, T. S. Chin, T. T. Shun, C. H. Tsau, and S. Y. Chang, "Nanostructured high-entropy alloys with multiple principal elements: Novel alloy design concepts and outcomes," *Adv. Eng. Mater.*, vol. 6, no. 5, p. 299–303+274, 2004.
[14] B. S. Murty, J.W. Yeh, S. Ranganathan, "*High-Entropy Alloys*." Elsevier (2014).
[15] J. Yeh, "Alloy Design Strategies and Future Trends in High-Entropy Alloys," vol. 65, no. 12, pp. 1759–1771, 2013.
[16] S. Guo and C. T. Liu, "Phase stability in high entropy alloys : Formation of solid-solution phase or amorphous phase," *Prog. Nat. Sci. Mater. Int.*, vol. 21, no. 6, pp. 433–446, 2011.
[17] W.-R. Wang, W.-L. Wang, S.-C. Wang, Y.-C. Tsai, C.-H. Lai, and J.-W. Yeh, "Effects of Al addition on the microstructure and mechanical property of AlxCoCrFeNi high-entropy alloys," *Intermetallics*, vol. 26, pp. 44–51, 2012.
[18] H. R. Sistla, J. W. Newkirk, and F. Frank Liou, "Effect of Al/Ni ratio, heat treatment on phase transformations and microstructure of AlxFeCoCrNi2−x (x=0.3, 1) high entropy alloys," *Mater. Des.*, vol. 81, pp. 113–121, 2015.
[19] Y. Zhang, T. T. Zuo, Z. Tang, M. C. Gao, K. A. Dahmen, P. K. Liaw, and Z. P. Lu, "Microstructures and properties of high-entropy alloys," *Prog. Mater. Sci.*, vol. 61, no. October 2013, pp. 1–93, Apr. 2014.
[20] X. Yang and Y. Zhang, "Prediction of high-entropy stabilized solid-solution in multi-component alloys," *Mater. Chem. Phys.*, vol. 132, no. 2–3, pp. 233–238, 2012.
[21] S. Guo, C. Ng, J. Lu, and C. T. Liu, "Effect of valence electron concentration on stability of fcc or bcc phase in high entropy alloys," *J. Appl. Phys.*, vol. 109, no. 10, pp. 0–5, 2011.
[22] M. C. Gao, P. K. Liaw, J.-W. Yeh, and Y. Zhang, *High-entropy alloys: Fundamentals and applications*. 2016.
[23] A. Manzoni, H. Daoud, R. Völkl, U. Glatzel, and N. Wanderka, "Phase separation in equiatomic AlCoCrFeNi high-entropy alloy.," *Ultramicroscopy*, vol. 132, pp. 212–5, Sep. 2013.
[24] S. Singh, N. Wanderka, B. S. Murty, U. Glatzel, and J. Banhart, "Decomposition in multi-component AlCoCrCuFeNi high-entropy alloy," *Acta Mater.*, vol. 59, no. 1, pp. 182–190, 2011.
[25] J. W. Yeh, "Recent progress in high-entropy alloys," *Ann. Chim. Sci. des Mater.*, vol. 31, no. 6, pp. 633–648, 2006.
[26] M.-H. Tsai and J.-W. Yeh, "High-Entropy Alloys: A Critical Review," *Mater. Res. Lett.*, vol. 2, no. 3, pp. 107–123, 2014.
[27] W. Guo, W. Dmowski, J.-Y. Noh, P. Rack, P. K. Liaw, and T. Egami, "Local Atomic Structure of a High-Entropy Alloy: An X-Ray and Neutron Scattering Study," *Metall. Mater. Trans. A*, vol. 44, no. 5, pp. 1994–1997, 2012.
[28] Z. Tang, M. C. Gao, H. Diao, T. Yang, J. Liu, T. Zuo, Y. Zhang, Z. Lu, Y. Cheng, Y. Zhang, K. a. Dahmen, P. K. Liaw, and T. Egami, "Aluminum alloying effects on lattice types, microstructures, and mechanical behavior of high-entropy alloys systems," *Jom*, vol. 65, no. 12, pp. 1848–1858, 2013.
[29] T. Egami and Y. Waseda, "Atomic size effect on the formability of metallic glasses," *J. Non. Cryst. Solids*, vol. 64, no. 1–2, pp. 113–134, 1984.
[30] W. R. Wang, W. L. Wang, and J. W. Yeh, "Phases, microstructure and mechanical properties of AlxCoCrFeNi high-entropy alloys at elevated temperatures," *J. Alloys Compd.*, vol. 589, pp. 143–152, 2014.
[31] "DoITPoMS - TLP Library Slip in Single Crystals - Slip geometry." [Online]. Available: https://www.doitpoms.ac.uk/tlplib/slip/slip_geometry.php. [Accessed: 11-May-2018].
[32] X. W. Gu, C. N. Loynachan, Z. Wu, Y. W. Zhang, D. J. Srolovitz, and J. R. Greer, "Size-dependent deformation of nanocrystalline Pt nanopillars," *Nano Lett.*, vol. 12, no. 12, pp. 6385–6392, 2012.

[33] M. F. Ashby and D. R. H. Jones, *Engineering Materials 1*. 2012.
[34] K. B. Zhang, Z. Y. Fu, J. Y. Zhang, W. M. Wang, H. Wang, Y. C. Wang, Q. J. Zhang, and J. Shi, "Microstructure and mechanical properties of CoCrFeNiTiAlx high-entropy alloys," *Mater. Sci. Eng. A*, vol. 508, no. 1–2, pp. 214–219, 2009.
[35] Z. Wu, H. Bei, G. M. Pharr, and E. P. George, "Temperature dependence of the mechanical properties of equiatomic solid solution alloys with face-centered cubic crystal structures," *Acta Mater.*, vol. 81, pp. 428–441, 2014.
[36] B. Gludovatz, "No Title," vol. 1153, 2014.
[37] O. N. Senkov, J. M. Scott, S. V. Senkova, F. Meisenkothen, D. B. Miracle, and C. F. Woodward, "Microstructure and elevated temperature properties of a refractory TaNbHfZrTi alloy," *J. Mater. Sci.*, vol. 47, no. 9, pp. 4062–4074, 2012.
[38] J. R. Greer and J. T. M. De Hosson, "Plasticity in small-sized metallic systems: Intrinsic versus extrinsic size effect," *Prog. Mater. Sci.*, vol. 56, no. 6, pp. 654–724, 2011.
[39] R. Dou and B. Derby, "A universal scaling law for the strength of metal micropillars and nanowires," *Scr. Mater.*, vol. 61, no. 5, pp. 524–527, 2009.
[40] J. R. Greer, C. R. Weinberger, and W. Cai, "Comparing the strength of f.c.c. and b.c.c. sub-micrometer pillars: Compression experiments and dislocation dynamics simulations," *Mater. Sci. Eng. A*, vol. 493, no. 1–2, pp. 21–25, 2008.
[41] S. Brinckmann, J. Y. Kim, and J. R. Greer, "Fundamental differences in mechanical behavior between two types of crystals at the nanoscale," *Phys. Rev. Lett.*, vol. 100, no. APRIL, pp. 1–4, 2008.
[42] J. Y. Kim, D. Jang, and J. R. Greer, "Tensile and compressive behavior of tungsten, molybdenum, tantalum and niobium at the nanoscale," *Acta Mater.*, vol. 58, no. 7, pp. 2355–2363, 2010.
[43] S. M. Han, T. Bozorg-Grayeli, J. R. Groves, and W. D. Nix, "Size effects on strength and plasticity of vanadium nanopillars," *Scr. Mater.*, vol. 63, no. 12, pp. 1153–1156, 2010.
[44] a. S. Schneider, C. P. Frick, P. a. Gruber, R. Mönig, O. Kraft, E. Arzt, D. Kaufmann, B. G. Clark, C. P. Frick, P. a. Gruber, R. Mönig, O. Kraft, and E. Arzt, "Correlation between critical temperature and strength of small-scale bcc pillars," *Phys. Rev. Lett.*, vol. 103, no. 10, pp. 1–4, 2009.
[45] B. Bhushan, *Nanotribology and Nanomechanics: An Introduction: Fourth Edition*. 2017.
[46] A. C. Fischer-Cripps, *Nanoindentation*. 2011.
[47] A. Tiwari, *Nanomechanical Analysis of High Performance Materials*, vol. 203. 2014.
[48] "Chapter 4 MICROSYSTEM FABRICATION PROCESSES," pp. 71–91.
[49] D. Drobne, M. Milani, V. Lešer, and F. Tatti, "Surface damage induced by FIB milling and imaging of biological samples is controllable," *Microsc. Res. Tech.*, vol. 70, no. 10, pp. 895–903, 2007.
[50] F. Machalett, K. Edinger, J. Melngailis, M. Diegel, K. Steenbeck, and E. Steinbeiss, "Direct patterning of gold oxide thin films by focused ion-beam irradiation," *Appl. Phys. A Mater. Sci. Process.*, vol. 71, no. 3, pp. 331–335, 2000.
[51] J. R. Greer, W. C. Oliver, and W. D. Nix, "Size dependence of mechanical properties of gold at the micron scale in the absence of strain gradients," *Acta Mater.*, vol. 53, no. 6, pp. 1821–1830, 2005.
[52] X. Ni, S. Papanikolaou, G. Vajente, R. X. Adhikari, and J. R. Greer, "Probing Microplasticity in Small-Scale FCC Crystals via Dynamic Mechanical Analysis," *Phys. Rev. Lett.*, vol. 118, no. 15, pp. 1–6, 2017.
[53] A. T. Jennings, M. J. Burek, and J. R. Greer, "Microstructure versus Size: Mechanical properties of electroplated single crystalline Cu nanopillars," *Phys. Rev. Lett.*, vol. 104, no. 13, 2010.
[54] M. J. Burek and J. R. Greer, "Fabrication and microstructure control of nanoscale mechanical testing specimens via electron beam lithography and electroplating," *Nano Lett.*, vol. 10, no. 1, pp. 69–76, 2010.
[55] Y. Zou, H. Ma, and R. Spolenak, "Ultrastrong ductile and stable high-entropy alloys at small scales," *Nat. Commun.*, vol. 6, 2015.
[56] "InSEM Systems." [Online]. Available: http://nanomechanicsinc.com/insem-systems-page/. [Accessed: 18-Apr-2018].

Chapter 2 . Methodology

2.1 Microscopic techniques

2.1.1 Optical Microscopy

Optical microscopy functions by the transmission of light through a material or reflection of light from a material surface. Objects are usually placed in the focal plane of a lens. In metallic materials, optical microscopes are used for preliminary evaluation of a material surface to determine surface roughness and whether the sample can be evaluated with other microscopic techniques requiring flat surfaces to determine other microstructural features. It is mostly used at mechanical polishing intervals for metal and alloys and comes in handy for quick analysis. It gives a general overview of a material, though limitations exist due to the resolution limit of submicron particles approaching the wavelength of visible light (400 to 700 nm) [1]. The Keyence high-speed microscope was used in our preliminary studies.

2.1.2. Scanning Electron Microscopy (SEM)

This microscopic technique works at very small wavelengths (3.7 pm at 100 KeV) [2] and electrons are deflected by a magnetic field. Electrons interact with particles of the material, and several characteristic signals such as backscattered electrons, secondary electrons, x-rays, etc. are obtained. These signals can be used to get a further understanding of the material structure by coupling with appropriate detectors. The backscatter electrons are high energy electrons reflected from the sample surface via elastic scattering. This is useful for phase contrast analysis due to atomic size contrasts of different elements. The secondary electrons are low energy electrons obtained from few nanometers interaction

with the sample surface via inelastic scattering. Imaging with this technique ensures a better surface topography. Consequently, very small surface features can be identified, such as grain boundaries, pore, voids, inclusions, precipitates, etc.

SEMs can be used to study surface morphology and topography of materials at a resolution of 10 nm. It is therefore an essential tool for texture analysis. In this study, the ZEISS SEM coupled with a Back-Scatter detector and the FEI dual beam SEM coupled with the secondary electron detectors were used.

2.1.3 Energy Dispersive Spectroscopy (EDS)

The energy dispersive spectroscopy (EDS) technique is usually coupled with the SEM to evaluate the elemental composition of a material. Characteristic X-ray signals unique to individual elements are obtained from the SEM and this can be used to probe elemental constituents in a material, either by line scans, mapping, or point analysis at specific sites. The ZEISS SEM coupled with Oxford INCA 300 X-ray Energy Dispersive Spectrometer (EDS) was used in this study.

2.1.4 Electron Back-Scatter Diffraction (EBSD)

The EBSD technique is used to identify the phase information (crystal structure identification) and crystallographic orientation of a material system. Very flat or polished material is required with this technique because signals are obtained via diffraction of the planes. This allows interplanar distances of planes to be calculated based on Bragg's conditions and lattice parameters already obtained from x-ray diffraction. The orientations of a crystal can thus be identified. This allows for orientation mapping of a large area as well as specific features in a material. This technique is mostly coupled with statistical

tools to help analyze disorientation angles between different grains, grain size distribution, texture analysis of a material after mechanical analysis, slip/lattice rotation, etc. The orientation mapping in this study was done using the ZEISS SEM coupled with HKL EBSD system.

2.1.5 Transmission Electron Microscopy (TEM)

The TEM is an electron microscope useful for probing intrinsic structures, additional phases, deformation behavior, etc. Electrons are transmitted through a very thin piece of materials usually less than 200 nm in thickness. It can be used for imaging and taking diffraction patterns to confirm poly crystalline, single crystalline or amorphous nature of a material. Different diffraction modes are possible such as Bright Field (BF) and Dark Field (DF). The Bright Field (BF) TEM requires introducing the objective aperture to the back focal plane of the objective lens allowing direct beam while the Dark Field (DF) prevents the direct beam from passing through, giving rise to a different contrast. High-resolution TEM (HRTEM) images can also be obtained to show the atomic arrangements in their lattice planes. Resolutions less than 0.16 nm can be seen, which allows lattice spacing to be calculated, and interfaces between crystals can also be studied. The EDS can also be coupled with the TEM for elemental information of a material. The TEM analysis was done using the FEI Tecnai F30 with 300 KeV accelerating voltage.

2.2 Small-Sized Sample Fabrication

For small-scale mechanical experiments, we fabricated nanopillars from the identified phases of the HEA using the FEI Versa 3D dual beam SEM/FIB. The pillar fabrication via Focused Ion Beam (FIB) milling was first utilized by Uchic et al [3] by making concentric circular milling patterns until the desired cylindrical specimen

dimension of aspect ratio (pillar height to diameter) of 3:1 is achieved. The milling is done using Ga^+ source to etch out the surface of the material. A voltage of 30 KV and a current of 5 nA is maintained for the first rough cut. The voltage is maintained to the final cut, but the current is gradually reduced as the finishing steps are reached to prevent excessive surface damage. For smaller specimens, 10 pA was used for the final cut.

In the SEM chamber, the sample is tilted normal to the ion beam source which is 52^0 from the electron beam gun. Imaging from the SEM is possible while milling is being done. TEM sample fabrication was done via using nanomanipulator probe associated with the FEI Versa dual beam SEM/FIB. Pt is deposited on the site of interest, and subsequent bulk milling on the sides of the region of interest is done to ensure a lift-out on to the TEM grid posts via the probe. Thinning of the sample on the TEM grid is done using FIB to a thickness of ~ 60 nm.

2.3 Mechanical experiments

2.3.1 Compression methodology

The uniaxial compression experiments were done in a nanoindenter (Hysitron TI-950 triboindenter), which functions using a three-axes piezo-scanner which enables X, Y, and Z stage movement while aided by an optical microscope to monitor the approach of the probe to the sample. The transducer assembly is made of the three-plate capacitive force-displacement transducer and voltage measurements are used to determine the force or displacements during a test. The entire system is kept in an acoustic enclosure to minimize noise and to reduce thermal drift [4]. The triboindenter is equipped with an 8 μm diamond flat punch. Experiments were conducted in a displacement-rate-controlled mode at a constant prescribed strain rate of 10^{-3} s^{-1} to a final total strain of 15% of the pillar

height.

Cryogenic experiments were done using in-situ nanomechanical setup developed by Lee et al [5]. The setup incorporates the FEI Quanta SEM, the nanoindenter (INSEM^{TM}) from Nanomechanics Inc. and the cryogenic assembly by Janis Research Company. The nanoindenter is used in vacuum and onstage with the cryogenic system has a vacuum transfer line that can be connected to both the liquid Helium or liquid Nitrogen to induce the low temperature for the experiments. This cryogenic assembly is also equipped with a temperature controller with thermocouples to read the temperature at the cold finger entry to the SEM chamber and at the sample stage. Room temperature experiments were conducted by removing the cryo-assembly from the set-up. A detailed explanation is described by Lee et al [5].

A constant temperature of ~143 K was achieved after 3 hours of releasing the liquid nitrogen through the transfer line to the SEM chamber and at temperature of ~ 40 K after about 2.5 hours of liquid He. The flow rate of liquid Ni/He into the SEM chamber controls the time at which the desired temperature is achieved. It is preferred to set an intermediate flow rate to prevent having excessive amounts of gases in the chamber, which could lead to fluctuations during the experiments, thereby causing noisy data. Conversely, an inadequate flow rate will prolong the time for the temperatures to be achieved.

The experiments were performed 2 hours after the desired temperature was reached. The in-situ nanomechanical set-up is equipped with a 5 μm tungsten carbide flat punch tip coated with gold (Au). The Au coating was used to prevent charging of the bulk sample for good in-situ SEM visualization. The experiments were done in displacement-rate-

controlled mode using a strain rate of 10^{-3} s^{-1} to a final total strain of 15 % of the pillar height.

2.3.2 Dynamic Mechanical analysis (DMA) Experiments

Dynamic mechanical experiments were performed using the Hysitron NanoDMA with in-situ drift corrections. Frequency sweep tests were conducted using an 8 μm flat punch. The experiments were conducted at a frequency range of 5 Hz to 20 Hz. This was done by superimposing a small sinusoidal force oscillation on top of a constant quasi-static force [6]. Displacement amplitudes, load amplitudes and phase angles were generated from the tests allowing us to calculate parameters such as storage modulus, loss modulus and tan delta, which defines the damping mechanisms of the HEA. Frequency sweep dynamic tests can be conducted as separate experiments for each frequency or multiple frequencies on a single experiment after certain wait times.

Quasi-static compression experiments were first conducted to determine the maximum load reached before plasticity. This is to ensure that the dynamic experiments were conducted in the elastic regime. The dynamic experiments were performed using the force-control mode to prescribe the oscillation force. These tests are site-specific, thus allowing us to work on the nanopillars fabricated from the individual phases of the bulk HEA while utilizing the Dynamic nanoindentation set-up in the Hysitron triboindenter.

References

[1]"MicroscopicTechniques,"*https://cw.fel.cvut.cz/wiki/_media/courses/a6m33zsl/microscopic_techniques.pdf.*

[2] "Introduction to Electron Microscopy - Advanced Microscopy - Imaging Facilities - The University of Utah." [Online]. Available:http://advancedmicroscopy.utah.edu/education/electron-micro/.

[3] M. D. Uchic, D. M. Dimiduk, J. N. Florando, and W. D. Nix, "Sample dimensions influence strength and crystal plasticity.," *Science*, vol. 305, no. 5686, pp. 986–9, Aug. 2004.

[4] HYSITRON, “TI 950 Triboindenter User Manual,” pp. 1–262, 2010.

[5] L. E. E. Seok-woo, C. Yintong, R. Y. U. Ill, G. J. R, S. W. Lee, Y. Cheng, I. Ryu, and J. R. Greer, “Cold-temperature deformation of nano-sized tungsten and niobium as revealed by in-situ nano-mechanical experiments,” *Sci. China Technol. Sci.*, vol. 57, no. 4, pp. 652–662, 2014.

[6] H. - Nanomechanical Test Instruments, “Continuous Nanoscale Dynamic Mechanical Analysis of PMMA - Utilizing the Power of nanoDMA® III with CMX and In-Situ Drift Correction.”

Chapter 3 . Microstructure and small-scale size effects in plasticity of individual phases of $Al_{0.7}CoCrFeNi$

3.1 Motivation

Microstructural characterization is very critical in new engineering materials since material properties are influenced by their microstructures. The processing history, performance, and properties of materials are usually interrelated to the microstructure. These microstructures may be described as the appearance of a material at the nano/micro length scale to determine the arrangement of phases and defects within the material. Apart from the surface appearance, internal structures that distinguish one material from the other can be defined as microstructure even at the atomistic level. Microstructural characterization in metallic systems is possible with the aid of various microscopic techniques. Polishing via mechanical and electrochemical routes aids the visibility of surface features.

To understand the structural properties of a new material system, it is important to probe the mechanical properties of the individual phases present in the bulk material. This can be achieved via nanomechanical experiments by probing the compressive strength of the single-crystalline small-scale samples fabricated from individual phases of an alloy, in this case $Al_{0.7}CoCrFeNi$ High-Entropy Alloy, and comparing the results with those of commonly studied pure Face-Centered Cubic (FCC) and Body-Centered Cubic metals of equivalent dimensions.

In this chapter, we focus on relating identified microstructures of $Al_{0.7}CoCrFeNi$ HEA to the mechanical properties of the individual phases. We discussed our findings in

the framework of nano-scale plasticity and the intrinsic lattice resistance through the interplay of the internal (microstructural) and external (dimensional) size-effects.

3.2 Sample Preparation of the Bulk $Al_{0.7}CoCrFeNi$ HEA

The vacuum arc melting technique was used for the fabrication of $Al_{0.7}CoCrFeNi$ HEA and this was done at the Department of Materials Science at the University of Tennessee, Knoxville. This involves heating using an electric arc between the tungsten electrode and the metals in a crucible in the copper hearth [1]. The melting is usually done in an argon atmosphere. A direct current (DC) powdered button melter with the copper mold was used in argon gas. The raw materials, Al, Co, Cr, Fe, and Ni powders of 99.9% purity in weight percent, were triple melted and formed into ~ 300 g button with a thickness of 10 mm. The as-cast buttons were heated in the vacuum furnace to 1250 ℃ for 2 hours and subsequently annealed at the same temperature for 50 hours to ensure homogenization. The samples were then cooled in the furnace down to room temperature. The homogenized buttons were embedded in carbon steel to avoid surface oxidation. The carbon steel was a 76 mm diameter Iron Pipe Size (IPS) tubing with a 3 mm thick wall. The tubing was flattened and then welded shut with the button inside. Then, the whole button was upset-forged without restriction to the four sides to achieve a 50% reduction in thickness at 1250 ℃. The final forged portion was ~ 5 mm thick.

Mechanical polishing was carried out using the Buehler EcoMet polisher, and alumina-lapping films were used by sequential polishing from 30 μm to 0.5 μm grit-size while running under water for removal of excess material. The sample surface was subsequently polished using Vibro polishing with silica suspension of particle size 0.05 μm. Due to the dense nature of the HEA, good surface features were not observed in the

optical and scanning electron microscope (SEM) and the final polishing was done via electrochemical route by Able Electropolishing Co.

3.3 Microstructural Characterization

3.3.1 Surface Features

Figure 3.1 (a-b) shows the microstructure of the as-forged electropolished $Al_{0.7}$CoCrFeNi HEA. The surface features were analyzed using the Keyence optical microscope (Fig. 3.1 (a)) and the ZEISS Scanning Electron Microscope (SEM) (Figure 3.1(b)), which utilized the backscatter detector to provide a general overview of the phase contrast. In both micrographs, we observe patterned phase contrast indicating two phases in a similar behavior found in the Widmanstätten structure commonly observed in Ni and Iron alloys [3]–[5]. On further magnification shown in Figure 3.1 (c), we observe a matrix - dendrite feature of the phases which is suggested to form via spinodal decomposition as a result of rapid unmixing during cooling. This phenomenon is prevalent in Al-containing HEAs and it has been studied to arise as Al ratio increases. The atomic % of Al in which spinodal decomposition occurs depends on the ratio of Al with the other combining metals [6]–[12].

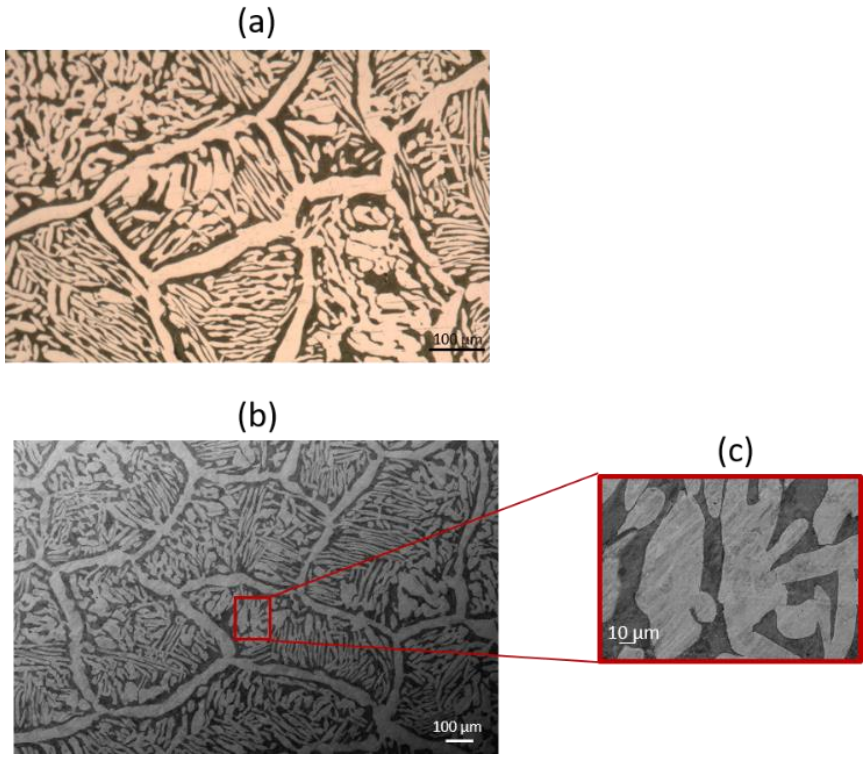

Figure 3.1 (a) shows the optical image of the $Al_{0.7}$CoCrFeNi HEA (b) the SEM image using the Back Scatter Detector (c) shows the magnified image showing the dendrites and interdendrites.

To get a detailed understanding of the dual-phase microstructure, we used the FEI versa 3D dual beam which couples the SEM and Focused Ion Beam (FIB) with the secondary electron detector with the sample stage tilted at 52^0. Figure 3.2 (a-b) shows the precise layout of the microstructure, which reveals the interdendrite region as the matrix into which the dendrites are embedded. Clear grain boundaries were observed in the matrix region. Each dendrite appears to be 10 –15 µm wide; on further magnification, we found the dendrites to contain nanoparticles that range from about 7 to 100 nm in diameter (Figure 3.2 (b)). The observed nanoprecipitates are a common feature observed in HEAs, and this feature is consistent with findings in [6], [13]–[18]. Surface relief across the phases was

also observed at good resolutions. The surface relief which is of few nanometers occurs as a result of the local material flow with the interface boundary [19], [20].

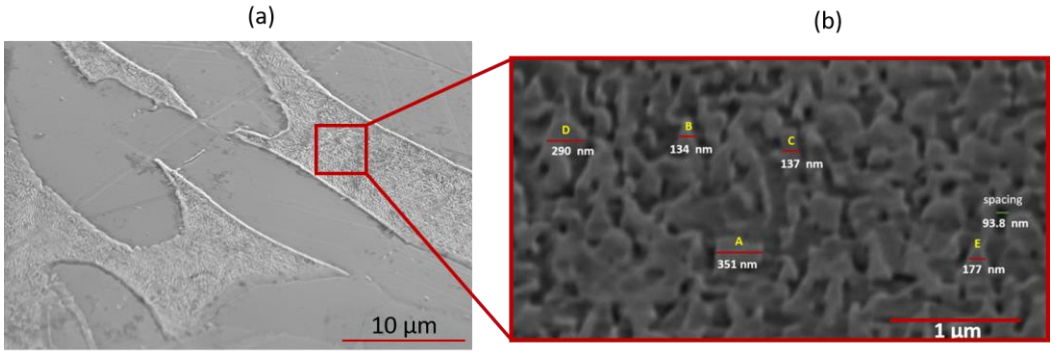

Figure 3.2 (a) shows the SEM image of the Al0.7CoCrFeNi HEA using the secondary electron detector, (b) shows the nanoprecipitates of varying diameter present in the dendrite region.

3.3.2 Elemental analysis

The elemental composition of $Al_{0.7}CoCrFeNi$ was analyzed using the Energy Dispersive Spectrometer (EDS) with line scans in the two regions. Figure 3.3 (a) presents the line scan of the interdendrite region and reveals an average composition of 23.2 $\pm$ 2.1 atomic percent (at. %) Co, 25.7 $\pm$ 2.4 at. % Cr, 27.0 $\pm$ 2.7 at. % Fe. The average content of Al and Ni in this region was less than 15.0 at. % each. Hereafter, we refer to the interdendrite region as the ‘‘Co–Cr–Fe rich region.’’ Figure 3.3 (b) shows the line scan of the dendrite region whose average composition was determined to contain 30.3 $\pm$ 3.1 at. % Al, 25.6 $\pm$ 3.3 at. % Ni, and the remaining elements (Co, Cr and Fe) had less than 16.0 at. % each. Hereafter, we refer to the dendrite region as the ‘‘Al–Ni rich region’’. This classification of both regions based on the specific element rich regions is consistent with those in [9], [11], [21]–[23]. From the elemental analysis of $Al_{0.7}CoCrFeNi$, we observed there was no presence of a single element rich phase which have been observed in Cu-containing HEAs [22] [24]; a single element rich phase such as Cr and Mn have been

observed to be sites for mechanical failure in the deformation of bulk HEA [25]. The chemistries of these phases would be useful in relating to their mechanical properties as a representation of the individual phases of the HEA rather than as a single element property.

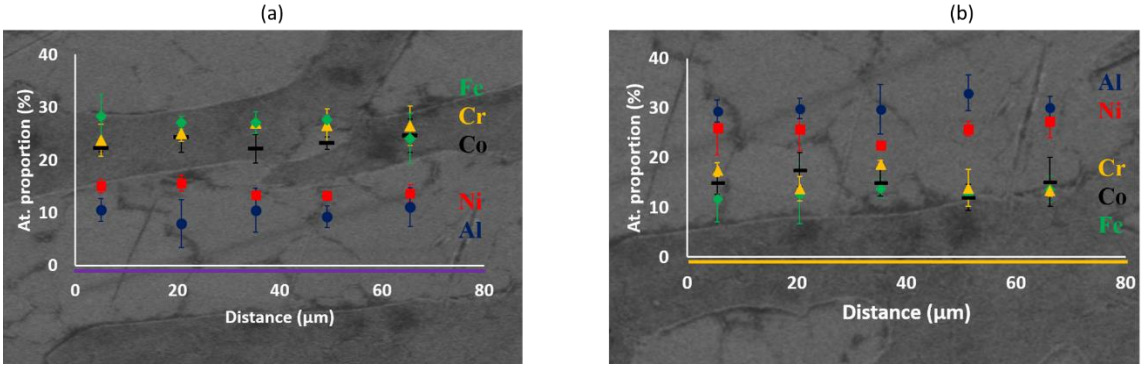

Figure 3.3 shows the elemental composition of (a) interdendrite (b) dendrite. The purple and yellow lines of (a) and (b) show the regions where the line scans were taken.

3.3.3 Phase Information and Orientation Microscopy

Orientation Image Mapping (OIM) was done to identify the phases from the lattice parameter values obtained from the XRD analysis using the Electron Back Scatter diffraction (EBSD) methodology. The Electron Back Scatter Diffraction maps shown in Figure 3.4 convey the phase contrast (Fig. 3.4 (b)) and the grain structure, as well as the crystallographic orientation of each grain (Fig. 3.4 (c)) of the Co–Cr–Fe rich region (interdendrite) and the Al–Ni rich region (dendrite). We used the lattice parameters of 0.3572 nm for the FCC phase and 0.2868 nm for the BCC (A2+B2) phase obtained via the X-ray diffraction spectrum of AlxCoCrFeNi (x = 0.1–2.0) from Reference [12]. OIM results reveal that the Co–Cr–Fe rich region (interdendrite) is the FCC phase and the Al–Ni rich region (dendrite) is the BCC (A2+B2) phase. We found the grain orientation to be

random in the two phases with an average grain size distribution of 2.85 μm in diameter on the orientation map shown in Figure 3.4 (b) and (c).

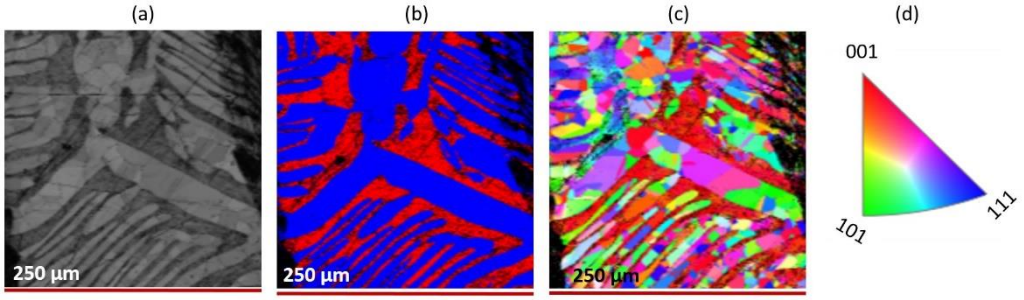

Figure 3.4 (a) Electron Image (b) Phase information; the blue is the FCC phase and the red is the BCC (A2+B2) phase (c) crystallographic orientation of the phases present (d) Pole figure labeling the orientations.

Transmission Electron Microscopy (TEM) analysis was done to identify additional microstructure within a phase such as the additional ordered phase, dislocation lines, slip planes, etc. Figure 3.5 shows the TEM analysis of the HEA, which further demonstrates two distinct phases present in this alloy. Figure 3.5 (a) presents the bright field image of the interdendrite region with the diffraction pattern in the inset, indicative of the FCC phase. Figure 3.5 (b) provides the TEM image of the dendrite region and the inset gives the diffraction pattern which indicates the presence of two phases from the ‘‘satellite-like’’ diffraction spots next to the main diffraction spots. The diffuse spots suggest the presence of the super-lattice diffraction which likely corresponds to the ordered B2 phase. Tung et al [10] suggested that it was the spinodal decomposition in the Al–Ni rich region that occurred during cooling of the HEA that led to the transformation from A2 to A2+B2.

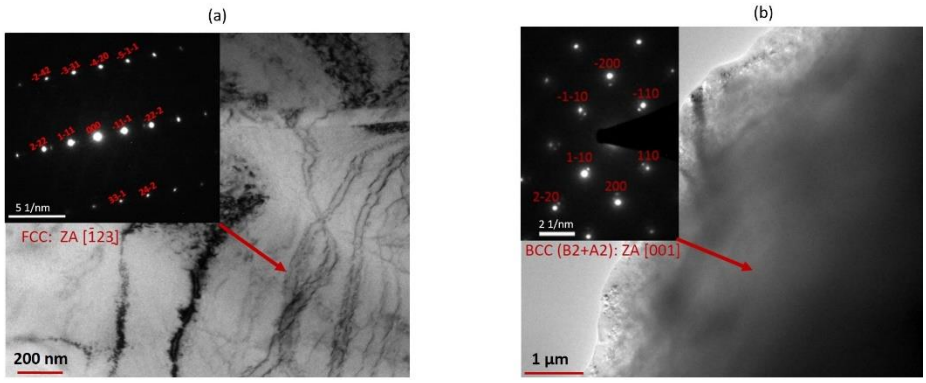

Figure 3.5 (a) Bright Field (BF) image of the interdendrite region with the diffraction pattern: ZA [123] at the top left (b) TEM image of the dendrite region with the diffraction pattern BCC (A2+B2) ZA:[001] at the top left where ZA is the zone axis.

3.4 Mechanical Properties of the individual phases of $Al_{0.7}CoCrFeNi$

Bulk HEAs have shown improved mechanical properties such as high strength, high temperature ductility, etc. [26]–[29]. Fewer studies have been done to understand the deformation mechanism of HEAs at the nanoscale, particularly in comparing them with pure metals with a focus on yield strength, size effect, and strain hardening.

3.4.1 Methodology

Using the Focused Ion Beam (FIB), we fabricated single-crystalline cylindrical nanopillars from each phase within individual grains in the $Al_{0.7}CoCrFeNi$ HEA. These nanopillars had diameters ranging from 400 nm to 2 μm and were oriented in the [324] direction for the FCC phase and in the [001] direction for the BCC phase. This fabrication methodology is described in Section 2.2. The final pillar dimensions were measured based on SEM images corrected for the tilt angle. The compression tests were carried out using a nanoindenter (Triboscope, Hysitron Inc) equipped with an 8 μm diamond flat punch. Experiments were conducted in a displacement rate-controlled mode at a constant

prescribed strain rate of 10^{-3} S^{-1} to a final total strain of 15% of the pillar height. Constant nominal strain rate was maintained by the feedback-loop algorithm in the nanoindenter software.

3.4.2 Uniaxial compression experiments

Figure 3.6 (a) and (b) show the SEM images of the representative pre - and post - compressed samples of the [324] oriented nanopillars fabricated from the FCC phase of the HEA. Crystallographic slip lines appear to be evenly distributed along multiple parallel slip planes, which is typical of the FCC crystals in low symmetry operations [30]. Figure 3.6 (c) shows the representative stress vs. strain data the FCC phase samples, showing the elastic loading region, the steep post-yield strain hardening to a strain of ∼2%, and the steady-state flow after. The smaller pillars exhibit higher yield strength and flow stresses typical of pure FCC metals. The slip angle after compression is measured to be 32.4° with respect to the loading axis. We observed multiple displacement bursts in pillars with diameters of 400 nm and smaller likely due to the inability of the instrument to catch the very fast burst events [31], [32]. Figure 3.7 (a) shows the SEM image of a representative compression of a [001]-oriented nanopillar carved from the BCC phase of the HEA. This image reveals wavy slip lines typical of BCC crystals. Figure 3.7 (b) shows the stress vs. strain data for the BCC phase pillars with diameters ranging from 400 nm to 2 μm and illustrates that the smaller pillars have higher yield strength and flow stresses similar to the pure BCC pillars under compression [33]. We also observed multiple displacement bursts in pillars with diameters of 400 nm and smaller likely due to the inability of the instrument to catch the very fast burst events [31], [32].

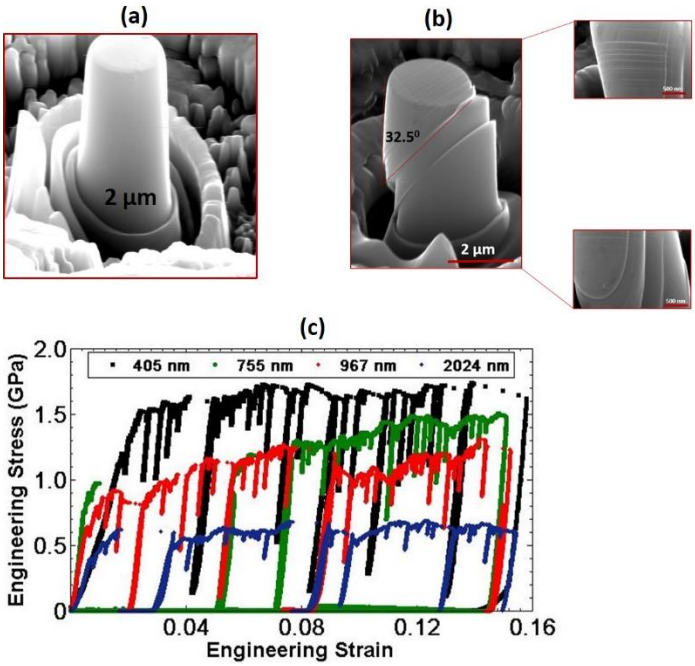

Figure 3.6 Representative (a) Pre-compressed image (b) Post-compressed image (c) Stress vs strain data of the [324] - oriented nanopillars in the FCC phase.

We observed a significant amount of strain hardening in this phase, which also appears to increase with reduced pillar size.

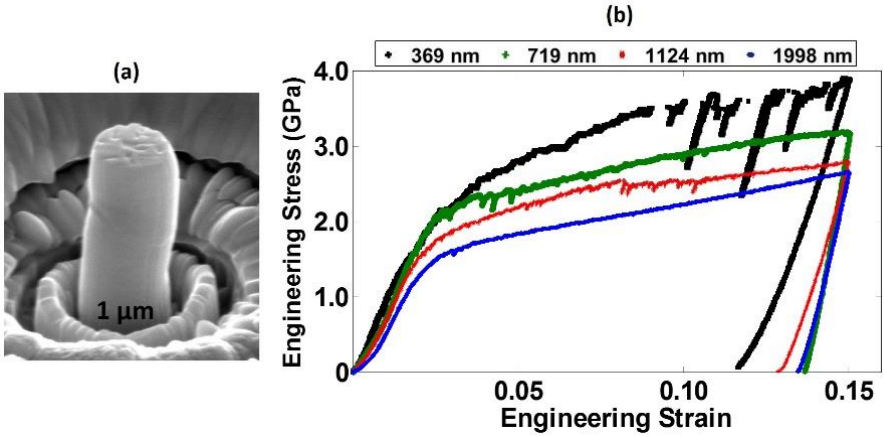

Figure 3.7 Representative (a) Pre-compressed image (b) Post-compressed image (c) Stress vs strain data of the [001] - oriented nanopillars in the BCC phase.

3.5 Discussion

3.5.1 Strength

Compressive strengths in the samples fabricated from both phases present in the HEA exhibited the ‘‘smaller is stronger’’ size effect, with the smallest, 400 nm-diameter nanopillar, having the highest strength of ~2.2 GPa in the BCC phase and ~1.2 GPa in the FCC phase. In bulk form, HEAs have been reported to have strengths higher than those of the conventional metals and alloys because of the heterogeneities in the atomic sizes leading to significant lattice distortion and higher intrinsic lattice resistance [7]. In the HEA studied here, Al has a larger atomic size of 1.43 Å compared with the other components: Co: 1.25 Å, Cr: 1.25 Å, Fe: 1.24 Å, and Ni: 1.24 Å. The presence of Al in the lattice likely increases the lattice distortion energy and leads to significant solid solution strengthening of the alloy [34]. A simple solid solution strengthening model [35] allows for the calculation of τ_{max}, the resolved shear stress required to tear the dislocation from the solute atom, Al in this case, as $\tau_{max} = F_{max}/bL'$, where b is the magnitude of the Burgers vector, and L' is the mean free path between the solute atoms. The mean spacing between the solute atoms in a crystallographic slip plane can be approximated as $b/\sqrt{2(c)}$, where c represents the concentration of the solute atoms. Using the EDX data obtained experimentally to calculate the relative atomic fraction of Al for a typical 400 nm-sized pillar, we find that the τ_{max}, or the shear stress required to push a dislocation through an array of solute atoms, is 0.68 MPa. This value is approximately one order of magnitude less than the resolved shear stress of 0.9 GPa, obtained from the data for the compression of a 400 nm-diameter nanopillar calculated from the axial applied stress. These results imply that solid-solution strengthening cannot be the sole or dominant cause of the observed high strength, although

it likely elevates the background stress of the BCC phase of the HEA. (See Appendix A for the detailed calculation).

In pure metals, size effects have been usually attributed to the distribution and motion of dislocations. For the same dislocation density in bulk, smaller-sized samples have fewer dislocations. The ‘‘smaller is stronger’’ size effect observed in the nanopillars fabricated from pure FCC metals and some alloys is thought to arise from of the annihilation of some of the pre-existing mobile dislocations at the available free surfaces, and the subsequent operation of harder and stronger dislocation sources to maintain the dislocation density necessary to accommodate the applied force and the ensuing plastic strain [36], [37]. In pure FCC nanopillars, dislocations present at the onset of plastic deformation leave the specimen before they multiply, forming the state of ‘‘dislocation starvation,’’ which requires the nucleation of new dislocations to accommodate plastic deformation [38], [39]. FCC metals undergo this type of deformation due to the glide dislocation motion during deformation. It is likely that the nano-pillars fabricated from the FCC phase of the HEA studied here (interdendrite, the Co–Cr–Fe rich region) experience the same plasticity mechanism. The distinct displacement bursts in the stress–strain data and multiple slip lines present in all deformed pillars suggest that this mechanism is retained even in these more complex alloys. BCC nanopillars also exhibit the ‘‘smaller is stronger’’ size effect, which has been shown to arise from more complex nanoplasticity mechanisms in pure BCC metals. In this type of crystal structure, individual dislocations can form kinks, with each component interacting with one another, forming junctions, all of which lead to greater dislocation densities, sessile junctions, and forest-like hardening upon the application of force [39], [40]. Similar arguments can be made for the size effect

that arises in the BCC phase of the $Al_{0.7}CoCrFeNi$ HEA. Wavy slip lines are present after compression presumably due to the cross slip of screw dislocations in the ⟨111⟩ direction, similar to W nanopillars [33]. The influence of different types of dislocation motion in each phase makes the BCC phase have higher strengths than those of the FCC phase [41]. The strength of the bulk sample (σ_{bulk}) was estimated to be *H/3*, where *H* represents nanoindentation hardness. Following this methodology, we found the strength of the bulk BCC phase as ~1.40 GPa and that of the FCC phase to be ~1.01 GPa. The yield stress of the 400 nm samples in the FCC phase of the HEA is 1.2 GPa, a factor of 1.5 greater than that of pure Ni nanopillars of equivalent dimensions, 0.8 GPa [30], Ni being the strongest of the commonly studied pure FCC metals (Cu, Al, and Au). The yield stress of the 400 nm diameter nanopillars fabricated from the BCC phase of the HEA studied here is 2.2 GPa, which is nearly equivalent to 2.0 GPa [33], the strength of 243 nm-diameter W, which is the strongest of the commonly studied pure BCC metals (Mo, Ta, Nb, and V).

3.5.2. Size effect

In most single crystalline metals at the micron and submicron scale, size dependence in strength can be described using the power law relation $\sigma = A / (D)^m$, where A is a constant and D is the pillar diameter. The exponent m is the main figure of merit for how much size-induced strengthening a particular family of materials exhibits. For example, Kim et al studied the size dependence of several pure BCC metals and found the power law exponent of the compressed W nanopillars to be − 0.43 [33]. To compare the size effect across different materials classes, it is useful to resolve the axial stress, which is what is typically measured in an experiment for samples in different orientations to the shear stress that operates on a relevant slip system [42]. When normalized by the shear

modulus (G) and the Burgers vector (b), the size dependence relation between the resolved shear stress τ and the pillar size D becomes $\tau/G = A(D/b)^m$.

3.5.2.1. FCC phase

We used the {111}/⟨110⟩ family of slip systems to calculate the resolved shear stress (τ) for the nanopillars fabricated from the FCC phase (Co–Cr–Fe rich region). These samples were oriented in the [324] direction, which has the Schmid factor of 0.634. We used the shear modulus of 75 GPa [43] reported for FeCr alloys to normalize the shear stress. Figure 3.8 (a) shows the plot of axial yield stress and the flow stress at a 10 % strain on the stress–strain data shown in Figure 3.6 (c) as a function of pillar diameter D. We found the slope m to be − 0.70 for the yield strength and − 0.63 for the 10 % flow stress. Figure 3.8 (b) shows the dependence of the resolved shear stress normalized by the shear modulus G as a function of pillar diameter normalized by the Burgers vector b on a log–log plot. A straight line that represents size effects in pure FCC metals is also provided for comparison (data obtained from [36]) and reveals a similar size dependence, with the ubiquitously reported m of − 0.66 for the yield strength and − 0.59 for the 10% flow stress. The plasticity mechanism in nano-sized FCC metals has been explained in the framework of dislocation starvation and dislocation source nucleation theory [36], [37]. A unified power law exponent m of − 0.6 has been observed in nearly all studied FCC metals (Ni, Cu, Al, Au) [36] with non-zero initial dislocation densities. Size-dependent strengthening in the FCC phase of our HEA can likely be explained by similar arguments because of the observed similarities in the morphology of the deformed samples, the stress versus strain data, and the power law strengthening exponent of − 0.6. The similarity in strengthening slope can be explained by the lower lattice distortion present in the FCC phase of the

$Al_{0.7}$CoCrFeNi compared with the BCC phase because the elements within the FCC phase; Co, Cr, Fe are similar in atomic size. The significantly higher strengths in the HEA likely stem from solution strengthening and high background stress [6], [7], [14], [44], and the multiple bursts observed in the stress–strain signature in Figure 3.6 (b) is an indication that there is ease of dislocation movement typical of the FCC metal.

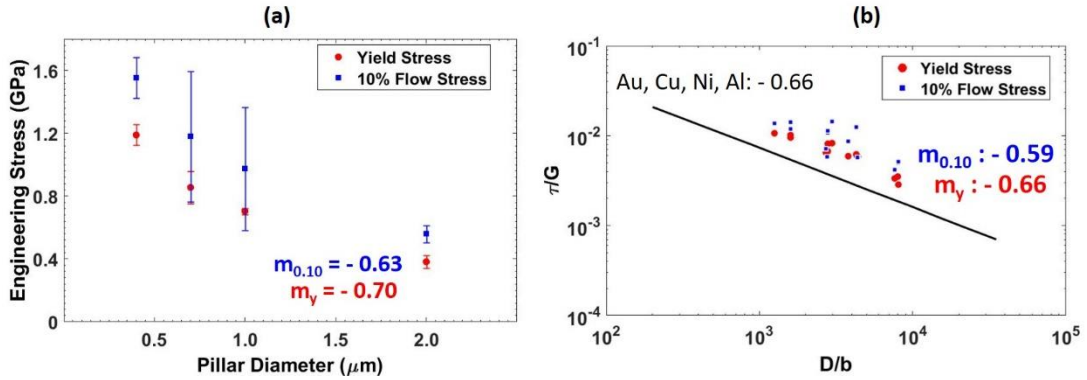

Figure 3.8 (a) Un-normalized size dependence plot of the FCC phase of the $Al_{0.7}$CoCrFeNi HEA where m_y *is the exponent calculated from the yield strength and* $m_{0.10}$ *is calculated from 10 % flow stress. Normalized sixe dependence plot of the FCC phase of the $Al_{0.7}$CoCrFeNI HEA compared with studied pure FCC metals. Source Au, Cu, Ni and AL: Data adapted from [36].*

3.5.2.2. BCC phase

We used the {110}/⟨111⟩ family of slip systems to calculate the resolved shear stress (τ) for the nanopillars fabricated from the BCC phase (Al–Ni rich region). These nanopillars were oriented in [001] with a Schmid factor of 0.408. We used the shear modulus G of 70 GPa [45] which is consistent with 65 $\pm$ 4 GPa that Frommeyer et al reported in the study on Ni–Al alloys [46]. Figure 3.9 (a) shows the axial as-measured yield stress, 2.25 GPa for the 400 nm sized pillar, as well as the flow stress at a 10 % strain, 3.5 GPa for equivalent size pillar as a function of nanopillar diameter, obtained from the stress versus strain data shown in Figure 3.7 (b). Fitting a power law functional form to each of

these data sets reveals the slope m of − 0.28 for the yield strength and − 0.27 for the flow stress. Figure 3.9 (b) gives the normalized size dependence for the BCC phase of the HEA and compares it with the normalized size dependence of reported pure BCC metals (V, Nb, Mo, Ta, and W). The BCC phase of the HEA appears to exhibit higher strengths and a reduced size dependence (m = − 0.28) compared to the pure counterparts. This value is slightly less than the lowest exponent of all pure BCC metals of − 0.32, reported for W by Kim et al. [33], [36], although power law exponents as low as − 0.21 have also been reported for W [47], − 0.22 for [001] Mo and − 0.34 for [235] Mo [48]. Zou et al studied a BCC refractory HEA (Nb25Mo25Ta25W25) and found that the strengthening size effect slope was m = − 0.33.

The difference in size dependence amongst the BCC metals has been attributed to the difference in their residual Peierls barrier at room temperature, with the highest Peierls barrier having the least pronounced size dependence [36]. In addition to the Peierls barrier, HEAs have the lattice distortion effect [6], [7], [14], [44], [49] which is even more prominent in the BCC phase of the Al0.7CoCrFeNi HEA. Wang and Zou reported that higher lattice distortion leads to greater lattice resistance, which amplifies the effective Peierls barrier in the system [31], [41], [50]. Using the temperature-dependent relation of the sum of lattice friction [51] as a contribution to the resolved shear stress, $\tau^* = (1 - T_t/T_c)\tau_0^*$, where τ^* is the stress required to overcome the Peierls barrier, T_t is the test temperature, T_c is the critical temperature and τ_0^* is the Peierls stress at 0 K. Zou et al. reported that materials with higher T_t/T_c are expected to have a reduced size effect, i.e. a lower slope m [31]. More experimental and theoretical work needs to be done to study the effect of the critical temperature and of the Peierls barrier of HEAs.

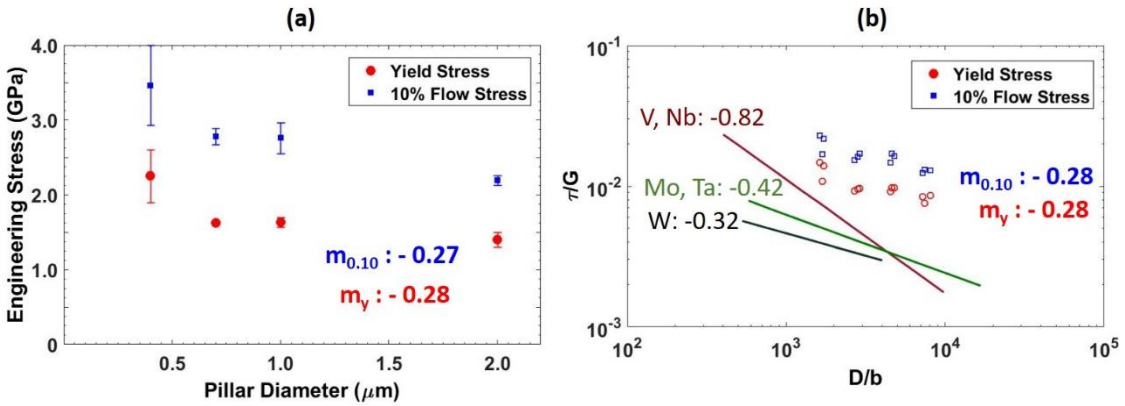

Figure 3.9 (a) Un-normalized size dependence plot of the BCC phase of the Al0.7CoCrFeNi HEA where m_y is the exponent calculated from the yield strength and $m_{0.10}$ is calculated from 10 % flow stress. Normalized size dependence plot of the BCC phase of the Al0.7CoCrFeNI HEA compared with studied pure BCC metals. Source V, Nb, Mo, Ta, W: Data adapted from [36].

3.5.2.3. Strain hardening

The stress versus strain data of the FCC phase shown in Figure 3.6 (a) indicates the presence of multiple, densely populated discrete strain bursts. We applied the hardening angle method used by Kunz et al [52] and the Holloman relationship in an attempt to quantitatively describe the strain hardening behavior in the FCC phase. Hardening angles were measured from the region of the stress–strain data where contact had been established in the steady state flow region to the onset of unloading, using 0.04 and 0.15 strains to define the end points. We observed that the measured angles fall within the range of 2–11°. This trend suggests that some marginal strain hardening is present in this region and does not appear to be size dependent, as shown in Figure 3.10 (a).

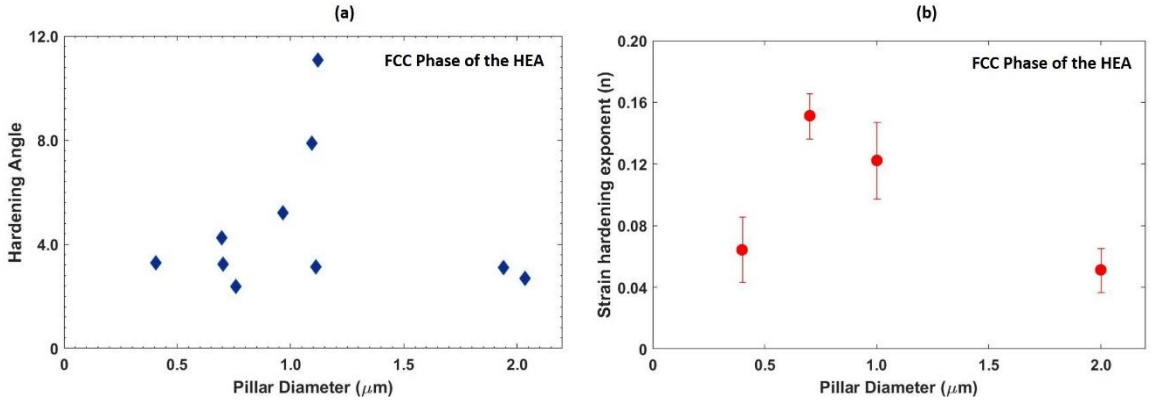

Figure 3.10 (a) Hardening angles vs. pillar diameter (μm) (b) Strain hardening exponent plot of the FCC phase of the $Al_{0.7}$CoCrFeNi HEA.

The Holloman formula, $\sigma = K\epsilon^n$ defines the relationship between the engineering stress and engineering strain, with K being the strength coefficient, and the measured parameter, n, being the strain-hardening exponent. 4% and 15% strains were used as end points in this calculation. We calculated n to vary between 0.06 and 0.15, as shown in Figure 3.10 (b). This shows that no apparent size effect or exponent trend in strain hardening were present in the FCC phase of the HEA.

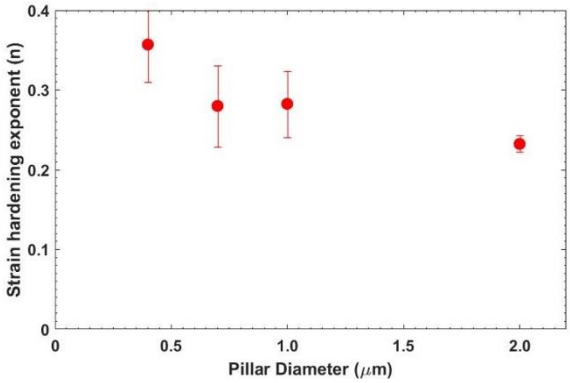

Figure 3.11. Strain hardening exponent plot of the BCC phase of the $Al_{0.7}$CoCrFeNi HEA.

The discrete strain bursts observed in the stress vs. strain data shown in Figure 3.6(c) suggest irregular hardening angles (see Figure 3.10). We also calculated the strain hardening exponent, n, for the nanopillars in the BCC phase, and found n to be in the range

between values of 0.22 – 0.35 (see Figure 3.11) with the smallest pillar size of 400 nm having the highest *n*. This observed size effect on the strain hardening exponent may be explained in terms of the initial dislocation densities present in the nanopillars, with more cross slip events of the screw dislocations in the smaller pillars.

3.6 Summary and Outlook

We studied the microstructure and mechanical properties of the $Al_{0.7}CoCrFeNi$ high-entropy alloy, which revealed the presence of two distinct crystallographic phases: (1) FCC phase which is the Co–Cr–Fe rich region or ‘‘the interdendrite’’and (2) BCC (A2+B2) phase which is the Al–Ni rich region a.k.a. ‘‘the dendrite.’’ We fabricated nanopillars ranging from 400 nm to 2 μm in diameter and uniaxially compressed them to study their mechanical response. We observed very high strengths in both phases; ∼2.2 GPa for the 400 nm nanopillars in the BCC phase and ∼1.2 GPa for equivalent size nanopillars in the FCC phase. We found that the yield strength of the smallest, 400 nm-diameter nanopillars extracted from the BCC phase is 1.5 times higher than that of the bulk, and 1.2 times higher for the FCC phase. We found that the size dependence of strength on pillar diameter in the FCC phase of the HEA is similar to that of pure FCC metals, with a strengthening exponent of − 0.66. We discovered that the BCC phase also exhibits a ‘‘smaller is stronger’’ size effect with the exponent of − 0.28 between strength and pillar diameter, which is lower than all size dependence reported for pure BCC metals, with only W approaching it at − 0.32. The absolute strength of the nano-pillars fabricated from the FCC phase is a factor of 1.5 higher than those of nickel (which is the strongest of the commonly studied FCC metals). We also observed pronounced strain hardening during the plastic deformation of the BCC phase, which in itself is size dependent, with smaller

nanopillars having greater strengthening with strain. The strain hardening observed in the FCC phase is marginal and not size dependent, likely due to a lack of dislocation interactions and multiplication. We postulate that the difference in the size dependence between the two phases is a result of the difference in the lattice resistance coming from higher presumed distortion energy in the BCC phase compared to the FCC phase.

References

[1] "Vacuum Arc Melting Unit," *http://home.iitk.ac.in/~anandh/lab/Arc_Melting.pdf*. [Online]. Available: http://home.iitk.ac.in/~anandh/lab/Arc_Melting.pdf. [Accessed: 24-May-2018].

[3] J. Young, "The Crystal Structure of Meteoric Iron as Determined by X-Ray Analysis," *Proc. R. Soc. A Math. Phys. Eng. Sci.*, vol. 112, no. 762, pp. 630–641, Oct. 1926.

[4] C. N. T. Belaiew, "On the Genesis of Widmanstätten Structure in Meteorites and in Iron-Nickel and Iron-Carbon Alloys," *Mineral. Mag.*, vol. 20, no. 104, pp. 173–185, 1924.

[5] R. P. Todorov and K. G. Khristov, "Widmanstatten Structure of Carbon Steels," *Met. Sci. Heat Treat.*, vol. 46, no. 1/2, pp. 49–53, Jan. 2004.

[6] J. W. Yeh, S. K. Chen, S. J. Lin, J. Y. Gan, T. S. Chin, T. T. Shun, C. H. Tsau, and S. Y. Chang, "Nanostructured high-entropy alloys with multiple principal elements: Novel alloy design concepts and outcomes," *Adv. Eng. Mater.*, vol. 6, no. 5, p. 299–303+274, 2004.

[7] Y. Zhang, T. T. Zuo, Z. Tang, M. C. Gao, K. A. Dahmen, P. K. Liaw, and Z. P. Lu, "Microstructures and properties of high-entropy alloys," *Prog. Mater. Sci.*, vol. 61, no. October 2013, pp. 1–93, Apr. 2014.

[8] C.-Y. Hsu, J.-W. Yeh, S.-K. Chen, and T.-T. Shun, "Wear Resistance and High-Temperature Compression Strength of Fcc CuCoNiCrAl 0.5 Fe Alloy with Boron Addition."

[9] S. Singh, N. Wanderka, B. S. Murty, U. Glatzel, and J. Banhart, "Decomposition in multi-component AlCoCrCuFeNi high-entropy alloy," *Acta Mater.*, vol. 59, no. 1, pp. 182–190, 2011.

[10] C. C. Tung, J. W. Yeh, T. T. Shun, S. K. Chen, Y. S. Huang, and H. C. Chen, "On the elemental effect of AlCoCrCuFeNi high-entropy alloy system," *Mater. Lett.*, vol. 61, no. 1, pp. 1–5, 2007.

[11] W. R. Wang, W. L. Wang, and J. W. Yeh, "Phases, microstructure and mechanical properties of AlxCoCrFeNi high-entropy alloys at elevated temperatures," *J. Alloys Compd.*, vol. 589, pp. 143–152, 2014.

[12] W.-R. Wang, W.-L. Wang, S.-C. Wang, Y.-C. Tsai, C.-H. Lai, and J.-W. Yeh, "Effects of Al addition on the microstructure and mechanical property of AlxCoCrFeNi high-entropy alloys," *Intermetallics*, vol. 26, pp. 44–51, 2012.

[13] T.-T. Shun and Y.-C. Du, "Microstructure and tensile behaviors of FCC Al 0.3 CoCrFeNi high entropy alloy," *J. Alloys Compd.*, vol. 479, pp. 157–160, 2009.

[14] Z. Tang, M. C. Gao, H. Diao, T. Yang, J. Liu, T. Zuo, Y. Zhang, Z. Lu, Y. Cheng, Y. Zhang, K. a. Dahmen, P. K. Liaw, and T. Egami, "Aluminum alloying effects on lattice types, microstructures, and mechanical behavior of high-entropy alloys systems," *Jom*, vol. 65, no. 12, pp. 1848–1858, 2013.

[15] K.-C. Hsieh, C.-F. Yu, W.-T. Hsieh, W.-R. Chiang, J. Son Ku, J.-H. Lai, C.-P. Tu, and C. Chao Yang, "The microstructure and phase equilibrium of new high performance high-entropy alloys," *J. Alloys Compd.*, vol. 483, pp. 209–212, 2009.

[16] K. Zhang and Z. Fu, "Effects of annealing treatment on phase composition and microstructure of CoCrFeNiTiAl x high-entropy alloys," *Intermetallics*, vol. 22, pp. 24–32, 2012.

[17] U. S. Hsu, U. D. Hung, J. W. Yeh, S. K. Chen, Y. S. Huang, and C. C. Yang, "Alloying behavior of iron, gold and silver in AlCoCrCuNi-based equimolar high-entropy alloys," *Mater. Sci. Eng. A*, pp. 460–461, 2007.

[18] C.-J. Tong, Y.-L. Chen, S.-K. Chen, J.-W. Yeh, T.-T. Shun, C.-H. Tsau, S.-J. Lin, and S.-Y. Chang, "Microstructure Characterization of Al x CoCrCuFeNi High-Entropy Alloy System with

Multiprincipal Elements."
[19] O. N. Senkov, S. V. Senkova, and C. Woodward, "Effect of aluminum on the microstructure and properties of two refractory high-entropy alloys," *Acta Mater.*, vol. 68, pp. 214–228, 2014.
[20] O. N. Senkov, C. Woodward, and D. B. Miracle, "Microstructure and Properties of Aluminum-Containing Refractory High-Entropy Alloys," *Jom*, vol. 66, no. 10, pp. 2030–2042, 2014.
[21] M.-H. Tsai and J.-W. Yeh, "High-Entropy Alloys: A Critical Review," *Mater. Res. Lett.*, vol. 2, no. 3, pp. 107–123, 2014.
[22] A. Manzoni, H. Daoud, R. Völkl, U. Glatzel, and N. Wanderka, "Phase separation in equiatomic AlCoCrFeNi high-entropy alloy.," *Ultramicroscopy*, vol. 132, pp. 212–5, Sep. 2013.
[23] Z. Tang, L. Huang, W. He, and P. K. Liaw, "Alloying and processing effects on the aqueous corrosion behavior of high-entropy alloys," *Entropy*, vol. 16, no. 2, pp. 895–911, Feb. 2014.
[24] K. G. Pradeep, N. Wanderka, P. Choi, J. Banhart, B. S. Murty, and D. Raabe, "Atomic-scale compositional characterization of a nanocrystalline AlCrCuFeNiZn high-entropy alloy using atom probe tomography," *Acta Mater.*, vol. 61, no. 12, pp. 4696–4706, 2013.
[25] B. Gludovatz, A. Hohenwarter, D. Catoor, E. H. Chang, E. P. George, and R. O. Ritchie, "A fracture-resistant high-entropy alloy for cryogenic applications," *Science (80-.).*, vol. 345, no. 6201, pp. 1153–1158, 2014.
[26] C. Hsu, J. Yeh, S. Chen, and T. Shun, "Wear resistance and high-temperature compression strength of Fcc CuCoNiCrAl0.5Fe alloy with boron addition," *Metall. Mater. Trans. A*, vol. 35, no. 5, pp. 1465–1469, 2004.
[27] T. T. Shun and Y. C. Du, "Microstructure and tensile behaviors of FCC Al0.3CoCrFeNi high entropy alloy," *J. Alloys Compd.*, vol. 479, no. 1–2, pp. 157–160, 2009.
[28] A. V. Kuznetsov, D. G. Shaysultanov, N. D. Stepanov, G. A. Salishchev, and O. N. Senkov, "Tensile properties of an AlCrCuNiFeCo high-entropy alloy in as-cast and wrought conditions," *Mater. Sci. Eng. A*, vol. 533, pp. 107–118, 2012.
[29] C. W. Tsai, M. H. Tsai, J. W. Yeh, and C. C. Yang, "Effect of temperature on mechanical properties of Al0.5CoCrCuFeNi wrought alloy," *J. Alloys Compd.*, vol. 490, no. 1–2, pp. 160–165, 2010.
[30] C. P. Frick, B. G. Clark, S. Orso, a. S. Schneider, and E. Arzt, "Size effect on strength and strain hardening of small-scale [1 1 1] nickel compression pillars," *Mater. Sci. Eng. A*, vol. 489, no. 1–2, pp. 319–329, 2008.
[31] Y. Zou, S. Maiti, W. Steurer, and R. Spolenak, "Size-dependent plasticity in an Nb25Mo25Ta25W25 refractory high-entropy alloy," *Acta Mater.*, vol. 65, pp. 85–97, Feb. 2014.
[32] D. M. Dimiduk, E. M. Nadgorny, C. Woodward, M. D. Uchic, and P. a. Shade, "An experimental investigation of intermittent flow and strain burst scaling behavior in LiF crystals during microcompression testing," *Philos. Mag.*, vol. 90, no. 27–28, pp. 3621–3649, 2010.
[33] J. Y. Kim, D. Jang, and J. R. Greer, "Tensile and compressive behavior of tungsten, molybdenum, tantalum and niobium at the nanoscale," *Acta Mater.*, vol. 58, no. 7, pp. 2355–2363, 2010.
[34] F. J. Wang, Y. Zhang, G. L. Chen, and H. A. Davies, "Cooling Rate and Size Effect on the Microstructure and Mechanical Properties of AlCoCrFeNi High Entropy Alloy," *J. Eng. Mater. Technol.*, vol. 131, no. 3, p. 034501, Jul. 2009.
[35] T. H. Courtney, *Mechanical behavior of materials*. Waveland Press, 2005.
[36] J. R. Greer and J. T. M. De Hosson, "Plasticity in small-sized metallic systems: Intrinsic versus extrinsic size effect," *Prog. Mater. Sci.*, vol. 56, no. 6, pp. 654–724, 2011.
[37] H. Sanavia and B. Schrefler, *Mechanics of Advanced Materials and Structures*. 2007.
[38] J. R. Greer, W. C. Oliver, and W. D. Nix, "Size dependence of mechanical properties of gold at the micron scale in the absence of strain gradients," *Acta Mater.*, vol. 53, no. 6, pp. 1821–1830, 2005.
[39] J. R. Greer, C. R. Weinberger, and W. Cai, "Comparing the strength of f.c.c. and b.c.c. sub-micrometer pillars: Compression experiments and dislocation dynamics simulations," *Mater. Sci. Eng. A*, vol. 493, no. 1–2, pp. 21–25, 2008.
[40] S. Brinckmann, J. Y. Kim, and J. R. Greer, "Fundamental differences in mechanical behavior between two types of crystals at the nanoscale," *Phys. Rev. Lett.*, vol. 100, no. APRIL, pp. 1–4, 2008.
[41] S. Wang, "Atomic Structure Modeling of Multi-Principal-Element Alloys by the Principle of Maximum Entropy," *Entropy*, vol. 15, no. 12, pp. 5536–5548, Dec. 2013.
[42] W. Callister and D. Rethwisch, *Materials science and engineering: an introduction*, vol. 94. 2007.
[43] F. Louchet, "From individual dislocation motion to collective behaviour," *J. Mater. Sci.*, vol. 41, no. 9, pp. 2641–2646, 2006.

[44] T. Egami and Y. Waseda, “Atomic size effect on the formability of metallic glasses,” *J. Non. Cryst. Solids*, vol. 64, no. 1–2, pp. 113–134, 1984.
[45] D. B. Miracle and R. Darolia, “NiAl and its Alloys,” *Struct. Appl. Intermet. Compd.*, p. 20, 2000.
[46] G. Frommeyer, R. Rablbauer, and H. J. Schäfer, “Elastic properties of B2-ordered NiAl and NiAl-X (Cr, Mo, W) alloys,” *Intermetallics*, vol. 18, no. 3, pp. 299–305, 2010.
[47] A. S. Schneider, C. P. Frick, P. a. Gruber, R. Mönig, O. Kraft, E. Arzt, D. Kaufmann, B. G. Clark, C. P. Frick, P. a. Gruber, R. Mönig, O. Kraft, and E. Arzt, “Correlation between critical temperature and strength of small-scale bcc pillars,” *Phys. Rev. Lett.*, vol. 103, no. 10, pp. 1–4, 2009.
[48] A. S. Schneider, B. G. Clark, C. P. Frick, P. A. Gruber, and E. Arzt, “Effect of orientation and loading rate on compression behavior of small-scale Mo pillars,” *Mater. Sci. Eng. A*, vol. 508, no. 1–2, pp. 241–246, 2009.
[49] W. Guo, W. Dmowski, J.-Y. Noh, P. Rack, P. K. Liaw, and T. Egami, “Local Atomic structure of a high-entropy alloy: an X-ray and neutron scattering study,” *Metall. Mater. Trans. A*, vol. 44, no. 5, pp. 1994–1997, 2013.
[50] Y. Zou, H. Ma, and R. Spolenak, “Ultrastrong ductile and stable high-entropy alloys at small scales,” *Nat. Commun.*, vol. 6, 2015.
[51] D. Hull and D. J. Bacon, *Introduction to Dislocations*. 2001.
[52] A. Kunz, S. Pathak, and J. R. Greer, “Size effects in Al nanopillars: Single crystalline vs. bicrystalline,” *Acta Mater.*, vol. 59, no. 11, pp. 4416–4424, 2011.

Chapter 4 . Temperature effect on Small-scale deformation on the phases of $Al_{0.7}CoCrFeNi$ HEA

4.1 Introduction

Engineering materials are continuously designed for extreme environments, for example high/low temperatures, high pressure, toxic chemical environment, and small – scale applications. Most of the existing engineering materials are reinforced as composites, alloyed with other metals, include precipitates, etc. Several fabrication techniques and architectures have been explored to get improved sum-total materials properties.

High-Entropy Alloys have shown unusual properties at extreme conditions. At high pressures greater than 14 GPa, CrMnFeCoNi HEA was observed to undergo a phase transformation from FCC to the HCP due to atomic displacement as a result of stacking fault formation [1]. Refractory HEAs have also been studied at elevated temperatures, showing independent temperature strain hardening at 296 - 873 K due to the formation twin activity and shear band formation in this temperature range [2]. Low temperature studies on HEAs have also been conducted at the macro-scale showing excellent properties; Gludovatz et al studied CrMnFeCoNi to have tensile strengths of 1 GPa and fracture toughness of 200 MPa $m^{1/2}$ due to the twins formation during deformation at 77 K [3].

Small-scale mechanical studies are important to evaluate and understand the individual contributing factors such as dislocation density, grain size, surface effect to deformation of the same material system at the bulk scale nanoscale [4]. This is also essential for the design of NEMS/MEMS devices [5], [6], [7]. Furthermore, effect of

temperature and size on nanoplasticity is essential for newly developed nanotechnologies especially in fields of aerospace applications, satellite parts, and tanks for liquefied gases.

Low temperature experiments on small-sized HEAs are yet to be explored to determine the size-property-microstructure relationship so as to compare their mechanical properties with their bulk counterparts, pure metals, and conventional alloys. To compare the small-scale mechanical properties of commonly observed crystal structures of HEA, we chose the $Al_{0.7}$CoCrFeNi HEA due to its dual-phase nature, i.e. FCC and BCC phases. These phases in our initial work at room temperature show distinct mechanical properties at the small scale [8]. In this work, we introduce the effect of temperatures (40 K to 295 K) on strength, nanoplasticity, work hardening, size-effect dependence, slip events, etc. taking into account the solid solution nature of the HEA and the intrinsic dislocation structure of the individual phases.

Molecular dynamics simulations were done by Dr. Zach H. Aitken, Dr. Mehdi Jafary-Zadeh, and Dr. Yong Wei Zhang from the Institute of High Performance Computing Singapore. These were performed on a representative FCC and BCC HEA in order to better understand the atomic mechanisms. Deformation in both phases indicates dislocation or dislocation/twinning of mediated mechanisms. We relate this to the low stacking energies promoting the different types of deformation mechanisms and temperature – dependent strengthening in the two phases.

4.2 Experimental Procedure

$Al_{0.7}$CoCrFeNi HEA was fabricated using the vacuum arc melting method with powders (Al, Co, Cr Fe and Ni) of 99 % purity. Details of this process are described in Section 3.2. Phase and orientation information were identified using Electron Back Scatter

Diffraction (EBSD) as described in Section 3.4. The nanopillars were fabricated from the single crystals of [324] for the FCC phase and [001] for the BCC phase using the Focused Ion Beam milling procedure described in Section 2.2. Pillars were fabricated for sizes ranging from 400 nm to 2 μm.

For the mechanical experiments, an in-situ nanomechanical set-up developed by Lee, et al [9] was used. This combines the nanoindenter (INSEM^{TM}) from Nanomechanics Inc., the FEI Quanta Scanning Electron Microscope and the cryogenic assembly by Janis Research Company. This is fully described in Section 2.2.2. The uniaxial compression experiments were carried out using an 8 μm tungsten carbide flat punch tip coated with Au was used. Displacement-rate control mode was used at a strain rate of 10^{-3} s^{-1} up to 15 % strain. TEM samples were fabricated using the lift-out approach. The samples were then thinned using the Ga^{+} source until a sample thickness of 60 - 65 nm was achieved. For the final thinning step, a voltage of 8 KeV and current of 42 pA were used. We obtained and indexed diffraction patterns of the pillars and collected several bright field, dark field, and high-resolution images of the deformed microstructure.

4.3 Results

Figure 4.1 (a-c) shows the stress versus strain data for representative [324]-oriented FCC nanopillars with diameters ranging from 400 nm to 2 μm, deformed at 295 K (Fig. 4.1(a)), 143 K (Fig. 4.1(b)) and 40 K (Fig. 4.1(c)). These experiments revealed that the yield and flow stresses of samples with equivalent diameters were highest at 40 K and lowest at 295 K. For example, the ~700 nm-diameter pillars had a yield strength of ~ 0.7 GPa at 295 K, 1.2 GPa at 143 K, and 1.6 GPa at 40 K. The relative increase in the yield stress with temperature appears to be lower for smaller-diameter samples: the yield strength

of 2 μm-diameter pillars increased by a factor of ~ 2 when temperature was lowered from 295 K to 143 K and by a factor of ~ 1.2 from 143 K to 40 K. For the 400 nm diameter samples, this relative strengthening was ~ 1.45 and 1.25 for the same temperature variations. The mechanical response of the FCC pillars from the stress-strain data in Figure 4.1 (a-c) show stochastic burst events whose intermittency increases with reducing pillar sizes and reduces for the same pillar size as the temperature reduces from 295 K to 40 K.

Figure 4.1 (d-f) shows SEM images of the typical deformation morphology of these [324]-oriented FCC samples at each temperature, which contain multiple slip lines predominantly parallel to each other and oriented at ~ 38° to 48° with respect to the loading direction, consistent with <011> / {111} or <110> / {111} slip system. The primary slip direction is indicated by the yellow arrows in the post compressed pillars in Figures 4.1(d-f). At lower temperatures, secondary slip direction emerges, which is indicated by the red arrows in Figures 4.1(e & f) for deformed nanopillars at 143 K and 40 K respectively. These images and the compressive stress-strain response suggest that the deformation mechanism remained the same at all temperatures.

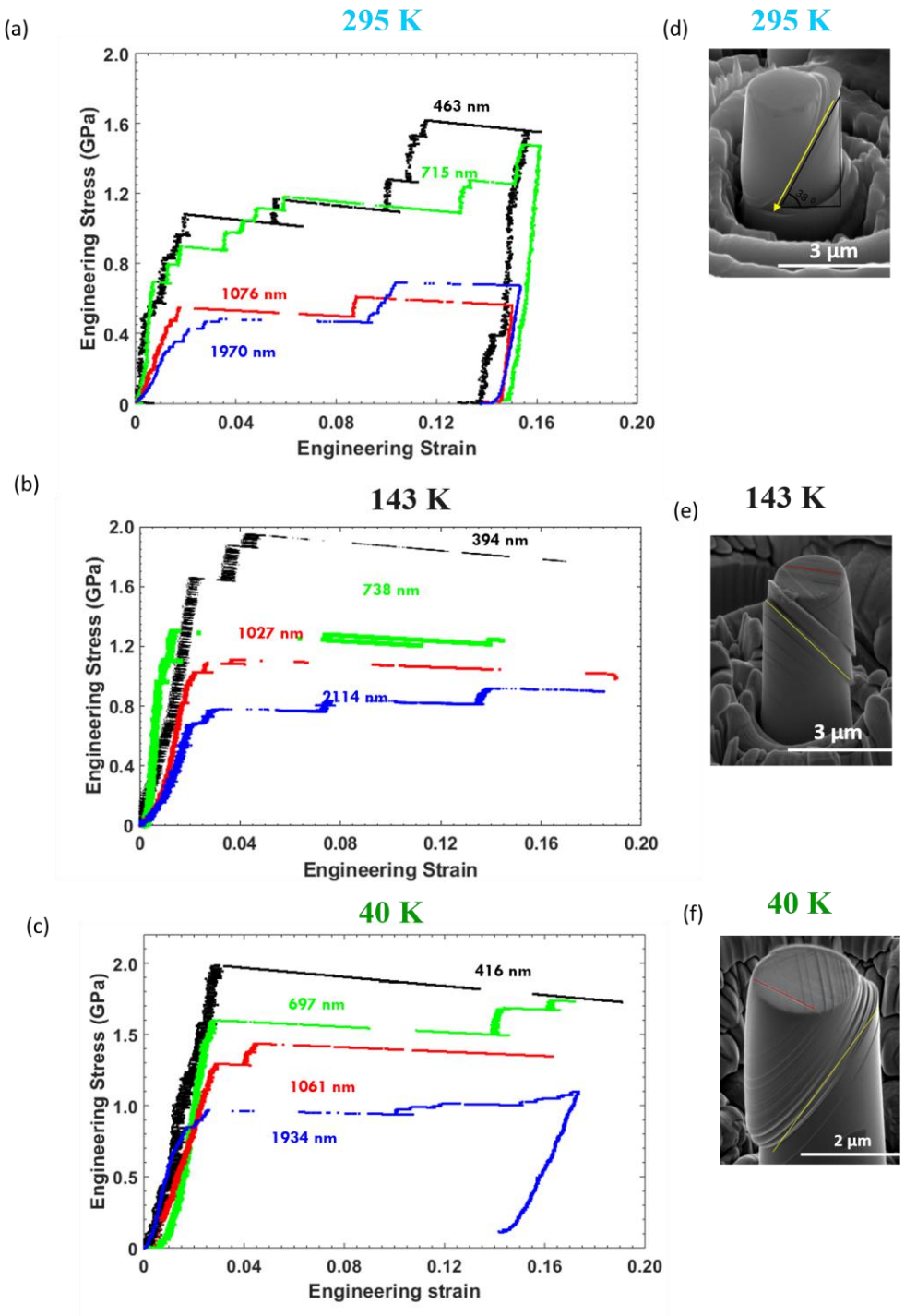

Figure 4.1 (a), (b) and (c) show the representative stress-strain curves of [324] FCC nanopillars compressed at 295 K, 143 K and 40 K respectively. Fig. 4.1(d), (e), and (f) give a typically deformed 2 µm-sized [324] FCC nanopillars at 295 K, 143 K and 40 K respectively.

Figure 4.2 (a-c) shows the compressive stress-strain response of nanopillars with diameters between ~ 400 nm and 1.8 um, fabricated from the [001]-oriented BCC phase deformed at the temperatures of 295 K (Fig. 4.2(a)), 143 K (Fig. 4.2(b)), and 40 K (Fig. 4.2(c)). We observed a marginal increase in the yield strength at different temperatures for the same pillar sizes: the yield strength of a 400 nm-diameter pillar increased by a factor of 1.2 from 2.5 GPa to 3.0 GPa as the temperature was lowered from 295 K to 143K, and then by a factor of 1.1 from 3.0 GPa to 3.2 GPa as it was further lowered to 40 K. The deformation signature of the BCC samples is different from the FCC pillars since the stress-strain data are smoother and less stochastic, especially for samples with larger diameters (~2 μm) pillars.

Figure 4.2 (d-f) contains SEM images that convey typical deformation morphology of the 2 μm-diameter [001]-oriented BCC pillars at each temperature. These images reveal that the deformation at all temperatures occurred via wavy crystallographic slip, whose traces are shown in Figure 4.2 (d) and a volumetric expansion at the pillar top.

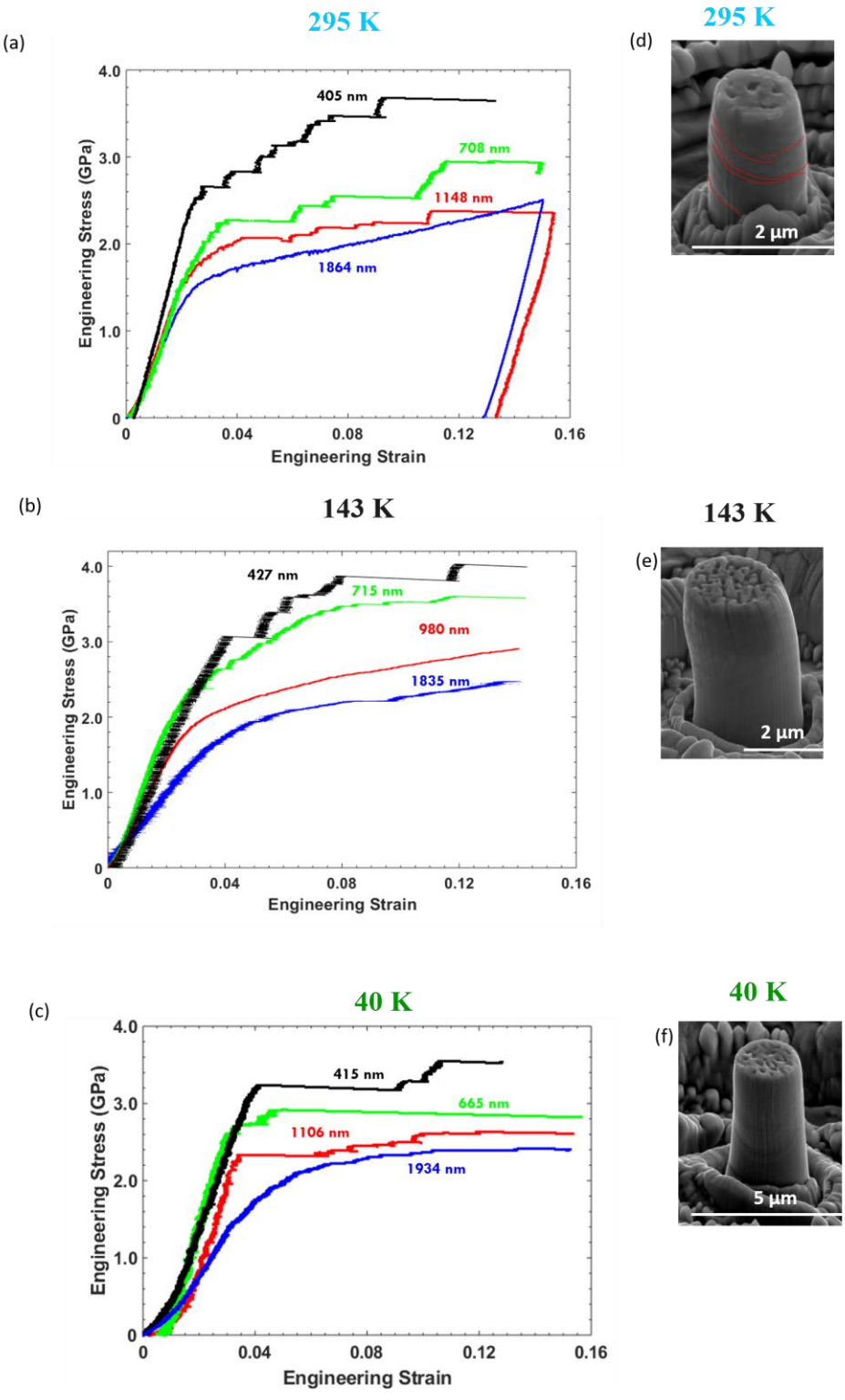

Figure 4.2 (a), (b) and (c) show the representative stress-strain curve of [001] BCC nanopillars compressed at 295 K, 143 K and 40 K respectively. Fig. 1(d), (e) and (f) give typically deformed [001] BCC nanopillars at 295 K, 143 K and 40 K respectively.

We calculated the work hardening exponent using Equation 4.1 for BCC nanopillars that show continuous plasticity in the stress versus strain data. The stresses for the calculation of the work hardening exponents (n) were taken at 6 and 12 % strain for all the test temperatures.

$$n = \frac{\partial \ln(\sigma_{12} - \sigma_6)}{\partial \ln(\varepsilon_{12} - \varepsilon_6)} \quad (4.1)$$

We observed that the work hardening exponent decreases as the temperature is decreased, indicated by the reduced flow stress, notably at 40 K shown in Figure 4.2 (c). The work hardening exponent calculated from the stress-strain curves of 2 μm size pillars reduces from n = 0.27 at 295 K to 0.19 at 143 K and 0.16 at 40 K.

Figure 4.3 (a) shows the plot of the yield stress, defined as stress of the first burst event after the elastic regime, of [324]-oriented FCC pillars versus pillar diameter deformed at each temperature. This yield strength was obtained from the stress-strain data for each pillar, examples of which are shown in Figure 4.1(a-c). Error bars in Figure 4.3 (a) represent the range of stresses for each pillar size. This plot clearly demonstrates that the strengths of pillars of all sizes consistently increased with the reduction in temperature, and that the highest strength in excess of 2 GPa was attained by samples with the smallest diameters of ~ 400 nm at 40 K. The ~ 2um-diameter pillars deformed at room temperature had the lowest strength of ~ 400 MPa. Figure 4.3(b) shows a log-log plot of these yield stresses resolved onto {110} / <111> slip system using the Schmid factor of 0.634 and divided by a shear modulus, G, versus pillar diameter with D, normalized by the Burgers vector, b, at each temperature. We used the Burgers vector b of 0.2526 nm, calculated based on $|b| = a/2 < 110 >$ and G of 75 GPa, common for FeCr alloys [27]. This plot reveals a power-law dependence of $\tau/G = A(D/b)^{-m}$ where m is the size effect exponent that

demarks each isothermal size effects plot. It is evident that in the FCC samples, the size effect exponent decreased with temperature, from -0.68 for 295 K to -0.47 for 143 K, and -0.38 for 40 K.

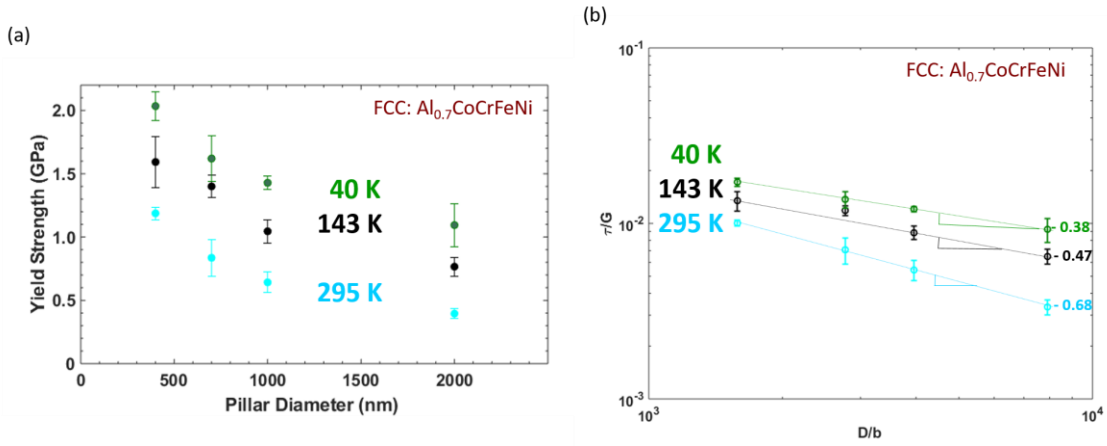

Figure 4.3(a)Un-normalized size dependence plot of yield strength vs pillar diameter of FCC pillars (b) Normalized size dependence plot of resolved shear stress vs pillar diameter of FCC pillars.

Figure 4.4 (a) shows the plot of the yield stress, defined as stress at 0.2 % offset of the strain, of [001]-oriented BCC pillars versus pillar diameter deformed at each temperature. This yield strength was obtained from the stress-strain data for each pillar, examples of which are shown in Fig. 4.2 (a-c). Error bars in Figure 4.4 (a) represent the range of stresses for each pillar dimension. This plot clearly demonstrates that the strengths of pillars of all sizes marginally increased with the reduction in temperature, and that the highest strength in excess of 3.2 GPa was attained by samples with the smallest diameters of ~ 400 nm at 40 K, and ~ 2 μm-diameter pillars deformed at room temperature had the lowest strength of ~ 1.5 GPa MPa. Figure 4.4 (b) shows a log-log plot of these yield stresses resolved onto {110} / <111> slip system using the Schmid factor of 0.408 and divided by a shear modulus, G, versus pillar diameter with D, normalized by the Burgers vector, b, at each temperature. We used the Burgers vector b of 0.2484 nm, calculated based

on $|b| = \sqrt{3}\,a/2 \ <111>$, and G of 70 GPa, common for NiAl alloys [28]. This plot reveals a power-law dependence of $\tau/G = A(D/b)^{-m}$ where m is the size effect exponent that demarks each isothermal size effects plot. It is evident that in the BCC samples, the size effect exponent remains the same as m = - 0.33 at all the temperatures studied.

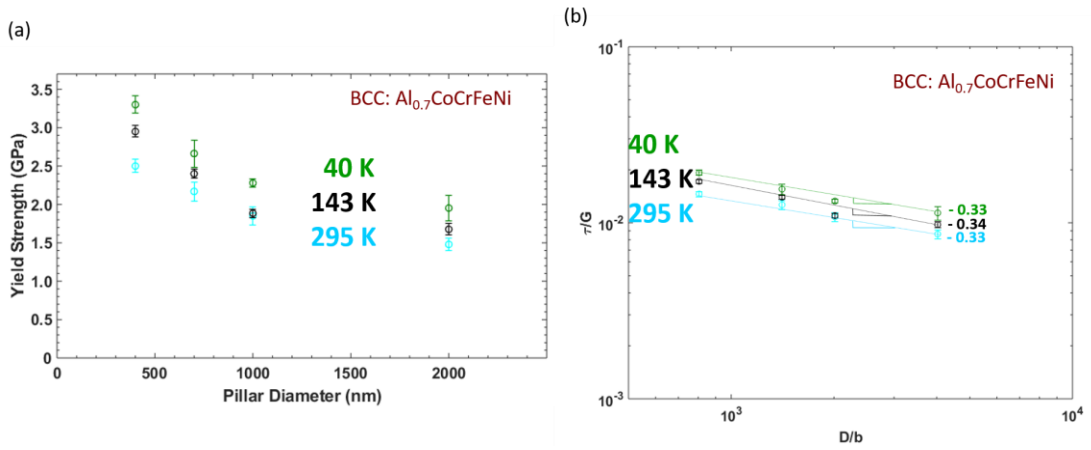

Figure 4.4 (c) Un-normalized size dependence plot of yield strength vs pillar diameter of BCC pillars (d) Normalized size dependence plot of resolved shear stress vs pillar diameter of BCC pillars.

Figure 4.5 (a-c) shows bright field (BF), as well as High Resolution (HR) TEM images of the [324]-oriented 2 µm-diameter pillars deformed at 295 K, 143 K, and 40 K, respectively, with their diffraction patterns shown as insets. This was taken from the red-circled region in Figure 4.5 (a-c) from the region where slip activity occurred. These images reveal the presence of multiple parallel slip lines, as well as of regions with bend contours in the BF images at all three deformation temperatures. The diffraction patterns are consistent with pure FCC phase, with no evidence of twinning at all temperatures. HRTEM images convey the presence of <111>-oriented stacking faults at 295 K (Fig. 4.5(a)) and 143 K (Fig. 4.5(b)), which may be attributed to dissociation of perfect dislocations into $1/6\langle 112\rangle$ Shockley partials. Sample deformed at 40K (Figure 4.5(c)) did not show stacking faults, instead it had distorted lattice fringes.

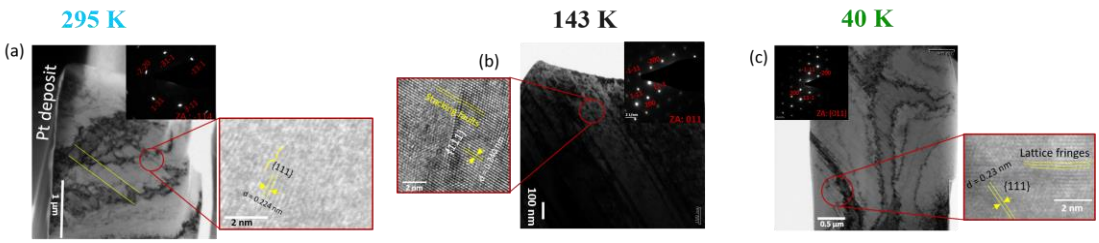

Figure 4.5 Bright field (BF) TEM images of [324]-oriented $Al_{0.7}$CoCrFeNi FCC pillars deformed at (a) 295 K,(b) 143K, and (c) 40K. High-Resolution (HRTEM) images show {111} planes and stacking faults (a, b), as well as lattice distortion (c). All diffraction patterns with labeled zone axes are shown in insets.

Figure 4.6 (a & c) shows the bright field (BF), as well as high-resolution HRTEM images of the [001]-oriented 2 µm-diameter pillars deformed at 295 K and 40 K respectively, while Figure 4.6 (b) shows the TEM image of 2 µm-diameter pillars deformed at 143 K, with their diffraction patterns shown as insets. These images reveal that deformation occur mostly in the top region of the pillar containing bend contours at all three deformation temperatures. These DPs were taken from the red-circled region on the BF/TEM images of Figures 4.6 (a-c) and are consistent with pure BCC phase indicating deformation by dislocation activity on the {110} as seen from the HRTEM image at 295 and 143 K in (Figure 4.6(a)) and (Fig. 4.6 (b)). BCC samples deformed at 40K (Fig. 4.6 (c)) shows the presence of twins in the {110} plane in the HRTEM images, and this is also confirmed by the presence of twinning diffraction spots.

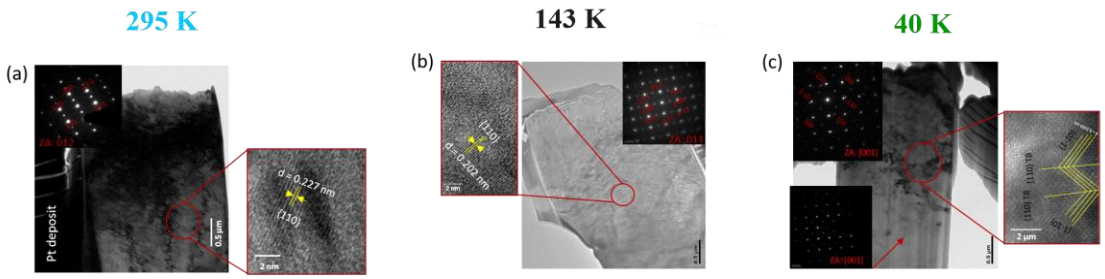

Figure 4.6 Bright field (BF) TEM images of [001]-oriented $Al_{0.7}$CoCrFeNi BCC pillars deformed at (a) 295 K,(b) 143K, and (c) 40K. High-Resolution (HRTEM) images show {110} planes and twinning deformation in (c). All diffraction patterns with labeled zone axes are shown in insets.

4.4 Discussion

4.4.1 Effect of temperature on strength

4.4.1.1 FCC phase

Strengths of FCC nanopillars fabricated from HEA are highest at the lowest temperature of 40 K for the smallest size of ~ 400 nm. Yield strength of 2.0 GPa was observed at 40 K for 400 nm-sized pillars (Figure 4.1 (c)). At lower temperatures there is less thermal activation, which leads to suppressed dislocation motion and an increase in the internal lattice friction, thereby increasing the yield stresses [50–52]. Mechanical properties of pure FCC metals have been studied to have little or no effect on temperature [52], [53]. FCC metals are known to have low lattice resistance and high strengths which are usually achieved by alloying or microstructural engineering [54,55]. As more alloying is done, defects and solute atoms/impurities are introduced as obstacles to dislocation motion, thereby increasing the strength. Our single-phase, single-crystalline FCC HEA samples here show significant strength and sensitivity to testing temperature.

Significant increases in strength with decreasing temperature have been reported for a variety of FCC HEAs [42], [54], [56–62]. Bulk FCC HEAs have been shown to have

increased yield strength compared to their pure metal counterparts due to the solid solution strengthening which includes lattice distortion and the chemical interactions of the combining metals [54], [63] ,[64]. For example, tensile strengths of 1 GPa have been reported for CrMnFeCoNi at 77 K [41] and at 700 °C, a compressive strength of 1167 MPa was reported for $CuCoNiCrAl_{0.5}Fe$ with the addition of boron (1.0) [64]. Following the trend in pure metals, the strength of FCC HEAs tend to not be as high as that of the BCC HEAs [4], suggesting that some fundamental mechanisms that control strength in less-complex alloys also control the strength in HEAs.

In addition to solution strengthening, nano-sized FCC metals have been observed to have annihilation of dislocations to the free surface followed by subsequent dislocation nucleation during plasticity [32] ,[33]. This surface-mediated plasticity also contributes to the higher stresses by shifting deformation from activation of existing dislocations to nucleation from internal or surface sources.

4.4.1.2 BCC phase

High strengths were calculated for the BCC pillars at low temperature of 40 K and also at smallest pillar size of 400nm. Yield strength of 3.2 GPa was calculated for ~ 400 nm size pillars at 40 K (Figure 4.2(c)). Generally, BCC metals are known to have higher stresses than the FCC metals due to the complex nature of their dislocation structure [33], [65–68]. BCC metals also have higher Peierls stress due to the non-planar structure of the screw dislocations [69], [70]. Bulk BCC HEAs have been reported to have yield strengths ranging from 1-1.5 GPa at room temperature [71], [72]. Post compressed images of the BCC pillars shown in Figure 4.2 (d-f) shows wavy slip lines in BCC single crystal

deformation are attributed to the cross slip events of screw dislocations to different planes of the same direction <111> [73–80].

Lee, et al [19] investigated the mechanical properties of Mo and W at 165 K and reported yield strengths of 0.65 GPa and 2.5 GPa respectively for 400 nm-sized pillars and attributed these high strengths compared to their room temperature values of 0.3 GPa and 2.0 GPa to the reduced mobility of screw dislocation at lower temperatures. Reduced screw dislocation mobility suppresses the ease of formation of kinks and forests. Indeed, the strength of several BCC metals are known to display a more significant temperature dependence than most FCC metals [81].

The 'smaller is stronger' size-effect also plays a role in the high stresses observed. This is due to the reported dislocation multiplication in small sized BCC pillars. Formation of kinks and forests occurs during the multiplication event [19], [32], [33], [67] and a suppression of this activity occurs at a low temperature, thereby increasing the stresses.

4.4.2 Effect of Temperature on Size effect

4.4.2.1 FCC phase

A universal size effect exponent of $m = 0.66$ has been established for sub-micron sized FCC single crystals [22], [32], [34, [36], [82]. The universality at room temperature is explained from the ease of dislocation motion and dislocation annihilation at the free surface. Fewer studies have been done on the size effect of pure sub-micron sized FCC metals at low temperature. Wheeler, et al studied the size effect of annealed Cu nanopillars from room temperatures to 400°C and reported a constant size effect of $m = 0.65$. It was explained that the constant size effect is attributed to negligible thermally activated contributions to stresses in that temperature range [83].

In contrast to previous reports of temperature insensitivity, we see a reduced size exponent, *m*, in the FCC phase as the temperature is reduced. The size effect exponent reduces from -0.68 to - 0.47 to - 0.38 as the temperature changes from 295 K to 143 K to 40 K.

4.4.2.2 BCC phase

Pure single crystal BCC metals have varying *m* values at room temperature, which is due to differences in critical temperatures and Peierls stresses between different BCC metals with smaller values attributed to higher Peierls stresses [32], [33], [67], [79]. Lee et al [19] studied Nb and W nanopillars at 165 K and showed a reduced size effect exponent of $m = 0.36$ and 0.19 respectively, when compared to the exponent values of 0.73 and 0.28 at room temperature [84]. He also ascribed this to the suppressed dislocation multiplication at lower temperatures [19].

In our BCC pillars, the same *m* was observed at the three test temperatures. It can be said that the dislocation structure remains relatively stable for the range of temperatures studied, making the size effect exponent invariant of temperature. The size effect exponent can be governed by other phenomenon such as single arm sources [85], [86], and this is plausible if the dislocation densities and activated slip systems during deformation remain the same [85]. More work needs to be done to establish this phenomenon in BCC HEAs.

4.4.3 Effect of temperature on slip events and work hardening

4.4.3.1 FCC phase

The stress strain data (Figure 4.1(a-c)) indicates the presence of burst events in the deformation of FCC pillars. It was observed that the intermittency of these burst events

reduces with decreasing temperature. The larger burst regime (less intermittency) suggests that when the slip event occurs, the dislocation activity continues for a longer duration at low temperature [19]. At room temperatures, frequent dislocation annihilation to the free surface leads to the intermittency of the strain bursts. Subsequent dislocation nucleation during plasticity could be increased at lower temperatures, leading to the infrequent intermittency and larger burst regime [29], [30]. Increased nucleation stresses at these lower temperatures contributes to the higher stresses [31].

Reduced work hardening was observed due to the intermittency of the bursts at room temperature; however, there are increased flow stresses after each burst events. At low temperatures, for a particularly longer burst regime, we have minimal increase or no flow stresses at all until ~ 15% strain is reached. For example, the stress-strain curves at 295 K in Figure 4.1(a) show that the first major strain burst event for a 400 nm-sized pillar occurred at a strain of 2%, then followed were by another event at 5, 9,10 and 12 % strain until the unloading event. At 143 K in Figure 4.1(b), strain hardening occurs until 5 % strain and no other strain burst activity occurred. At 40 K, apart from the burst events at yield, no other strain burst event occurred. Though multiple parallel slip lines were observed for deformed pillars at the lower temperatures, it is suggested that these multiple slip events took place within a burst regime.

4.4.3.2 BCC phase

The plastic behavior of the 2 μm-sized BCC pillar during deformation is different from the smaller specimen sizes of 1μm to 400 nm, especially at room temperature (Figure 4.2(a)). There is continuous plasticity for the large sample which is attributed to the formation of kinks and forests with minimal contribution from surface related activity

(nucleation or exhaustion). As the sample size is reduced, more surface contribution is involved, resulting in dislocation exhaustion at the free surface. As the temperature is reduced, we observe similar plastic behavior exists for smaller pillars size, particularly the 700 nm and 1 μm size specimens. The similarity in plastic behavior of 2 μm size pillars at room temperature and smaller sizes at cryogenic temperature could be due to prolonged dislocation activity due to suppressed multiplication at low temperature [19].

4.4.4 Microstructural analysis of the deformed pillars

4.4.4.1 FCC phase

From Figure 4.5 (a-c), we observed dislocation-driven deformation via slip bands in the Bright field (BF) images and the absence of addition deformation mechanism such as twinning spots in the diffraction patterns at all the temperatures studied. Pure FCC metals at the nanoscale have been reported to undergo dislocation mediated nanoplasticity at room temperature [22], [32–36], but mechanical twinning has been reported in Ag pillars [37], [38] at room temperature. Belwitt, et. al studied the deformation of bulk single crystal FCC metals (Cu, Al, Ag, Au) and observed mechanical twinning at temperatures of 4.2 K and ~78 K [39]. It was reported that twinning occurs at orientations about 3 to 5 degrees from [111]. They also reported the lack of such twinning deformation for Pb and Al single crystals at low temperatures for the same orientations studied [39], [40]. It is inferred that orientation and the intrinsic properties of the material play a role in twinning activity. Deformation of bulk FCC HEAs has been reported to be controlled via dislocation motion at room temperature [41], while mechanical twinning has been reported in CoCrFeMnNi deformed at 20% strain at 77 K [42] and for $Fe_{40}Mn_{40}Co_{10}Cr_{10}$ deformed up to ~ 45% strain at room temperature [43].

The lack of a change in the deformation mechanism of [324] FCC nanopillars at the three test temperatures can be attributed to orientation dependent twinning deformation. Kireeva, et. al [44] studied the orientation effects on the tensile deformation of [001], $[\bar{1}23]$, and $[\bar{1}11]$ bulk single crystals of CoCrFeMnNi HEA at room temperature and observed differences in the deformation behavior of these crystals. Samples with a [001] orientation deformed via dislocation glide, while samples with $[\bar{1}23]$ or $[\bar{1}11]$ orientation underwent both glide and deformation twinning but twinning emergence at different strains, 25 % and 5 % for each orientation, respectively. They attributed these differences to the ratio of the Schmid factor of twinning (m_{tw}) to the Schmid factor of slip (m_{sl}). Ease of twinning deformation occurs in $\frac{m_{tw}}{m_{sl}} > 1$ [44]. They later observed twinning in the [001] single crystal of the same HEA at 77 K [45]. We can apply the ratio $\frac{m_{tw}}{m_{sl}}$ to the study of the FCC pillars where $m_{tw} = -0.2188$ using the most commonly observed twin system of (111) $[11\bar{2}]$ in FCC metals, $m_{sl} = 0.634$. The $\frac{m_{tw}}{m_{sl}} = -0.345$ makes twinning difficult in this orientation. Twinning commonly observed in polycrystalline FCC metals and polycrystalline HEAs can also be aided by the presence of grain boundaries.

4.4.4.2 BCC phase

Several deformation mechanisms have been reported to occur for single crystal BCC metals at different temperatures. Cross-slip events of dislocation multiplication have been described as the main activity at room temperature for BCC metals [32], [33]. Weinberger, et. al [46] summarized the slip planes of single crystal BCC metals at different temperatures. For example, slip in Mo occurs on {110} at 4.2 K and both the {110} and {112} at 77 K and predominantly {110} slips at room temperature. Most BCC metals

exhibit compression/tension asymmetry depending on crystal orientation and temperatures, either exhibiting slips or twins at low temperature. Wang, et al [47] observed twinning during in-situ deformation of 100 nm W pillars at room temperature with the twinning system identified as [111]/{112}. The ordered BCC B2 crystal structure has also been studied to have an anti-twinning mode of shear which causes dislocation glide in the opposite direction [48]. More work must be done to establish the twinning mechanisms in BCC HEAs at lower temperatures.

Bulk BCC HEAs have not been extensively studied at low temperatures, although BCC AlCoCrFeNi has been shown to have excellent yield strength at 77K. Any information about changes in deformation mechanism was not reported [49].

4.5 Molecular Dynamics Simulations

We employed molecular dynamics simulations to understand the atomic deformation mechanisms of a representative FCC and BCC HEA nanopillar under compression. To construct the initial sample, we create a cylindrical geometry with the axis aligned along the [324] crystallographic direction for the FCC sample and along the [001] crystallographic direction for the BCC sample to match experimental crystallographic axes. The initial sample was monatomic and the HEA was created by randomly replacing atomic species to achieve an equi-atomic composition. The dimensions of the cylinders were 30 nm in diameter with a length of 90 nm. The direction parallel to the cylinder axis was periodic and the 2 directions perpendicular to the axis were free surface boundaries. The energy of the initial structures was minimized following a conjugate gradient scheme. The system was then assigned a velocity profile corresponding to the simulation temperature of 50 K, 143 K, or 300 K. The pillars were then equilibrated for 200 ps at the

assigned temperature and zero pressure along the axial direction followed by equilibration for 200 ps under time integration of the NVE ensemble. All simulations were performed using an integration timestep of 1 fs. Compression was performed by deforming the simulation box at a strain rate of 108 s-1 up to at least 15% total strain.

Stacking fault energy calculations were performed following standard methodology [23]. A block with dimensions 12.5x12.5x20 nm with equi-atomic composition was constructed and relaxed. The energy of this initially-relaxed sample was taken as the reference energy for calculation of the stacking fault energy. The stacking fault plane was aligned with z-axis and given a free surface boundary condition and the two perpendicular directions were given periodic boundary conditions. For the FCC HEA, the stacking fault plane was [111] and the fault direction was $\langle 11\bar{2} \rangle$. For the BCC HEA, the stacking fault plane was $[11\bar{2}]$ and the fault direction was $\langle \bar{1}\bar{1}1 \rangle$. The top half of the block was displaced in the fault direction by a fraction of the Burgers vector and the total energy was calculated while keeping the atoms fixed. This was repeated along the entire length of periodicity in the fault direction. The stacking fault energy was calculated as the difference between the energy and reference energy, normalized by the area of the stacking fault plane: $\gamma_{SFE} = \frac{E-E_0}{A}$. This results in the unrelaxed stacking fault curve. This procedure was repeated but allowing atoms to relax in the direction normal to the stacking fault plane producing the relaxed stacking fault curve.

Representative FCC and BCC HEA compositions were chosen based on (1) similarity to experimental composition, (2) availability of interatomic potentials, and (3) energetic and mechanical lattice stability. Following these requirements, we implement the EAM potential developed by Zhou, et al. [24] and choose the equi-atomic CoFeNiPd

system as our representative FCC HEA and the equi-atomic AlMoWTa system as our representative BCC HEA. All simulations were performed using the LAMMPS molecular dynamics software [25] and OVITO [26] was used for common neighbor analysis, calculation of atomic shear strain, and visualization.

4.5.1 Simulated compression of a representative FCC HEA

To better understand the atomistic mechanisms underlying the strength and temperature dependence observed experimentally, we performed compression simulations on representative HEA systems. Figure 4.7 (a-c) shows the local atomic shear strain for the 30 nm-diameter FCC HEA samples compressed at 300 K, 143 K, and 50 K. These shear strain snapshots correspond to the initial nucleation event. The maximum engineering stress (and strain at max stress) is 3.93 GPa (0.028), 3.72 GPa (0.028), and 3.64 GPa (0.028) for 50 K, 143 K, and 300 K respectively. The average stress from 0.06 to 0.15 strain was calculated as 2.26, 2.14, and 2.21 GPa for 50 K, 143 K, and 300 K respectively. We refer the reader to the supplemental material, Figure B.1(a), for the output stress-strain data. These simulations reveal that failure occurs via nucleation of a $1/6\langle 112\rangle$ partial dislocation on a nanopillar surface. A trailing partial nucleates with further straining, which creates a fully dissociated pair of partial dislocations, which then glides along the (111) slip plane across the diameter and annihilates at the opposite surface. Further plastic deformation proceeds via partial dislocation nucleation from the surface on planes adjacent to the previously sheared slip planes. Nucleation of partial dislocations was observed to the primary mechanism of deformation at all temperatures. These figures indicate that slip occurred on a set of parallel slip planes that correspond to the plane with the greatest resolved shear stress. Based on the average stress at high strain and highly localized shear

profiles in Figures 4.7 (a-c), it is clear that the initial set of slip planes become favorable sources of dislocations. As seen in Figures 4.7 (a-c), no cross-slip of dislocations occurred at any temperature. This is likely because the partial dislocation pairs remained dissociated throughout glide until annihilation at the opposing surface.

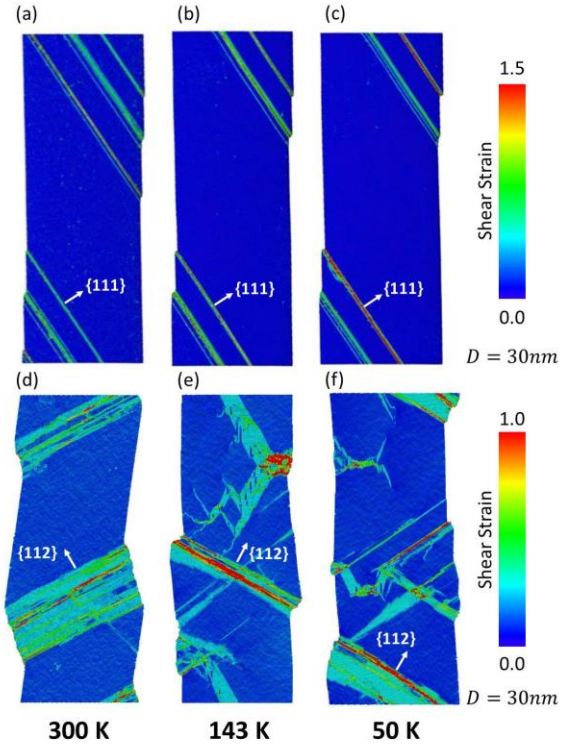

Figure 4.7 (a)-(c) shows the atomic shear strain of our representative FCC HEA following the initial stress drop at 50 K, 143 K, and 300 K. Deformation is dominated by the nucleation of partial dislocations that traverse the diameter of the pillar. Slip is strongly planar, occurring along a set of parallel slip planes. Figure 4.7 (d)-(f) shows the atomic shear strain of our representative BCC HEA following the initial stress drop at 50 K, 143 K, and 300 K. Deformation is dominated by nucleation of partial dislocations that grow into twinned regions and nucleate full dislocations. At 50 K and 143 K, multiple slip systems are activated while slip at 300 K is confined to a set of parallel slip planes.

Figure 4.7 (a-c) corresponds well with the post-deformation SEM images shown in Figure 4.1 (d-f). Both post-deformation morphologies indicate that FCC HEA single crystals deform via parallel planar shear offsets, indicating highly localized plasticity at all temperatures. Figure 4.5 (a-c) suggests that the underlying atomic mechanisms of

deformation in the FCC HEA are dislocation driven. Indeed, our MD simulations show that the shear planes shown in Figure 4.7 (a-c) are a result of the glide of dissociated dislocation partial pairs. Dissociation of full dislocations would prevent cross-slip, promoting planar, localized plasticity and reducing strain hardening. Such dissociated partial pairs have been suggested in previous experiments on HEAs to prevent cross-slip and promote planar dislocation structures [42,87,88].

4.5.2 Simulated compression of a representative BCC HEA

Figure 4.7 (d-f) shows the atomic shear strain for the BCC HEA samples compressed at 300 K, 143 K, and 50 K. These shear strain snapshots correspond to the point of minimum stress following the stress drop from maximum stress. The maximum stress (and strain at max stress) is 12.84 GPa (0.085), 12.14 GPa (0.082), and 11.10 GPa (0.078) for 50 K, 143 K, and 300 K, respectively. The average stress from 0.1 to 0.175 strains was calculated as 3.03, 1.73, and 1.60 GPa for 50 K, 143 K, and 300 K, respectively. We refer the reader to the supplemental material, Figure B.1(b), for the output stress-strain data. The maximum stress corresponds to the nucleation of partial dislocations on (112) planes. These partials nucleate on successive planes and form an I_3 fault which contains 2 twinned planes separated by 3 atomic layers [89]. Ahead of this fault, full dislocations and partial dislocations are nucleated. Further plastic deformation results in nucleation of dislocations from deformed regions and thickening of twinned regions via nucleation and glide of 1/3<111> partial dislocations along the boundaries of the twinned region. Due to the high symmetry of the (001) loading in the simulated BCC HEA, several slip systems are activated. At 143 K and 50 K, we observe the intersection of several slip systems. In

comparison to the FCC HEA, bands of shear strain are much thicker. These bands correspond to twinned regions that grew from I_3 faults that nucleate from the surface.

Both Figure 4.7 (d-f) and Figure 4.2 (d-f) indicate homogeneous deformation in both the experiment and simulation BCC HEA single crystals at all temperatures. Figure 4.7 (d-f) show not only dislocations, but the presence of twins in the deformed BCC HEA. Consistent with these experimental observations, our MD simulations show that deformation in our simulated BCC HEA is driven by partial dislocations, full dislocations, and twinning.

4.5.3 Calculation of stacking fault energy

Dislocation dissociation, the nucleation of partial dislocations, and twinning are all known to be dependent upon the stacking fault energy [89–91]. To understand how the stacking fault energy of our HEA systems compares against pure metals, we calculated both the unrelaxed and relaxed stacking fault curves for our simulated FCC and BCC HEAs.

Figure 4.8 (a-b) shows the unrelaxed stacking fault curves for our representative FCC and BCC HEA. The series of curves shows the stacking fault curves for a series of monatomic and alloy systems composed of constituent elements from the FCC and BCC HEA systems, as well as the stacking fault curves for our representative FCC and BCC HEAs. In Figure 4.8 (a), the stable stacking fault energy decreases monotonically with increasing alloying. The stable stacking fault in the FCC HEA is 25.4 mJ/m^2, which is 70% and 64% less than the stable stacking fault energy of Pd and Ni. The unstable stacking fault energy of the FCC HEA is also significantly less than the unstable stacking fault energy in Pd and Ni, but slightly greater than in the $Pd_{50}Ni_{50}$ and $Pd_{33}Ni_{33}Co_{33}$ alloys. There is no

stable stacking fault energy in the BCC system, but Figure 4.8 (b) shows that the overall stacking fault curve decreases monotonically with increasing alloying. The unstable stacking fault energy of the BCC HEA is 658 mJ/m^2 which is 50% less than the unstable stacking fault in BCC W. Figure 4.8 (c)-(d) shows the relaxed stacking fault curves. The relaxed curves show an overall decrease in energy as compared to the unrelaxed curves, but qualitatively show little change.

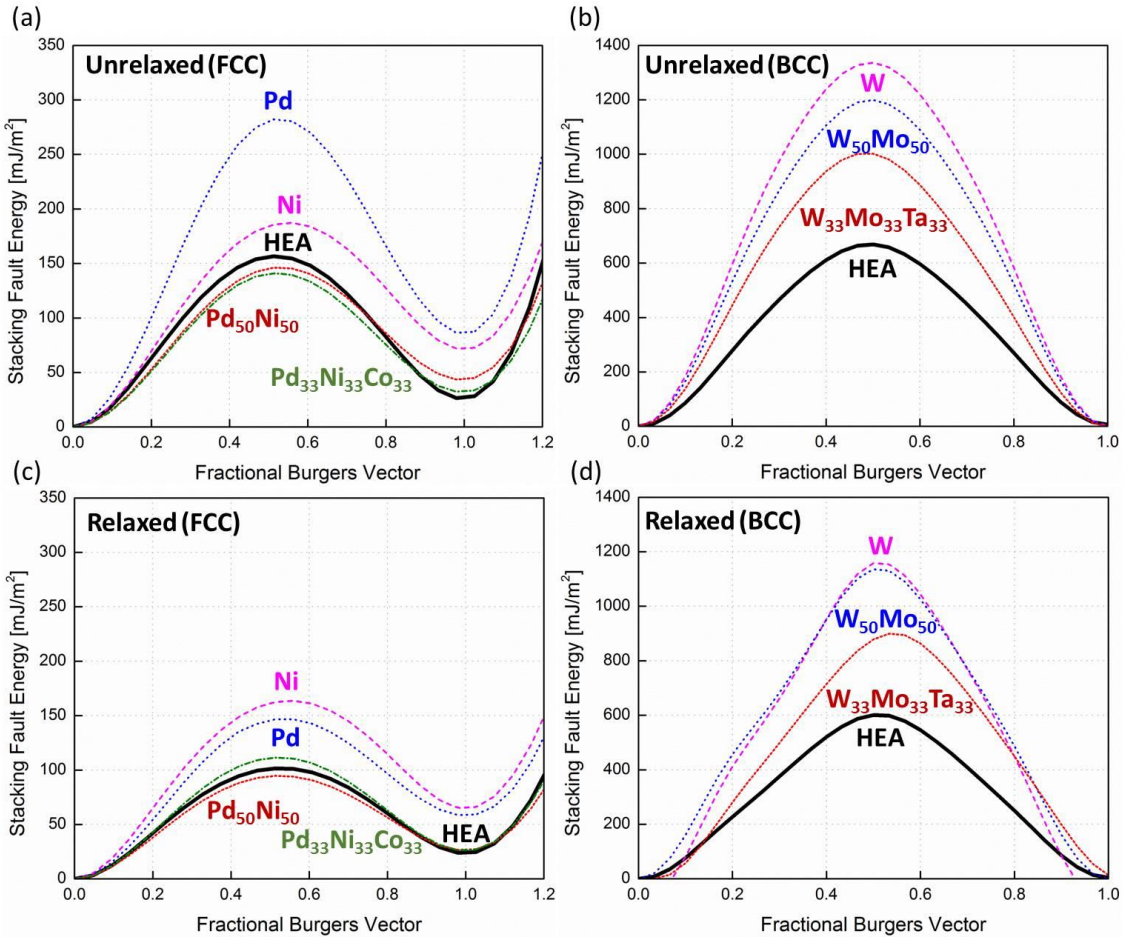

Figure 4.8 (a)-(b) shows the unrelaxed stacking fault energy in our representative FCC and BCC HEAs. For the FCC HEA, we consider slip on the [111] plane in the <110> direction. Corresponding the deformation observed in compression simulations, we consider slip on the [112] plane in the <111> direction for our representative BCC HEA. In both the FCC and BCC HEA, increasing alloying significantly decreases the stacking fault energy. Figure 4.8 (c)-(d) shows the same data but allowing the system to relax in the direction perpendicular to the slip plane.

Several stacking faults in the FCC phase were reported here and have been frequently observed in several other HEA systems suggesting that it is a general feature in such alloys [42], [61, [87], [92], [93]. Our MD calculations show that HEAs have significantly lower stacking fault energy as compared to their pure counterparts. Such low stacking fault energy promotes the presence of dissociated partial dislocations in our FCC HEAs (preventing cross-slip and promoting planar, local deformation) and deformation twinning.

4.6 Modeling Size-Dependent Strength of HEA as a function of Temperature

4.6.1 Sources of strengthening and temperature dependence in HEA

The expected factors contributing to higher stresses in this study can be summarized as solid solution strengthening of the HEAs, the size-dependent source contribution, and dislocation forest interactions. These contributions to shear stress at a small scale can be represented [85], [86], [94] as,

$$\tau = \tau^* + \tau_G + \tau_{source} \tag{4.2}$$

where τ^* is the contribution from lattice friction, τ_G is the contribution from Taylor hardening, and τ_{source} is the contribution from the single–arm sources. The contributions from Taylor hardening and size-dependent sources are not dependent on temperature [94], [95]. It then is reasonable to only consider the temperature dependence of the lattice friction.

A few models have been put forward to explain the temperature dependence of FCC HEAs [54], [57], [96], [97]. The chief approach to explain the temperature strengthening in HEAs has been to consider thermally-activated flow. The strength related to internal lattice friction can be generally expressed as [98]:

$$\frac{\tau^*(T)}{\tau^*(0)} = \frac{k_B T}{\Delta \mathrm{E}} \ln\left(\frac{\dot{\varepsilon}}{\dot{\varepsilon}_0}\right) + 1 \qquad (4.3)$$

$\tau^*(0)$ is the athermal strength, ΔE is the activation energy required for a dislocation to overcome the dominant obstacle, $\dot{\varepsilon}$ is the experimental strain rate, $\dot{\varepsilon}_0$ is a reference strain rate related to the velocity of mobile dislocations, and k_B is Boltzmann's constant. To predict strength as a function of temperature then requires knowledge of $\tau^*(0)$ and ΔE for the relevant strengthening mechanism.

In conventional metallic solid solutions, the obstacles to dislocation motion are the solute atoms. This is clearly complicated in HEAs where no single element dominates and the definition of "solute" is not straightforward. Most approaches begin with the classical Labusch model for solid strengthening in a binary alloy [99] and extend it for use in HEAs. In the Labusch model, strengthening arises from the interaction of a dislocation with several randomly dispersed solutes on its glide plane. In contrast to theories of strong-pinning, the solutes in the Labusch model are not individually strong enough to pin a dislocation, but the combined interactions of many solutes act to resist the dislocation. Varvenne, et al previously developed a model that considers the interaction of a dislocation with solute atoms on and off its glide plane and also allowed for an arbitrary number of solutes at arbitrary concentration [97]. Under simplifications of the solute/dislocation interaction energy, their model predicts analytic expressions for $\tau^*(0)$ and ΔE.

In contrast to these thermally-activated models of temperature-dependent strength, Wu, et al suggested that strengthening in HEAs may arise due to the temperature dependence of the dislocation core width [54]. They adopt the Peierls-Nabarro (P-N) picture of the dislocation and assume a linear temperature dependence of the dislocation width. Athermal strength is then predicted via the P-N model and strength is predicted to

decrease exponentially with temperature but contains parameters that must ultimately be fit to data.

4.6.2 Comparison of strengthening models to FCC phase

We would like to compare the predicted strengths of these two models to the strength of our FCC HEA. The Labusch-type strengthening model requires several mechanical properties and atomic volumes as input to the model. For the FCC phase of the $Al_{0.7}$CoCrFeNi HEA studied here, we use $\mu = 75\ GPa$ and $\nu = 0.28$ [54]. We use previously reported atomic volumes of Co, Cr, Fe, Ni in a CoCrFeNi alloy of $V_{Co} = 11.12\ Å^3$, $V_{Cr} = 12.27\ Å^3$, $V_{Fe} = 12.09\ Å^3$, and $V_{Ni} = 10.94\ Å^3$ [97]. By applying Vergard's law between the lattice parameter of the CoCrFeNi and the lattice parameter of the FCC phase in our $Al_{0.7}$CoCrFeNi, we obtain an atomic volume for Al of $V_{Al} = 13.71\ Å^3$. We apply the above elastic constants for the Peierls-Nabarro model, and following the analysis of Wu, et al, we choose the 0 K dislocation width to be equal to the Burgers vector magnitude, $\omega_0 = b$. We can estimate the bulk strength of our experimental FCC HEA by extrapolation of the size dependent power law to 20 μm. This corresponds to the expected length scale at which dislocation multiplication changes from single-arm to double-arm sources.

Figure 4.9 shows the extrapolated bulk strength from our experimental data, the predicted temperature dependence of the Labusch model, the predicted 0 K temperature as predicted via the P-N model, and the exponential curve fit from the model suggested by Wu, et al. Figure 8 shows that the Labusch model predicts the room temperature strength of our FCC HEA very well but significantly under-predicts the strength at cryogenic temperatures. From the exponential curve fit, we see that the experimental data approaches

the 0 K strength as predicted from the P-N model. This suggests that at low temperatures, Angstrom-level fluctuations in the dislocation line (which are neglected in the modified Labusch model) become increasingly important, effectively decreasing the width of the local potential well. Although the low temperature strength is better captured by the P-N mechanism, to achieve the temperature decrease from 0 to 300 K as indicated by the curve fit would require an increase in the dislocation core width of 30%.

Attempts to identify the controlling mechanism of this strengthening have focused on measuring the activation volume of these FCC HEAs. The activation volume, which is typically reported in units of b^3 where b is the Burgers vector, for the dominant yield mechanism in FCC HEAs has been reported to be on the order of 10-60b^3 at cryogenic temperatures (73 – 77 K) and 100-360b^3 at room temperature. These values are far below typical room temperature values of FCC metals (100-1000b^3) and closer to the activation volume for kink-pair propagation in BCC metals (1-100b^3) [57], [60], [62]. Despite the low activation volume, no significant anisotropy between the mobility of screw or edge dislocations was observed in a FCC HEA [87], suggesting that the kink-pair propagation mechanism used to explain the temperature dependence of the size effect exponent in BCC metals is likely not applicable here. More work is required to identify the relevant mechanisms and temperature ranges control the strengthening in FCC HEAs.

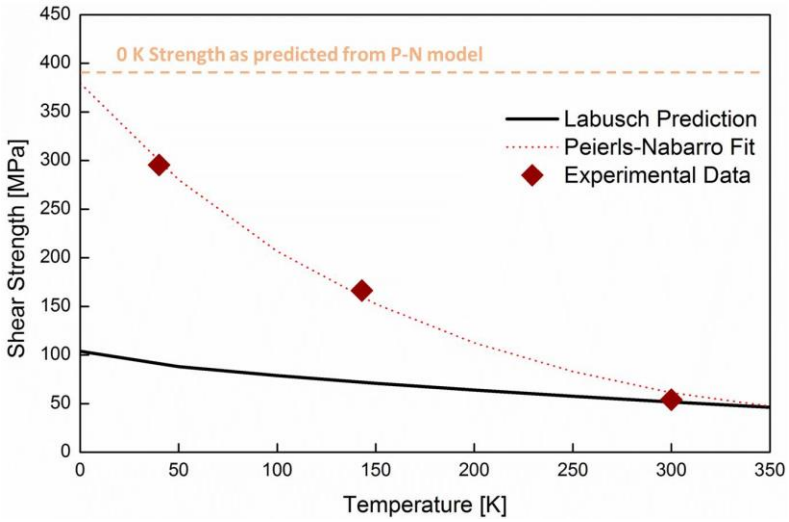

Figure 4.9 compares the bulk shear strength of the FCC phase of our HEA obtained by extrapolation of the size dependent data. We see that the thermally-activated Labusch model (Varvenne-Curtin) predicts the room temperature strength very well but significantly under-predicts the low temperature strength. The P-N model (Wu-Pharr-George) provides a much better prediction at 0 K. This suggests that at low temperatures, Angstrom-level fluctuations (neglected in the Labusch model) in the dislocation become increasingly important, which effectively decreases the width of the local potential well.

4.6.3 Strengthening in BCC phase

Along with strengthening due to the spinodal microstructure of the A2+B2 phase [100], the low size effect exponent is consistent with previously reported size effects in BCC metals [32]. The higher yield stresses obtained in the [001] BCC HEA nanopillars can be said to arise from the heavily distorted BCC phase of the $Al_{0.7}$CoCrFeNi HEA. The elemental analysis in the BCC phase indicates the 30.3 $\pm$ 3.1 at.% of Al and 25.6 $\pm$ 3.3 at. % of Ni than the other combining Transition Metals (TMs) [20]. Al has an atomic size of 1.43 Å while the other TMs are ~1.25 Å, hence the distortion [20]. This high distortion leads to high lattice resistance.

4.6.4 Origin of temperature dependence in the size exponent

Temperature dependence of the size effect has been previously observed in BCC metals [19], [81], [101], but not typically in FCC metals. In BCC metals, this arises due to the temperature sensitivity of screw dislocation mobility [81]. Motion of screw dislocations in BCC metals proceeds by the passage of kink-pairs over the Peierls barrier. At temperatures near the critical temperature, kink-pairs can easily overcome this barrier, and screw dislocations in BCC metals have high mobility and glide similar to dislocations in FCC metals. With decreasing temperature, overcoming the Peierls barrier becomes more difficult, effectively increasing the internal lattice friction. An increase in τ^* in Equation (2), which is fit to a power law to give the size effect exponent, then results in a decrease in the fit exponent.

From the discussion in Section 4.6.2, we conclude that the decreasing size effect with temperature for the FCC phase reported here is directly related to increasing lattice friction with decreasing temperature. In contrast, the BCC phase shows a constant low size effect exponent at all temperatures. It has been estimated that the critical temperature in a BCC HEA is far above their pure constituent elements [86]. The temperature insensitivity of the size effect exponent in the BCC phase is likely due to high lattice strength at room temperature.

4.7 Summary and Conclusion

In this study, we observed higher yield stresses in the single crystals of [324] and [001] orientation of the FCC and BCC phase respectively of the $Al_{0.7}$CoCrFeNi HEA. These high stresses are due to the solid solution effect of the HEAs, surface contribution of the sub-micron sized specimen, and the effect of low temperatures. We observed a

temperature dependent size effect exponent in the [324] FCC pillars. The exponent value *m* reduces as the temperature reduces due to an increasing lattice friction. The *m* value of the [001] phase of the BCC pillars remains constant with temperature, suggesting relatively stable behavior of the dislocation structure. The microstructural analysis of the deformed pillars indicates that the FCC pillars undergo dislocation-mediated plasticity for all the test temperatures, while the BCC pillars have dislocation activities at 295 K and 143 K and the presence of twinning deformation at 40 K.

Molecular dynamics simulations show dislocation-dominated deformation in a representative FCC HEA and dislocation/twinning deformation in a representative BCC HEA. Calculation of the stacking fault energy in both the representative FCC and BCC HEA suggest that the high alloying in these HEAs promotes these deformation mechanisms. By reviewing current models for temperature-dependent strengthening in FCC HEAs, our experimental results suggest that room temperature strengthening occurs via a Labusch-type solid solution strengthening, while at lower temperatures is controlled by the local dislocation structure.

References

[1] C. L. Tracy, S. Park, D. R. Rittman, S. J. Zinkle, H. Bei, M. Lang, R. C. Ewing, and W. L. Mao, "High pressure synthesis of a hexagonal close-packed phase of the high-entropy alloy CrMnFeCoNi," *Nat. Commun.*, vol. 8, 2017.

[2] O. N. Senkov, J. M. Scott, S. V. Senkova, F. Meisenkothen, D. B. Miracle, and C. F. Woodward, "Microstructure and elevated temperature properties of a refractory TaNbHfZrTi alloy," *J. Mater. Sci.*, vol. 47, no. 9, pp. 4062–4074, 2012.

[3] B. Gludovatz, A. Hohenwarter, D. Catoor, E. H. Chang, E. P. George, and R. O. Ritchie, "A fracture-resistant high-entropy alloy for cryogenic applications," *Science (80-.).*, vol. 345, no. 6201, pp. 1153–1158, 2014.

[4] R. Fritz, D. Wimler, A. Leitner, V. Maier-Kiener, and D. Kiener, "Dominating deformation mechanisms in ultrafine-grained chromium across length scales and temperatures," *Acta Mater.*, vol. 140, pp. 176–187, 2017.

[5] B. Bhushan, *Nanotribology and Nanomechanics: An Introduction: Fourth Edition*. 2017.

[6] A. S. Schneider, "Mechanical Properties of Small-Scale BCC Metal Structures," 2010.

[7] L. E. E. Seok-woo, C. Yintong, R. Y. U. Ill, G. J. R, S. W. Lee, Y. Cheng, I. Ryu, and J. R. Greer, "Cold-temperature deformation of nano-sized tungsten and niobium as revealed by in-situ nano-mechanical experiments," *Sci. China Technol. Sci.*, vol. 57, no. 4, pp. 652–662, 2014.

[8] A. Giwa, P. K. Liaw, K. A. Dahmen, and J. R. Greer, "Microstructure and Small-scale Size Effects in Plasticity of Individual Phases of Al 0 . 7 CoCrF eN i High Entropy Alloy."

[9] L. E. E. Seok-woo, C. Yintong, R. Y. U. Ill, and G. J. R, "Cold-temperature deformation of nano-sized tungsten and niobium as revealed by in-situ nano-mechanical experiments," vol. 57, no. 4, pp. 652–662, 2014.

[10] L. Temperatures, "Low Temperatures," *Phys. Today*, vol. 10, no. 7, p. 54, 1957.

[11] Z. S. Basinski and J. W. Christian, "Mechanical Properties of Metals at Low Temperatures," in *Advances in Cryogenic Engineering*, Boston, MA: Springer US, 1960, pp. 90–92.

[12] D. A. Wigley, *Mechanical Properties of Materials at Low Temperatures*. 1971.

[13] R. M. Brick, J. R. J. Low, and C. H. Lorig, *Behavior of Metals At Low Temperatures*. American Society for Metals, 1953.

[14] M. F. Ashby and H. J. Frost, "Deformation-mechanism maps," *Oxford Pergamon Press.*, pp. 44–45, 1982.

[15] Z. Wu, H. Bei, G. M. Pharr, and E. P. George, "Temperature dependence of the mechanical properties of equiatomic solid solution alloys with face-centered cubic crystal structures," *Acta Mater.*, vol. 81, pp. 428–441, 2014.

[16] S. I. Rao, C. Woodward, T. A. Parthasarathy, and O. Senkov, "Atomistic simulations of dislocation behavior in a model FCC multicomponent concentrated solid solution alloy," *Acta Mater.*, vol. 134, pp. 188–194, Aug. 2017.

[17] F. Otto, a. Dlouhý, C. Somsen, H. Bei, G. Eggeler, and E. P. George, "The influences of temperature and microstructure on the tensile properties of a CoCrFeMnNi high-entropy alloy," *Acta Mater.*, vol. 61, no. 15, pp. 5743–5755, 2013.

[18] Z. Wu, Y. Gao, and H. Bei, "Thermal activation mechanisms and Labusch-type strengthening analysis for a family of high-entropy and equiatomic solid-solution alloys," *Acta Mater.*, vol. 120, pp. 108–119, Nov. 2016.

[19] Z. Wu, Y. F. Gao, and H. Bei, "Single crystal plastic behavior of a single-phase, face-center-cubic-structured, equiatomic FeNiCrCo alloy," *Scr. Mater.*, vol. 109, pp. 108–112, Dec. 2015.

[20] Z. Wu, H. Bei, F. Otto, G. M. Pharr, and E. P. George, "Recovery, recrystallization, grain growth and phase stability of a family of FCC-structured multi-component equiatomic solid solution alloys," *Intermetallics*, vol. 46, pp. 131–140, Mar. 2014.

[21] S. I. Hong, J. Moon, S. K. Hong, and H. S. Kim, "Thermally activated deformation and the rate controlling mechanism in CoCrFeMnNi high entropy alloy," *Mater. Sci. Eng. A*, vol. 682, pp. 569–576, Jan. 2017.

[22] I. Kireeva, Y. Chumlyakov, Z. Pobedennaya, and A. Vyrodova, "Temperature dependence of mechanical properties in [1¯11]-oriented single crystals of CoCrFeNiAl0.3 high entropy alloy," 2017, p. 20083.

[23] G. Laplanche, J. Bonneville, C. Varvenne, W. A. Curtin, and E. P. George, "Thermal activation parameters of plastic flow reveal deformation mechanisms in the CrMnFeCoNi high-entropy alloy," *Acta Mater.*, vol. 143, pp. 257–264, Jan. 2018.

[24] Y. Qiu, S. Thomas, M. A. Gibson, H. L. Fraser, and N. Birbilis, "Corrosion of high entropy alloys."

[25] C. Hsu, J. Yeh, S. Chen, and T. Shun, “Wear resistance and high-temperature compression strength of Fcc CuCoNiCrAl0.5Fe alloy with boron addition,” *Metall. Mater. Trans. A*, vol. 35, no. 5, pp. 1465–1469, 2004.

[26] B. Gludovatz, A. Hohenwarter, D. Catoor, E. H. Chang, E. P. George, and R. O. Ritchie, “A fracture-resistant high-entropy alloy for cryogenic applications,” *Science (80-.).*, vol. 345, no. 6201, pp. 1153–1158, 2014.

[27] Y. Zhang, T. T. Zuo, Z. Tang, M. C. Gao, K. A. Dahmen, P. K. Liaw, and Z. P. Lu, “Microstructures and properties of high-entropy alloys,” *Prog. Mater. Sci.*, vol. 61, no. October 2013, pp. 1–93, Apr. 2014.

[28] J. R. Greer and J. T. M. De Hosson, “Plasticity in small-sized metallic systems: Intrinsic versus extrinsic size effect,” *Prog. Mater. Sci.*, vol. 56, no. 6, pp. 654–724, 2011.

[29] S. Brinckmann, J. Y. Kim, and J. R. Greer, “Fundamental differences in mechanical behavior between two types of crystals at the nanoscale,” *Phys. Rev. Lett.*, vol. 100, no. APRIL, pp. 1–4, 2008.

[30] C. R. Weinberger and W. Cai, “Surface-controlled dislocation multiplication in metal micropillars,” *Proc. Natl. Acad. Sci.*, vol. 105, no. 38, pp. 14304–14307, 2008.

[31] J. Y. Kim, D. Jang, and J. R. Greer, “Crystallographic orientation and size dependence of tension-compression asymmetry in molybdenum nano-pillars,” *Int. J. Plast.*, vol. 28, no. 1, pp. 46–52, 2012.

[32] J.-Y. Kim and J. R. Greer, “Size-dependent mechanical properties of molybdenum nanopillars,” *Appl. Phys. Lett.*, vol. 93, no. 10, p. 101916, 2008.

[33] a. S. Schneider, C. P. Frick, B. G. Clark, P. a. Gruber, and E. Arzt, “Influence of orientation on the size effect in bcc pillars with different critical temperatures,” *Mater. Sci. Eng. A*, vol. 528, no. 3, pp. 1540–1547, 2011.

[34] V. Vitek, “Structure of dislocation cores in metallic materials and its impact on their plastic behaviour,” *Prog. Mater. Sci.*, vol. 36, no. C, pp. 1–27, 1992.

[35] V. Vitek and V. Paidar, “Chapter 87 Non-planar Dislocation Cores: A Ubiquitous Phenomenon Affecting Mechanical Properties of Crystalline Materials,” *Dislocations in Solids*, vol. 14. pp. 439–514, 2008.

[36] Y. Zhang, X. Yang, and P. K. Liaw, “Alloy Design and Properties Optimization of High-Entropy Alloys,” *Jom*, vol. 64, no. 7, pp. 830–838, Jul. 2012.

[37] O. N. Senkov, G. B. Wilks, J. M. Scott, and D. B. Miracle, “Mechanical properties of Nb25Mo25Ta25W25 and V20Nb20Mo20Ta20W20 refractory high entropy alloys,” *Intermetallics*, vol. 19, no. 5, pp. 698–706, May 2011.

[38] Q. Sun, Q. Guo, X. Yao, L. Xiao, J. R. Greer, and J. Sun, “Size effects in strength and plasticity of single-crystalline titanium micropillars with prismatic slip orientation,” *Scr. Mater.*, vol. 65, no. 6, pp. 473–476, Sep. 2011.

[39] T. . Mitchell and W. . Spitzig, “Three-stage hardening in tantalum single crystals,” *Acta Metall.*, vol. 13, no. 11, pp. 1169–1179, Nov. 1965.

[40] W. A. Spitzig and A. S. Keh, “Orientation and temperature dependence of slip in iron single crystals,” *Metall. Trans.*, vol. 1, no. 10, p. 2751.

[41] H. Matsui and H. Kimura, “A mechanism of the ‘unexpected {110} slip’ observed in BCC metals deformed at low temperatures,” *Scr. Metall.*, vol. 7, no. 9, pp. 905–913, Sep. 1973.

[42] J.-Y. Kim, D. Jang, and J. R. Greer, “Insight into the deformation behavior of niobium single crystals

under uniaxial compression and tension at the nanoscale," *Scr. Mater.*, vol. 61, no. 3, pp. 300–303, 2009.

[43] A. Seeger, "Why anomalous slip in body-centred cubic metals?," *Mater. Sci. Eng. A*, vol. 319–321, pp. 254–260, Dec. 2001.

[44] a. S. Schneider, C. P. Frick, P. a. Gruber, R. Mönig, O. Kraft, E. Arzt, D. Kaufmann, B. G. Clark, C. P. Frick, P. a. Gruber, R. Mönig, O. Kraft, and E. Arzt, "Correlation between critical temperature and strength of small-scale bcc pillars," *Phys. Rev. Lett.*, vol. 103, no. 10, pp. 1–4, 2009.

[45] Y. Zou, S. Maiti, W. Steurer, and R. Spolenak, "Size-dependent plasticity in an Nb25Mo25Ta 25W25 refractory high-entropy alloy," *Acta Mater.*, vol. 65, pp. 85–97, 2014.

[46] S. Min Han, G. Feng, J. Young Jung, H. Joon Jung, J. R. Groves, W. D. Nix, and Y. Cui, "Critical-temperature/Peierls-stress dependent size effects in body centered cubic nanopillars," *Appl. Phys. Lett.*, vol. 102, no. 4, p. 41910, Jan. 2013.

[47] F. Louchet, "From individual dislocation motion to collective behaviour," *J. Mater. Sci.*, vol. 41, no. 9, pp. 2641–2646, 2006.

[48] C. P. Frick, B. G. Clark, S. Orso, a. S. Schneider, and E. Arzt, "Size effect on strength and strain hardening of small-scale [1 1 1] nickel compression pillars," *Mater. Sci. Eng. A*, vol. 489, no. 1–2, pp. 319–329, 2008.

[49] J. R. Greer, W. C. Oliver, and W. D. Nix, "Size dependence of mechanical properties of gold at the micron scale in the absence of strain gradients," *Acta Mater.*, vol. 53, no. 6, pp. 1821–1830, 2005.

[50] A. T. Jennings, M. J. Burek, and J. R. Greer, "Microstructure versus Size: Mechanical properties of electroplated single crystalline Cu nanopillars," *Phys. Rev. Lett.*, vol. 104, no. 13, 2010.

[51] A. Kunz, S. Pathak, and J. R. Greer, "Size effects in Al nanopillars: Single crystalline vs. bicrystalline," *Acta Mater.*, vol. 59, no. 11, pp. 4416–4424, 2011.

[52] J. M. Wheeler, C. Kirchlechner, J. S. Micha, J. Michler, and D. Kiener, "The effect of size on the strength of FCC metals at elevated temperatures: annealed copper," *Philos. Mag.*, vol. 96, no. 32–34, pp. 3379–3395, 2016.

[53] D. B. Miracle and R. Darolia, "NiAl and its Alloys," *Struct. Appl. Intermet. Compd.*, p. 20, 2000.

[54] J. Y. Kim, D. Jang, and J. R. Greer, "Tensile and compressive behavior of tungsten, molybdenum, tantalum and niobium at the nanoscale," *Acta Mater.*, vol. 58, no. 7, pp. 2355–2363, 2010.

[55] S.-W. Lee and W. D. Nix, "Size dependence of the yield strength of fcc and bcc metallic micropillars with diameters of a few micrometers," *Philos. Mag.*, vol. 92, no. 10, pp. 1238–1260, Apr. 2012.

[56] Y. Zou, S. Maiti, W. Steurer, and R. Spolenak, "Size-dependent plasticity in an Nb25Mo25Ta25W25 refractory high-entropy alloy," *Acta Mater.*, vol. 65, pp. 85–97, Feb. 2014.

[57] J. Weiss, T. Richeton, F. Louchet, F. Chmelik, P. Dobron, D. Entemeyer, M. Lebyodkin, T. Lebedkina, C. Fressengeas, and R. J. Mcdonald, "Evidence for universal intermittent crystal plasticity from acoustic emission and high-resolution extensometry experiments."

[58] M. Zaiser, J. Schwerdtfeger, A. S. Schneider, C. P. Frick, B. G. Clark, P. A. Gruber, and E. Arzt, "Strain bursts in plastically deforming molybdenum micro-and nanopillars," *Philos. Mag.*, vol. 88, pp. 30–32.

[59] T. Zhu, J. Li, A. Samanta, A. Leach, and K. Gall, "Temperature and strain-rate dependence of surface dislocation nucleation," *Phys. Rev. Lett.*, vol. 100, no. 2, 2008.

[60] K. S. Ng and A. H. W. Ngan, "Stochastic nature of plasticity of aluminum micro-pillars," *Acta Mater.*, vol. 56, no. 8, pp. 1712–1720, May 2008.

[61] S. Narayanan, G. Cheng, Z. Zeng, Y. Zhu, and T. Zhu, "Strain Hardening and Size Effect in Five-fold Twinned Ag Nanowires."

[62] S. Buzzi, M. Dietiker, K. Kunze, R. Spolenak, and J. F. Lofler, "Deformation behavior of silver submicrometer-pillars prepared by nanoimprinting," *Philos. Mag.*, vol. 89, no. 10, pp. 869–884, 2009.

[63] T. H. Blewitt, R. R. Coltman, and J. K. Redman, "Low-temperature deformation of copper single crystals," *J. Appl. Phys.*, vol. 28, no. 6, pp. 651–660, 1957.

[64] B. Ramaswami, "Deformation Twinning in Face-Centered Cubic Crystals Effects of Schmid factor and slip nucleation on deformation mechanism in columnar-grained nanotwinned Ag and Deformation Twinning in Face-Centered Cubic Crystals," *J. Appl. Phys. J. Appl. Phys. J. Appl. Phys. Cu J. Appl. Phys. J. Appl. Phys.*, vol. 36, no. 8, pp. 2569–651, 1965.

[65] Y. Deng, C. C. Tasan, K. G. Pradeep, H. Springer, A. Kostka, and D. Raabe, "Design of a twinning-induced plasticity high entropy alloy," *Acta Mater.*, vol. 94, pp. 124–133, 2015.

[66] I. V. Kireeva, Y. I. Chumlyakov, Z. V. Pobedennaya, I. V. Kuksgausen, and I. Karaman, "Orientation dependence of twinning in single crystalline CoCrFeMnNi high-entropy alloy," *Mater. Sci. Eng. A*, vol. 705, no. August, pp. 176–181, 2017.

[67] I. V. Kireeva, Y. I. Chumlyakov, Z. V. Pobedennaya, A. V. Vyrodova, and I. Karaman, "Twinning in [001]-oriented single crystals of CoCrFeMnNi high-entropy alloy at tensile deformation," *Mater. Sci. Eng. A*, vol. 713, no. October 2017, pp. 253–259, 2018.

[68] C. R. Weinberger, B. L. Boyce, and C. C. Battaile, "Slip planes in bcc transition metals," *Int. Mater. Rev.*, vol. 58, no. 5, pp. 296–314, Jun. 2013.

[69] J. Wang, Z. Zeng, C. R. Weinberger, Z. Zhang, T. Zhu, and S. X. Mao, "In situ atomic-scale observation of twinning-dominated deformation in nanoscale body-centred cubic tungsten," *Nat. Mater.*, vol. 14, no. 6, pp. 594–600, Jun. 2015.

[70] M. H. Yoo, "Deformation twinning in superlattice structures," *J. Mater. Res.*, vol. 4, no. 1, pp. 50–54, 1989.

[71] Y. Zhang, X. Yang, and P. K. Liaw, "Alloy Design and Properties Optimization of High-Entropy Alloys." *Jom*, vol. 64, no. 7, pp. 830–838, Jul. 2012.

[72] J. A. Zimmerman, H. Gao, and F. F. Abraham, "Generalized stacking fault energies for embedded atom FCC metals," *Model. Simul. Mater. Sci. Eng.*, vol. 8, no. 2, pp. 103–115, Mar. 2000.

[73] X. W. Zhou, R. A. Johnson, and H. N. G. Wadley, "Misfit-energy-increasing dislocations in vapor-deposited CoFe/NiFe multilayers," *Phys. Rev. B*, vol. 69, no. 14, p. 144113, Apr. 2004.

[74] S. Plimpton, "Fast Parallel Algorithms for Short-Range Molecular Dynamics," *J. Comp. Phys.*, vol. 117, no. 1, pp. 1–19, 1995.

[75] A. Stukowski, "Visualization and analysis of atomistic simulation data with OVITO–the Open Visualization Tool," *Modelling and Simulation in Materials Science and Engineering*, vol. 18, no. 1. p. 15012, 2009.

[76] N. L. Okamoto, S. Fujimoto, Y. Kambara, M. Kawamura, Z. M. T. Chen, H. Matsunoshita, K. Tanaka, H. Inui, and E. P. George, "Size effect, critical resolved shear stress, stacking fault energy, and solid solution strengthening in the CrMnFeCoNi high-entropy alloy," *Sci. Rep.*, vol. 6, no. 1, p. 35863, Dec. 2016.

[77] I. V. Kireeva, Y. I. Chumlyakov, Z. V. Pobedennaya, A. V. Vyrodova, I. V. Kuksgauzen, V. V.

Poklonov, and D. A. Kuksgauzen, “The orientation dependence of critical shear stresses in Al0.3CoCrFeNi high-entropy alloy single crystals,” *Tech. Phys. Lett.*, vol. 43, no. 7, pp. 615–618, Jul. 2017.

[78] J. P. Hirth and J. Lothe, *Theory of Dislocations*, Second Edi. New York: John Wiley & Sons, Inc., 1982.

[79] H. Van Swygenhoven, P. M. Derlet, and A. G. Frøseth, “Stacking fault energies and slip in nanocrystalline metals,” *Nat. Mater.*, vol. 3, no. 6, pp. 399–403, Jun. 2004.

[80] R. J. Asaro and S. Suresh, “Mechanistic models for the activation volume and rate sensitivity in metals with nanocrystalline grains and nano-scale twins,” *Acta Mater.*, vol. 53, no. 12, pp. 3369–3382, Jul. 2005.

[81] T. M. Smith, M. S. Hooshmand, B. D. Esser, F. Otto, D. W. McComb, E. P. George, M. Ghazisaeidi, and M. J. Mills, “Atomic-scale characterization and modeling of 60° dislocations in a high-entropy alloy,” *Acta Mater.*, vol. 110, pp. 352–363, May 2016.

[82] G. Laplanche, A. Kostka, C. Reinhart, J. Hunfeld, G. Eggeler, and E. P. George, “Reasons for the superior mechanical properties of medium-entropy CrCoNi compared to high-entropy CrMnFeCoNi,” *Acta Mater.*, vol. 128, pp. 292–303, Apr. 2017.

[83] T. A. Parthasarathy, S. I. Rao, D. M. Dimiduk, M. D. Uchic, and D. R. Trinkle, “Contribution to size effect of yield strength from the stochastics of dislocation source lengths in finite samples,” *Scr. Mater.*, vol. 56, no. 4, pp. 313–316, Feb. 2007.

[84] S. I. Rao, D. M. Dimiduk, T. A. Parthasarathy, M. D. Uchic, M. Tang, and C. Woodward, “Athermal mechanisms of size-dependent crystal flow gleaned from three-dimensional discrete dislocation simulations,” *Acta Mater.*, vol. 56, no. 13, pp. 3245–3259, Aug. 2008.

[85] I. Toda-Caraballo and P. E. J. Rivera-Díaz-del-Castillo, “Modelling solid solution hardening in high entropy alloys,” *Acta Mater.*, vol. 85, pp. 14–23, Feb. 2015.

[86] C. Varvenne, A. Luque, and W. A. Curtin, “Theory of strengthening in fcc high entropy alloys,” *Acta Mater.*, vol. 118, pp. 164–176, Oct. 2016.

[87] D. Hull and D. J. Bacon, *Introduction to Dislocations*. 2001.

[88] R. Labusch, “A Statistical Theory of Solid Solution Hardening,” *Phys. status solidi*, vol. 41, no. 2, pp. 659–669, 1970.

[89] I. Basu, V. Ocelík, and J. T. M. De Hosson, “Size dependent plasticity and damage response in multiphase body centered cubic high entropy alloys,” *Acta Mater.*, vol. 150, pp. 104–116, May 2018.

[90] A. Giwa, P. K. Liaw, K. A. Dahmen, and J. R. Greer, “Microstructure and Small-scale Size Effects in Plasticity of Individual Phases of Al 0 . 7 CoCrF eN i High Entropy Alloy,” no. 1, pp. 1–21.

[91] O. Torrents Abad, J. M. Wheeler, J. Michler, A. S. Schneider, and E. Arzt, “Temperature-dependent size effects on the strength of Ta and W micropillars,” *Acta Mater.*, vol. 103, pp. 483–494, 2016.

Chapter 5 . Effect of Phase boundary as an interface in small-scale deformation of $Al_{0.7}CoCrFeNi$ HEA

5.1 Introduction

Advanced engineering materials have complex microstructural heterogeneities such as precipitates, multiple phases, embedded intermetallics, inclusions, etc. With these features, bulk metallic systems have interfaces such as grain and phase boundaries. The effect of these interfaces on mechanical properties can now be studied due to the development of small-scale mechanical testing techniques and equipment. In addition to knowing the influences of these interfaces on properties, small-scale metal systems can be designed and modeled based on their responses and functionalities. The focus of this chapter is to understand the effect of phase boundary on different orientation (high and low symmetry) configurations of FCC and BCC phase as bi-phase pillars of the $Al_{0.7}CoCrFeNi$ HEA. The phase boundary acts as a junction where the two crystals meet, but they differ in terms of lattice structure and composition [1]. It has been reported that phase separation occurs in Al-containing HEA due to the rapid un-mixing of the constituents during solidification [2], [3].

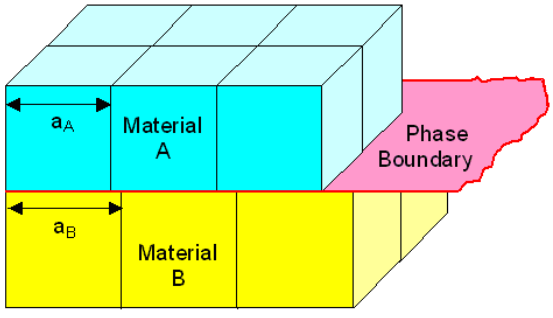

Figure 5.1 Schematic of a phase boundary in a metallic system [4].

Figure 5.1 illustrates the phase boundary showing two different crystal structures having different lattice parameters, which may be of the same or different compositions. We have shown in the XRD study of the HEA in Section 3.4 that the lattice parameter values are 0.3752 nm for the FCC phase and 0.2868 nm for the BCC phase. In [5], it was mentioned that the phase boundaries were high-energy defects like the grain boundaries. In this regard, they can be likened, especially in the context of presence or absence of dislocation densities near the interface, absence or presence of slip transfer from one region to another, distribution of dislocation sources, etc. Kheadmand et al [6] summarized several mechanisms that can occur across grain boundaries which can also be applied to the phase boundary as well; dislocation nucleation drives increase in mechanical properties, especially yield strength and strain hardening as a result of dislocation pile-ups at the boundary; dislocation absorption by dissociation at the interface; dislocation transmission; dislocation absorption and subsequent re-emission. These mechanisms can be observed by both in-situ and ex-situ techniques.

Figure 5.2 (a) shows the lattice arrangement of a bi-phase material having some coincident lattice sites (in red). When subjected to external force either via fabrication (especially in thin layer technology [5]) or through tensile and compressive forces, coherent phase boundaries can be formed, thereby causing multiple lattice matching (Figure 5.2(b)) which aids slip transfer or Figure 5.2 (c) i.e., the introduction of misfit dislocations leading to bending or deflection of the boundary [5]. The difference in the lattice parameter of the combining phases can be an indication for either lattice matching or lattice mismatch. Several other factors play significant roles in the deformation mechanism of the bi-phase material such as crystallographic orientation of the individual phases, the intrinsic

dislocation structure of the combining phases, and most importantly, the surface contribution to stresses of these combining phases during deformation.

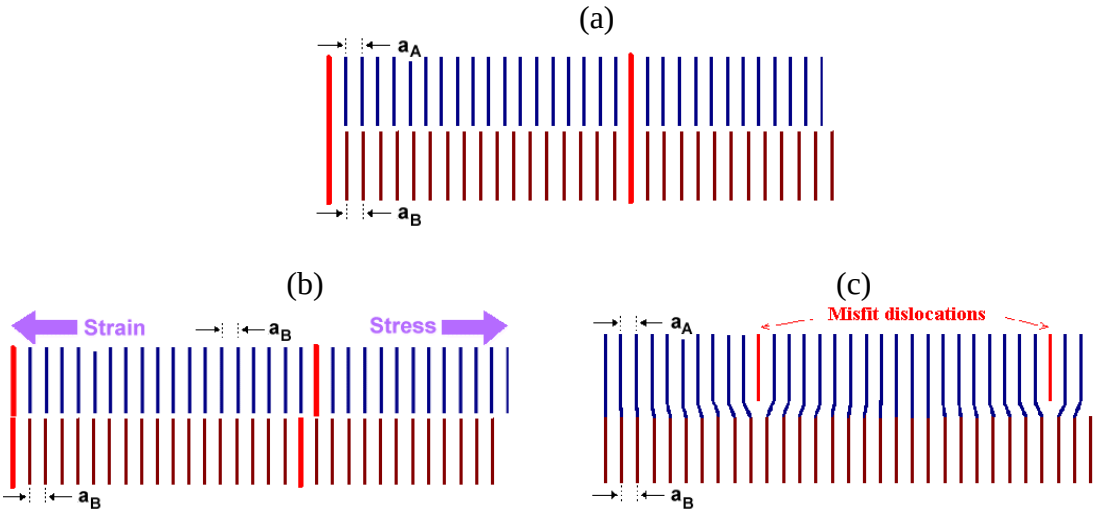

Figure 5.2 (a) Lattice arrangement of a dual phase system and the coincidence site lattice (in red) where the lattice matching takes place. (b) and (c) show the two possibilities of the combining lattice structure when force is applied [5].

Phenomena such as dislocation statistics, dislocation starvation, source truncation, dislocation exhaustion, dislocation nucleation, etc. [7]–[10] have been used to describe nanoscale plasticity which can help understand the effect of the phase boundary at an interface especially at small scales for dislocation–boundary interactions. Several techniques have also been used to investigate dislocation–boundary interactions such as nanoindentation, high resolution EBSD, pillar compression methodology, as well as atomistic simulations [11]. Slip transmission across a boundary is a subject of interest and two models have been suggested to explain this behavior. Zheng et al summarized these models as indirect transmission which occurs as a result of nucleation of Frank-Read sources in the presence of dislocation pile-ups at the boundary [11]–[13], or direct transmission which occurs as a result of dislocation pile-ups transferring to a new slip plane on the other side of the boundary [11], [14], [15]. Imrich et al [7] studied the deformation

of bi-crystalline Cu containing Large Angle Grain Boundary (LAGB) to have improved mechanical properties in strength and strain hardening compared to the individual properties of the combining crystals as a result of the grain boundary acting as an effective barrier to dislocation motion, while bi-crystals having the Coherent Twin Boundary (CTB) have similar properties with the single crystal since the boundary did not act as an impediment to dislocation motion.

In this study, we probe the mechanical properties of bi-phasic FCC/BCC pillars of a high-entropy alloy in different configurations of orientations to understand the effect of orientations of the combining phases, the competing dislocation behavior of the individual phases and, the dislocation-boundary behavior by their mechanical responses.

5.2 Methodology

The EBSD technique as described in Section 3.5 was used to identify the phases and crystal orientation in this study. Vertically aligned bi-phasic 2 μm sized HEA pillars were fabricated from the identified phases and crystallographic orientations of [001] BCC | [101] FCC, [325] BCC | [101] FCC, and [001] BCC | [324] FCC. These configurations were combined as high symmetry BCC | high symmetry FCC, low symmetry BCC | low symmetry FCC, and high symmetry BCC | low symmetries BCC orientations. The lack of a phase boundary in the EBSD mapping for a low symmetry FCC | low symmetry BCC prevented us from probing this configuration.

The pillars were fabricated using Focused Ion Beam (FIB) milling with Ga^+ source. Concentric circular pattern milling was performed until the desired pillar dimensions were achieved. The aspect ratio of 3:1 (i.e. pillar height to diameter) was used in this study. Uniaxial compression experiments were done in the Hysitron described in Section 2.3.1in

displacement control mode at a strain rate of 10^{-3} s^{-1}. The displacement was taken at 15% of the total height. The pillars were compressed using an 8 µm flat punch diamond tip. Figure 5.3(a) shows the electron back-scatter diffraction (EBSD) maps from which the bi-phasic pillars were fabricated. The different types of orientation configurations are illustrated in Figure 5.3(b).

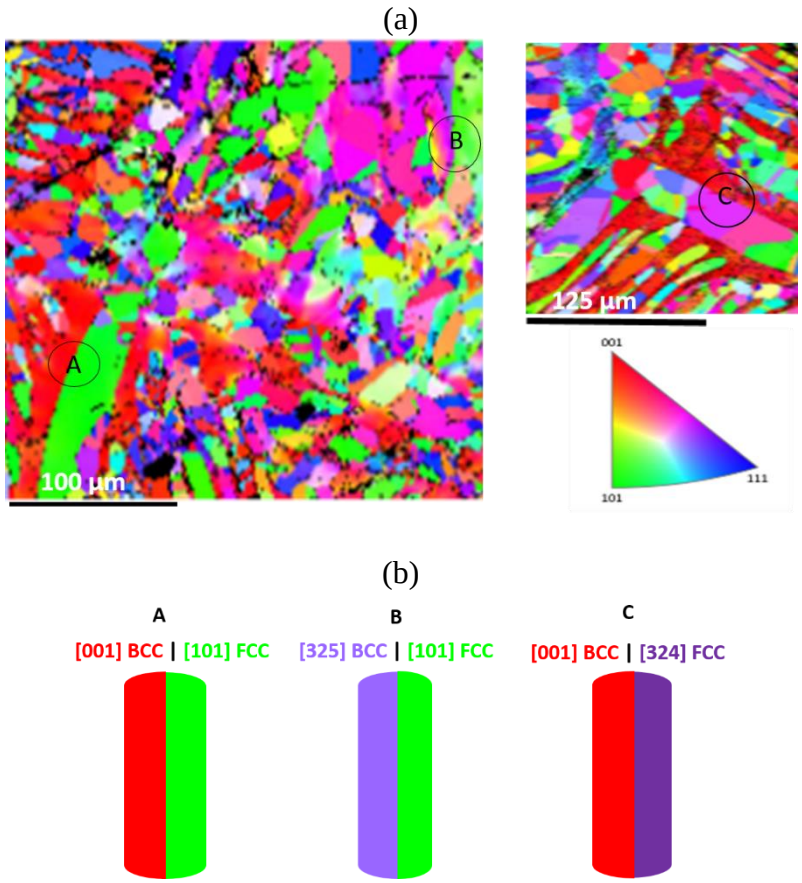

Figure 5.3 (a) Electron BackScatter Diffraction (EBSD) maps from which the bi-phasic pillars were fabricated. (b) Different types of orientation configurations.

5.3 Single Pillar compression experiments

Fundamental differences exist in single crystal plasticity based on their intrinsic material structure, which is related to the differences in their dislocation behavior [16], [17]. Phenomena such as dislocation nucleation in FCC metals and dislocation multiplication in BCC single crystals have been established to explain the varying plastic behavior [16]–[18]. To understand these differences in $Al_{0.7}$CoCrFeNi HEA phases, we fabricated pillars from single crystals of both phases in two orientations of interest: low and high symmetry. These orientations constitute the half-pillars in the study of the effect of an 'interphase' in the bi-phase specimens. The single crystals are [001] BCC, [325] BCC, [101] FCC and [324] FCC. 1 μm and 2μm sized pillars were fabricated from these phases and orientations. These dimensions were chosen due to the dimensions of interest for the bi-phase pillar which is 2 μm. This will enable us compare the size and property relationship of both the single crystals of the FCC and BCC phase with the bi-phase crystals.

5.3.1 Effect of Orientation in FCC phase of $Al_{0.7}$CoCrFeNi HEA

Figure 5.4 (a) represents the typical stress-strain behavior of 1 and 2 μm sized pillars fabricated from the [324] and [101] orientations of the FCC phase. 1 μm sized [101] pillars have a slightly higher yield strength of 0.5 GPa compared to the [324] of the same pillar size which is 0.4 GPa. This difference can be attributed to the difference in the Schmid factor values of both orientations. The Schmid factors for [101] and [324] orientations are 0.408 and 0.638 respectively. This was calculated using the common slip system of {111} [110] generally observed in the FCC system. The Resolved Shear Stresses

(RSS) were calculated as 0.26 GPa for the [324] and 0.20 GPa for the [101]. This shows that the RSS of the [324] is ~ 25% greater than the [101].

(a)

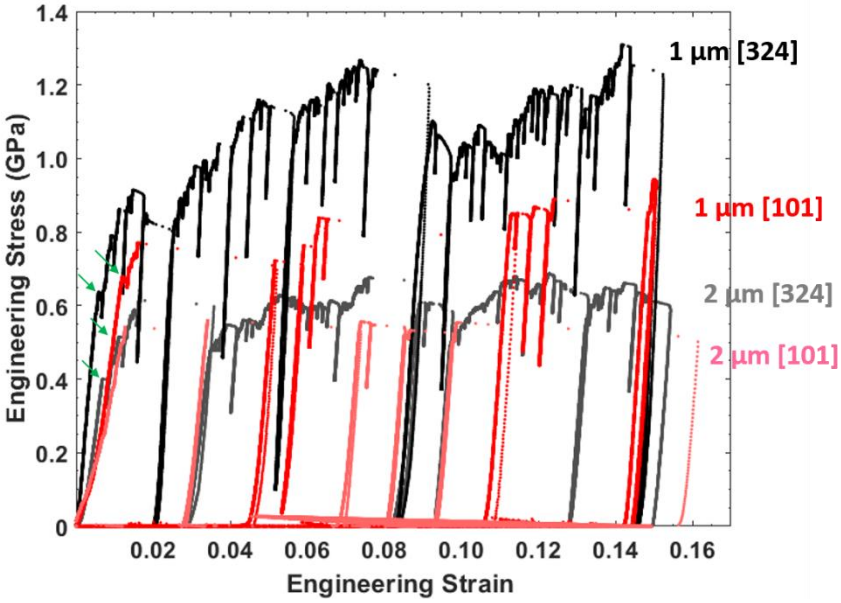

(b)

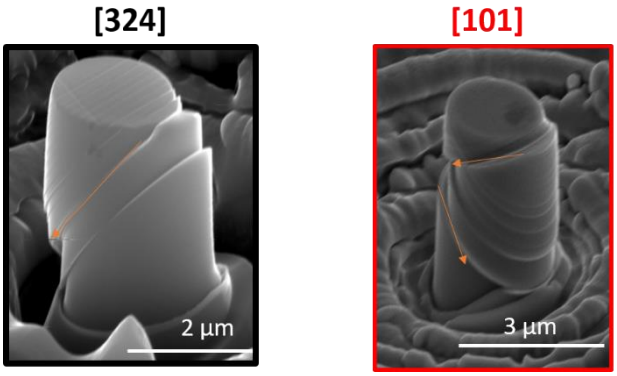

Figure 5.4 (a) Typical stress-strain curves of the [324] FCC pillars – in black and [101] FCC pillars – in red for 1µm and 2 µm sized pillars. The green arrows in the plot indicate the yield points (b) post compressed images of 2 µm sized [324] left and [101] right.

The elastic modulus values were calculated from the intermittent unloading curve at 7 % strain due to uniformity in unloading. The slope from the first one-third of the curve gave values of 214.8 ± 25.5 GPa, which are similar to both [324] and [101]

crystals. The ‘smaller is stronger’ behavior is observed in both orientations as the 1μm pillars have a greater yield strength than the 2 μm pillars. Generally, the ‘smaller is stronger’ phenomenon can be attributed to the distribution, motion, and interactions of dislocations.

Fig. 5.4 (a) shows the typical stress-strain curves of the [324] FCC pillars – in black and [101] FCC pillars – in red for 1μm and 2 μm sized pillars. The green arrows in the plot indicate the yield points and (b) shows the post compressed images of 2 μm sized [324] left and [101] right.

Small sized specimens have fewer dislocations, hence enhancing surface contribution during deformation, as sample sizes are reduced more surface contribution takes place. The strength of the [324] pillars increases as the pillar reduces from 2 μm to 1μm size. A percentage strength increase of 62.5% was calculated for the [324] while for [101], an increase of 40 % was calculated for the same range of sizes. Though the focus of this chapter is not to describe a power law size effect in both orientations, we observed that [101] might have a reduced size dependence when compared with [324] orientation due to a lesser percentage increment in yield stresses of the [101] pillars. [324] has been which was been studied to have a size effect of m = - 0.68 at room temperature for pillar sizes ranging from ~ 400 nm to 2 μm [19] which is universal for commonly studied pure FCC metals [20]–[23]. Zhang et al [24] studied the size effect of single crystal FCC CoCrCuFeNi high symmetry orientation [001] to have m = 0.46, which may suggest a size effect variation with orientation in FCC HEAs.

Discrete stochastic bursts are observed in the stress-strain signatures of both phases. The intermittency of burst events is more in [324] than [101]. Figure 5.4 (b) shows the post

compressed images of the pillars in both phases. There is activation of two slip systems in the post deformed samples of the [101], compared to the 324 which exhibited multiple parallel slips in the one direction. In their study of different Al crystal orientations, Kunz et al [21] indicated that orientations in which the deformation proceeds via double slip system have shorter average burst size, suggesting that multiple slip systems increase hardening by reducing the dislocation mean free path, leading to a shorter average burst size or reduced intermittency as in this case [21].

In addition to the differences in the intermittency of burst events, [324] has high flow stress than the 101. For example, the 1 μm sized [324] samples at 6% strain has a flow stress value of 1.2 GPa, while the [101] of the same size has a flow stress of 0.8 GPa.

The measurement of hardening angles serve as a method for analyzing the degree of hardening in the study of single crystals that undergo discrete stochastic bursts in the stress-strain signature [21]. The angles were measured at strains when contact is fully established during experiments. Angles were measured at 4% strain to 15% strain for the 1μm sized samples of both the [101] and [324] orientations. The hardening angles fall within 8 to 9 degrees which indicates a similarity in hardening behavior. Due to the random distribution of the burst events, it can be suggested that the hardening in both orientations is invariant of orientation.

In FCC single crystals, deformation occurs via annihilation of pre-existing mobile dislocations available at the free surfaces, leaving the pillar in a state of dislocation starvation thereby requiring the nucleation of new dislocations to accommodate plastic deformation [17], [22], [25], [26].

The strengths in small-scale FCC phase of our HEA have higher values than commonly studied FCC metals of the same size. For example, 1 μm size pillars of the [101] and [324] FCC phase of the $Al_{0.7}$CoCrFeNi HEA have yield strengths of ~ 0.65 - 0.70 GPa while Al and Ni have yield strengths of 0.1 GPa and 0.2 GPa, respectively [21], [20]. The strength values increased by a factor of ~3-4 in the HEAs. The high strengths in FCC HEA can be attributed to the solid solution strengthening due to the heterogeneities in the atomic sizes, leading to significant lattice distortion and higher intrinsic lattice resistance [27]. The deformation behavior of the FCC phase in this study can be compared to the deformation of single crystals of pure FCC metals. This comparison can be inferred from the stress-strain signature in Figure 3.6 which shows the elastic loading region, steep post yield strain hardening, and the steady state flow with distinct displacement bursts which are ascribed to the ease of glide dislocation motion in FCC metals.

5.3.2 Effect of Orientation in BCC phase of $Al_{0.7}$CoCrFeNi HEA

Figure 5.5 represents the stress strain behavior of 1 and 2 μm-sized pillars fabricated from [325] and [001] orientations of the BCC phase. The yield strengths of both crystals were determined at 0.2 % offset due to the continuous elastic-plastic transition nature of the stress-strain curve. Pillars fabricated from the [325] BCC crystal have slightly higher stresses than [001] BCC pillars for the same size. Yield strength of 2.0 GPa and 10% flow stress of 3.0 GPa were calculated for 1 μm sized [325] pillar. The [001] pillar of the same size (1μm) had yield strength of 2.0 GPa and a 10% flow stress of 3.0 GPa. The Schmid factors are 0.752 and 0.408 for the [325] and [101], respectively. The resolved shear stresses at yield are 1.50 GPa for [325] and 0.73 GPa for [101] for the same pillar size of 1μm. [325] has an RSS of a factor of 2 greater than [001] which had yield strength

of 2.0 GPa and 10 % flow stress of 3.0 GPa. The elastic modulus was calculated from the slope of first one-third of the unloading curve. Both orientations have similar elastic modulus of ~ 158 GPa.

Using the Holloman relationship in Equation 5.1 to determine the strain hardening exponent *n*

$$\frac{d\ln(\sigma_{10\%}-\sigma_{5\%})}{d\ln(\varepsilon_{10\%}-\varepsilon_{5\%})} = n \qquad (5.1)$$

where $\sigma_{10\%}$is the stress at 10% strain, $\sigma_{5\%}$ is the stress at 5% strain, ε is the strain. *n* values ~ 0.25 to 0.28 was calculated for 2um pillars of [325] and [001] crystals. Figure 5.5 (b) shows the post compressed images of the [325] and the [001] BCC pillars. The [001] pillars exhibits volume expansion in the top region of the pillar with wavy slip traces which are also observed in W pillars [28] and indicate cross-slips in planes with the [111] directions.

(a)

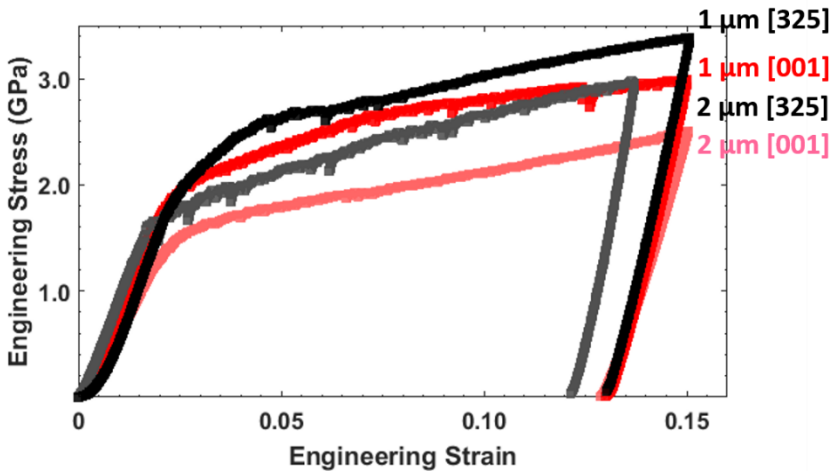

(b)

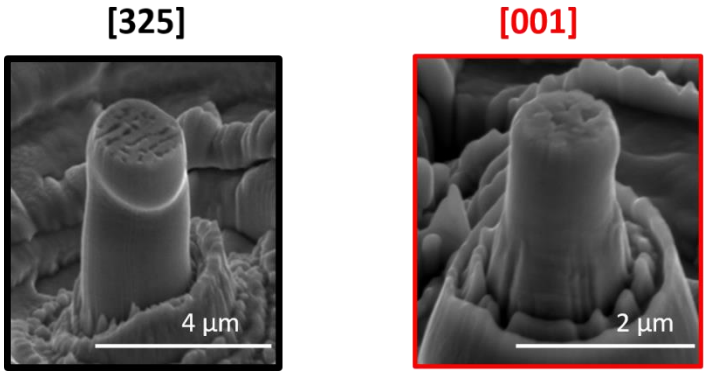

Figure 5.5 (a) shows the typical stress-strain curves of the [325] BCC pillars – in black and [001] BCC pillars – in red (b) shows the post compressed images of 2 µm sized [325] BCC pillar and 1µm sized [001] BCC pillar.

The [325] pillar has distinct slip lines which is similar to [235] deformed Mo pillar [29]. Continuous plasticity is observed in the stress-strain curve of the 2 µm-sized [001] pillar which exhibits intrinsic dislocation core activities during deformation, though a transition exists as the pillar is reduced, suggesting surface contribution by dislocation exhaustion. The presence of burst events in the [325] pillar even for the 2 µm suggests activation of a single slip [29]. This was observed in both 1 µm and 2 µm sized [325] pillars.

In the BCC crystal structure, individual dislocations can form kinks, with the components interacting with one another, thus forming junctions. These interactions lead to greater dislocation densities, sessile junctions, and forest-like hardening upon the application of force [19], [16], [26]. Subsequently, it results in increased stresses in the BCC crystal structure relative to the FCC crystal structure.

Variation exists in the strengths of pure BCC metals due to the differences in their Peierls stresses and specific critical temperatures. For example, Mo with higher Peierls

Stress of 730 MPa [30] have a yield strength of ~ 0.6 GPa [28], while Nb with a Peierls stress of 415 GPa [30] have a yield strength of ~ 0.3 GPa [31] for the same 1μm-sized pillars. Single crystals of $Nb_{25}Mo_{25}Ta_{25}W_{25}$ BCC HEA have been reported to have a yield strength of ~ 2.0 GPa for the same 1μm pillar size.

In this study, the BCC phase of the HEA is hypothesized to have high lattice resistance due to the roughly 60% of Al and Ni with disparate atomic sizes present compared to the other constituent metals [19].

5.3 Deformation response of BCC | FCC Bi – phase pillars

The stress-strain curves of 2 μm bi-phase pillars for the different configurations of orientations studied are shown in Figure 5.6. The configurations [001] BCC | [101] FCC and [325] BCC | [101] FCC represented by the blue and black curves respectively have similar stress-strain response. This would be further defined as A and B bi-phase configurations. The yield stress ranges from about 0.45 to 0.55 GPa. Smooth elastic to plastic transitions are observed due to the presence of stochastic bursts after yield. The yield strengths are found to be similar to the FCC HEA pillars of the same 2 μm size. The plastic deformation in these configurations indicates continuous strain hardening with the presence of burst events. The continuous hardening behavior is typical of the 2 μm sized BCC pillars without the presence of the burst events. Here, we can attribute the burst events to originate from the ease of glide dislocation in the FCC half pillar during the deformation rather than dislocation exhaustion to the free surface in smaller BCC samples. The Elastic modulus calculated for both A and B configurations is 173.8 ± 30 GPa.

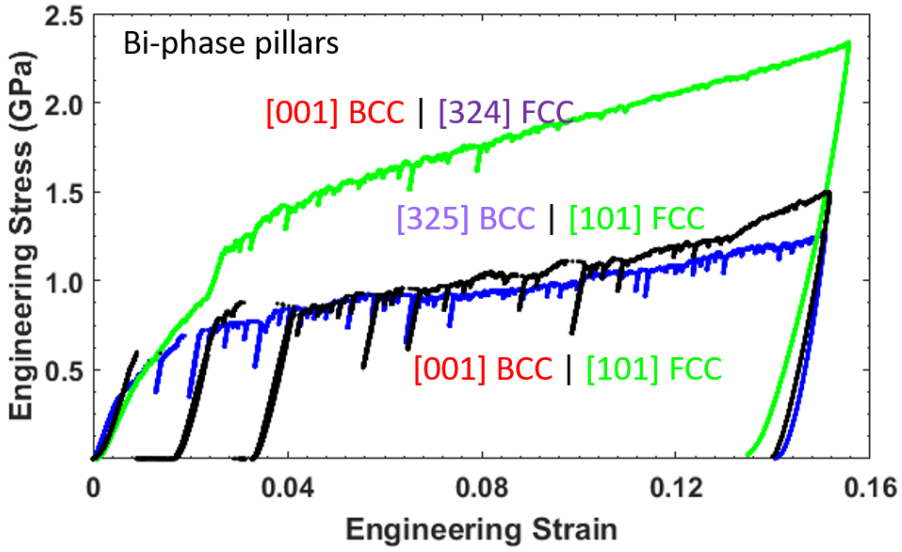

Figure 5.6 shows the stress strain curves for the three bi-phase pillar configurations.

The [001] BCC | [324] FCC bi-phase configuration which would be defined as the C bi-phase configuration has a yield stress of ~1.0 GPa, though lower than 2 µm-sized pillars of BCC [001] and [325] phase of the HEA. The absence of smooth elastic to plastic transition was observed indicating elastic and plastic incompatibility of the crystals of both phases [6]. Continuous plastic deformation is observed at a stress of ~ 1.2 GPa and a strain of 3%. There are fewer burst events in C bi-phase configuration compared to the A and B configurations. The C bi-phase configuration has a higher flow stress than the other configurations, at a strain of 10 %; the C bi-phase configuration has a flow stress of 2.0 GPa, and is a factor of 2 greater than the other configurations. The elastic modulus of the C bi-phase orientation is 210.3 ± 32 GPa; it falls within the range of other configurations.

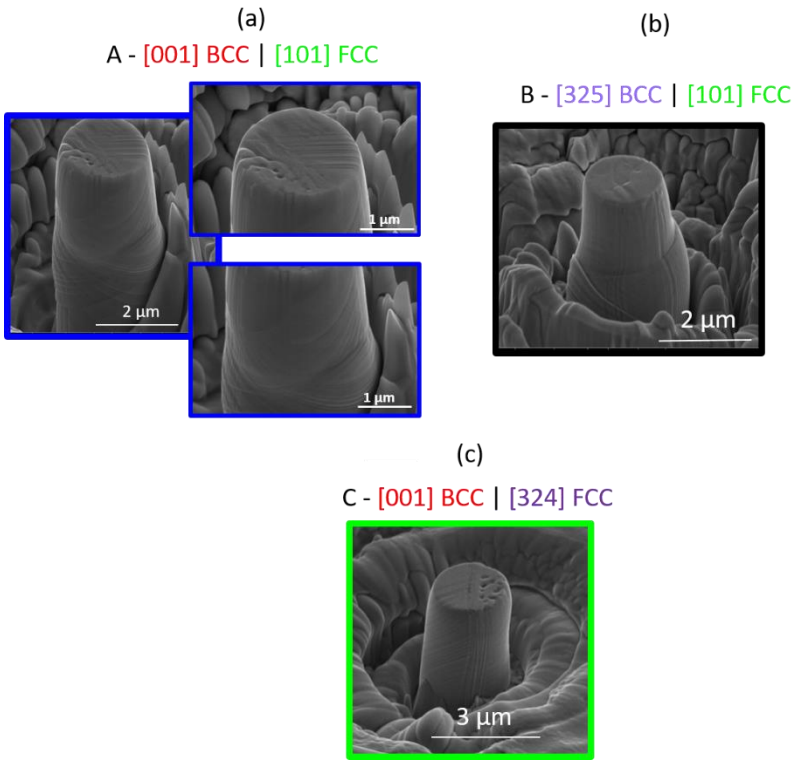

Figure 5.7 Post-compressed images of the three bi-phase pillar configurations.

Figure 5.7 shows the post compressed images of the bi-phase pillars. Figure 5.7(a) shows slip transformation across the FCC and BCC phases of A configuration. We observed multiple slip systems in the [101] orientation from the study of the single crystal [101] FCC. This slip transfer from the FCC phase to the BCC phase indicates that the phase boundary does not serve as an impediment to dislocation motion. It also indicates the homogenous distribution of dislocation sources [6], [21]. Figure 5.4 (b) shows the post compressed image of the B bi-phase configuration. Here, we observe bowing and bending in the pillar as a result of the phase boundary deflection. It can be suggested that inhomogeneous distribution of the dislocation sources [6] and lattice mismatch occur in this configuration. There was no apparent slip transmission from one phase to the other. Figure 5.4 (c) shows the post compressed image of the C bi-phase configuration. Here,

uniform deformation occurs without any change in the phase boundary. Also, no slip transmission occurred, although slip traces were found on the FCC half-pillar. Due to the apparent increase in stress and strain hardening, it can be suggested that dislocation/boundary interaction play a role in this bi-phase deformation.

Figure 5.8 shows the strain-hardening exponent versus the type of bi-phase pillar configuration. The strain hardening exponent (n) calculated for A and B bi-phase configurations using Equation 5.1 from 5% and 10% strains is 0.151 ± 0.06 while the C bi-phase configuration has $n = 0.34 \pm 0.03$. Although there is similarity in the plastic behavior of all the bi-phase configurations due to the continuous hardening and the burst events, the strain hardening exponent value varies particularly for the C configuration due to the higher yield and flow stress.

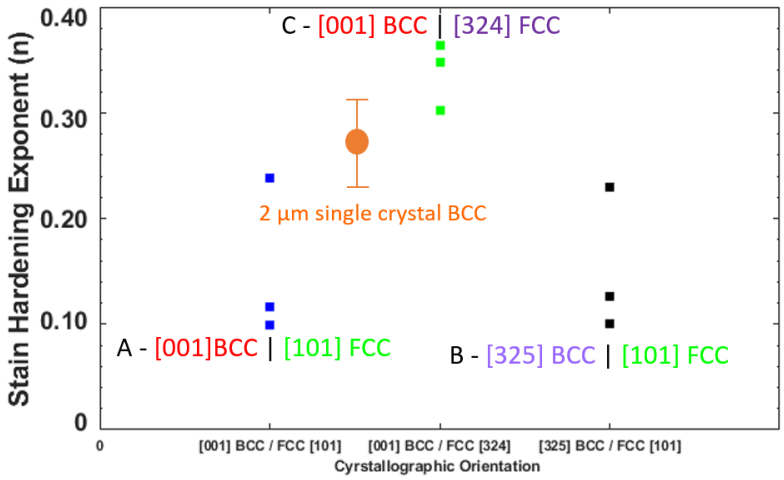

Figure 5.8 shows the strain hardening exponent n *of the bi-phase pillars and* n *of 2 µm [325] and [001] sized BCC pillars.*

5.5 Discussion

We observed different deformation behaviors when comparing the stress-strain data of the single crystals and the bi-phase pillars. The single crystals of the HEA behave

as the typical pure metals of FCC and BCC crystal structure, but with improved mechanical properties due to the solid solution nature of the multi-component alloy. The deformation of bi-phase pillars is indicative of a composite-like behavior of the 2 phases either in elastic and or plastic behavior. For example, the plastic behavior of the 3 bi-phase configurations of the bi-phase pillar have similarities which can be explained based on the intrinsic dislocation structure of the half pillars and velocities of these dislocation motions during plasticity. The competing phenomena in the bi-phase pillars are: (1) the slow mobility of the screw dislocations undergoing cross slips resulting in the formation of kinks and forests to increase the strain hardening for the BCC phase and (2) the easy and fast glide dislocation motion in the FCC phase without apparent increase in continuous strain hardening. The differences in both dislocation velocities for the same amount of strain would have to be investigated via atomistic simulation methods. A combination of these phenomena suggest that continuous plasticity will occur from the BCC half pillar contribution and with the presence of bursts events from the FCC phase simultaneously. This leaves an open question; we seek to understand the energetics of the plastic behavior of the bi-phase, particularly the dislocation velocities of the contributing phases both singly and combined as a bi-phase pillar. This is unrelated to an effect of orientation, but rather the behavior of a dislocation network in the presence of another competing dislocation structure while they simultaneously deform.

The elastic behavior of the three bi-phase configurations can be briefly described as configurations containing the [101] FCC half pillar: A and B configurations undergo a similarity with the single crystal FCC experiments, the yield stress for the same size pillars of 2 μm falls in the range of ~ 0.5 GPa. We know that FCC metals have lower stresses than

the BCC metals. Hence, they have a tendency to yield first in the bi-phase pillars. Due to the activation of multiple slip systems in [101] as seen from Figure 5.1, we suggest a more dominating elastic behavior of the FCC than the FCC in the A and B configurations.

The C bi-phase configuration has a higher yield stress value of ~1.0 GPa and did not have a smooth elastic-to-plastic transition. It is suggested that the presence of just a single slip system in the combining [324] FCC pillar leads to a more elastic activity from the BCC half pillar, thereby causing the uneven transition and a greater stress value. This indicates that the [324] half-pillar does not dominate the elastic deformation of the bi-phase of the [001] BCC | [324] FCC configuration. The influence of an interface such as a phase boundary in small-scale metals is discussed in the context of the role the boundary acts with the presence or absence of dislocations. Grain boundaries have been studied in small-scale crystal deformations to act as either a dislocation source or sink. If the boundary acts as an impedance to dislocation motion, dislocation pile ups are observed at the boundary and mechanical properties such as strain hardening is improved compared to the single crystals [6], [7], [21], [32]. In our experiments, the strain hardening values of the A and B bi-phase configurations are lower than for the BCC single crystals. The presence of discrete bursts in these phases directly suggests that the boundary does not act as a source but rather as a sink [7], [21]. The C bi-phase configuration has higher stresses, but not as high as the BCC single crystals of the same pillar size of 2 μm. Fewer bursts events were present, which indicates that the glide dislocation activity of the FCC half-pillar. The strain-hardening exponent of 0.3 - 0.4 indicates a boundary/dislocation interaction due to the improved plasticity. Therefore, the boundary acted as an effective barrier to dislocation, thus leading to the increased hardening [7].

The slip transmission in the A bi-phase configuration indicates no impedance of the phase boundary to dislocation motion and a smooth deformation of the pillar, and this has been observed in the study of vertically aligned Ni bicrystals. It was inferred that lattice matching and homogeneous distribution of dislocation sources occurred during the deformation of the Ni bicrystals. [6]. Due to the absence of strong boundary/dislocation interactions, the stresses and degree of strain hardening are reduced. This can also be referred to as the absence of dislocation pile-ups at the interface for the promotion of dislocation nucleation [21]. Deflections in bi-crystalline pillars have been studied to occur as a result of inhomogeneous distribution of dislocation sources [6]. This is similar to the deformation behavior in B bi-phase configuration.

5.6 Summary and Outlook

We have studied the influence of phase boundary on small-scale deformation of HEA bi-phase pillars. We observed slip transmission in bi-phase pillars containing high symmetry orientations in both phases while bi-phase pillars containing a mixture of both high and low orientations demonstrate different mechanical responses.

The [001] BCC | [101] FCC bi-phase configuration has lower yield stress values, reduced strain hardening, presence of burst events during plasticity, and evidence of slip transmission across the phases. This behavior suggests that the phase boundary does not serve as an obstacle to dislocation motion, thus preventing dislocation nucleation or pile-ups at the interface. This eventually leads to the ease of slip from the FCC phase to the BCC phase.

The [325] BCC | [101] FCC bi-phase configuration has a similar mechanical response with the configuration, but rather than slip transfer across the phases, we observed

a deflection of the phase boundary which indicates an inhomogeneous distribution of the dislocation sources. Both phases have the [101] FCC half pillars, which suggests that orientation effect cannot be overlooked.

The [001] BCC | [324] FCC configuration exhibited an entirely different mechanical response: the smooth elastic-to-plastic transition was not observed, stresses were high and strain hardening exponent values *n* also improved compared to the *n* values of 2 μm sized BCC pillars of both [325] and [001] orientations. This observation suggests a boundary/dislocation interaction might be responsible for the improved mechanical properties.

In order to understand the interplay between orientation effect, competing dislocation behaviors, presence or absence of dislocations at the boundary and the overall effect of a phase boundary on deformation, molecular dynamics simulations have to be employed to understand the dislocation velocities of the competing dislocation structures, favorable energetics for plastic and elastic deformation, the compatibility of stresses, etc. Also, in-situ mechanical experiments would help shed more light on the competing deformation behaviors. Microstructural analysis of the deformed bi-phase pillars should be conducted using TEM to determine whether dislocations are present at the interface or the influence of boundary thickness on slip activities.

References

[1] "Phase boundaries - an overview | ScienceDirect Topics." [Online]. Available: https://www.sciencedirect.com/topics/chemistry/phase-boundaries. [Accessed: 30-Apr-2018].

[2] W.-R. Wang, W.-L. Wang, S.-C. Wang, Y.-C. Tsai, C.-H. Lai, and J.-W. Yeh, "Effects of Al addition on the microstructure and mechanical property of AlxCoCrFeNi high-entropy alloys," *Intermetallics*, vol. 26, pp. 44–51, 2012.

[3] W. R. Wang, W. L. Wang, and J. W. Yeh, "Phases, microstructure and mechanical properties of AlxCoCrFeNi high-entropy alloys at elevated temperatures," *J. Alloys Compd.*, vol. 589, pp. 143–

152, 2014.

[4] “Phase Boundary - Advanced The critical thickness is very small , even for small misfit,” pp. 1–4.

[5] T. Moritani, “5.3.2 Phase Boundaries,” pp. 1–4.

[6] B. N. Kheradmand and H. Vehoff, “Orientation Gradients at Boundaries in Micron-Sized Bicrystals **,” no. 3, pp. 153–161, 2012.

[7] P. J. Imrich, C. Kirchlechner, C. Motz, and G. Dehm, “Differences in deformation behavior of bicrystalline Cu micropillars containing a twin boundary or a large-angle grain boundary,” *Acta Mater.*, vol. 73, pp. 240–250, 2014.

[8] S. I. Rao, D. M. Dimiduk, M. Tang, M. D. Uchic, T. A. Parthasarathy, and C. Woodward, “Estimating the strength of single-ended dislocation sources in micron-sized single crystals,” *Philos. Mag.*, vol. 87, no. 30, pp. 4777–4794, Oct. 2007.

[9] J. R. Greer and W. D. Nix, “Nanoscale gold pillars strengthened through dislocation starvation,” *Phys. Rev. B - Condens. Matter Mater. Phys.*, vol. 73, no. 24, pp. 1–6, 2006.

[10] T. A. Parthasarathy, S. I. Rao, D. M. Dimiduk, M. D. Uchic, and D. R. Trinkle, “Contribution to size effect of yield strength from the stochastics of dislocation source lengths in finite samples,” *Scr. Mater.*, vol. 56, no. 4, pp. 313–316, Feb. 2007.

[11] Z. Zheng, S. Waheed, D. S. Balint, and F. P. E. Dunne, “Slip transfer across phase boundaries in dual phase titanium alloys and the effect on strain rate sensitivity,” *Int. J. Plast.*, vol. 104, pp. 23–38, May 2018.

[12] T. C. Lee, I. M. Robertson, and H. K. Birnbaum, “Prediction of slip transfer mechanisms across grain boundaries,” *Scr. Metall.*, 1989.

[13] T. C. Lee, I. M. Robertson, and H. K. Birnbaum, “AnIn Situ transmission electron microscope deformation study of the slip transfer mechanisms in metals,” *Metall. Trans. A*, vol. 21, no. 9, pp. 2437–2447, Sep. 1990.

[14] Z. Zheng, D. S. Balint, and F. P. E. Dunne, “Discrete dislocation and crystal plasticity analyses of load shedding in polycrystalline titanium alloys,” 2016.

[15] S. Kondo, T. Mitsuma, N. Shibata, and Y. Ikuhara, “Direct observation of individual dislocation interaction processes with grain boundaries,” 2016.

[16] S. Brinckmann, J. Y. Kim, and J. R. Greer, “Fundamental differences in mechanical behavior between two types of crystals at the nanoscale,” *Phys. Rev. Lett.*, vol. 100, no. APRIL, pp. 1–4, 2008.

[17] J. R. Greer and J. T. M. De Hosson, “Plasticity in small-sized metallic systems: Intrinsic versus extrinsic size effect,” *Prog. Mater. Sci.*, vol. 56, no. 6, pp. 654–724, 2011.

[18] J.-Y. Kim, D. Jang, and J. R. Greer, “Insight into the deformation behavior of niobium single crystals under uniaxial compression and tension at the nanoscale,” *Scr. Mater.*, vol. 61, no. 3, pp. 300–303, 2009.

[19] A. M. Giwa, P. K. Liaw, K. A. Dahmen, and J. R. Greer, “Microstructure and small-scale size effects in plasticity of individual phases of Al0.7CoCrFeNi High Entropy alloy,” *Extrem. Mech. Lett.*, vol. 8, pp. 220–228, 2016.

[20] C. P. Frick, B. G. Clark, S. Orso, a. S. Schneider, and E. Arzt, “Size effect on strength and strain hardening of small-scale [1 1 1] nickel compression pillars,” *Mater. Sci. Eng. A*, vol. 489, no. 1–2, pp. 319–329, 2008.

[21] A. Kunz, S. Pathak, and J. R. Greer, “Size effects in Al nanopillars: Single crystalline vs. bicrystalline,” *Acta Mater.*, vol. 59, no. 11, pp. 4416–4424, 2011.

[22] J. R. Greer, W. C. Oliver, and W. D. Nix, “Size dependence of mechanical properties of gold at the micron scale in the absence of strain gradients,” *Acta Mater.*, vol. 53, no. 6, pp. 1821–1830, 2005.

[23] A. T. Jennings, M. J. Burek, and J. R. Greer, “Microstructure versus Size: Mechanical properties of electroplated single crystalline Cu nanopillars,” *Phys. Rev. Lett.*, vol. 104, no. 13, 2010.

[24] H. Zhang, K. W. Siu, W. Liao, Q. Wang, Y. Yang, and Y. Lu, “In situ mechanical characterization of CoCrCuFeNi high-entropy alloy micro/nano-pillars for their size-dependent mechanical behavior,” *Materials Research Express*, vol. 3, no. 9. 2016.

[25] H. Sanavia and B. Schrefler, *Mechanics of Advanced Materials and Structures*. 2007.

[26] J. R. Greer, C. R. Weinberger, and W. Cai, “Comparing the strength of f.c.c. and b.c.c. sub-micrometer pillars: Compression experiments and dislocation dynamics simulations,” *Mater. Sci. Eng. A*, vol. 493, no. 1–2, pp. 21–25, 2008.

[27] Y. Zhang, T. T. Zuo, Z. Tang, M. C. Gao, K. A. Dahmen, P. K. Liaw, and Z. P. Lu, “Microstructures and properties of high-entropy alloys,” *Prog. Mater. Sci.*, vol. 61, no. October 2013, pp. 1–93, Apr. 2014.

[28] J. Y. Kim, D. Jang, and J. R. Greer, “Tensile and compressive behavior of tungsten, molybdenum, tantalum and niobium at the nanoscale,” *Acta Mater.*, vol. 58, no. 7, pp. 2355–2363, 2010.

[29] A. S. Schneider, B. G. Clark, C. P. Frick, P. A. Gruber, and E. Arzt, “Effect of orientation and loading rate on compression behavior of small-scale Mo pillars,” *Mater. Sci. Eng. A*, vol. 508, no. 1–2, pp. 241–246, 2009.

[30] T. Suzuki, H. Koizumi, and H. O. K. Kirchner, “Plastic flow stress of b.c.c. transition metals and the Peierls potential,” *Acta Metall. Mater.*, vol. 43, no. 6, pp. 2177–2187, Jun. 1995.

[31] a. S. Schneider, C. P. Frick, B. G. Clark, P. a. Gruber, and E. Arzt, “Influence of orientation on the size effect in bcc pillars with different critical temperatures,” *Mater. Sci. Eng. A*, vol. 528, no. 3, pp. 1540–1547, 2011.

[32] N. Kheradmand, A. F. Knorr, M. Marx, and Y. Deng, “Microscopic incompatibility controlling plastic deformation of bicrystals,” *Acta Mater.*, vol. 106, pp. 219–228, 2016.

Chapter 6 . Damping capacity of the individual phases of $Al_{0.7}$CoCrFeNi HEA

6.1 Motivation

The damping capacity of metals and alloys can be studied from the perturbation of atom motions via oscillatory deformation. Damping capacity is a measure of a material's ability to dissipate elastic strain energy during mechanical vibration or wave propagation [1]. This can be frequency, temperature, or combined (frequency/temperature) controlled. It is important to characterize the damping properties of alloys having good mechanical properties since they are potential materials for structural applications. HEAs as a novel class of materials possess high mechanical properties and thermal stability especially refractory compositions [2], [3]. It is important to establish the kinetic stability of this system having complex atomic arrangements. Materials with high mechanical properties have low damping properties [1] and there is a need to fabricate materials with excellent mechanical properties and high damping capacities to prevent unwanted noise and vibrations during use. Alloys such as Mn-Cu, Fe-Cr-Al, and Zn-Al have been observed to have high damping capacities and have found applications in marine and automotive industries [4].

The damping behavior of bulk Al(x)CoCrFeNi (where x = 0 - 2) was studied by Ma et al [5] who observed storage modulus (E') of (~ 67 – 88 GPa) depending on the Al content for a range of frequency 1 to 16 Hz. It was observed that E' is independent of frequency at a particular temperature. This phenomenon was related to composite strengthening in polymeric concrete composites [6]. Small-scale $Al_{0.7}$CoCrFeNi HEA has shown improved mechanical properties than its bulk counterparts due to the surface

contribution via dislocation starvation and subsequent nucleation in the FCC phase and dislocation multiplication and exhaustion to the free surface in BCC phase [7]–[9]. There is a need to establish the damping properties of nano-sized HEAs to enable us to predict the effect of vibration if applied in the fabrication of micro and nano electromechanical devices (MEMS/NEMS) devices.

Dual-phase $Al_{0.7}CoCrFeNi$ HEA is an ideal candidate to compare the dynamic properties of the individual phases since commonly studied HEAs are either BCC or FCC crystal structure. We discuss the results in relation to differences in intrinsic properties of the individual phases and compare the results to the damping behavior of bulk HEA of similar composition.

6.2 Materials and Methods

Bulk $Al_{0.7}CoCrFeNi$ was fabricated via vacuum arc melting as described in Section 2.2. The phase information and orientation mapping were obtained using Electron Back-Scatter Diffraction (EBSD) technique described in Section 2.2. 500 nm-sized pillars were fabricated from [324] FCC and [001] BCC phases of the HEA. This was done using the Focused Ion Beam (FIB) milling fabrication by making concentric circular milling until pillar dimensions reached the aspect ratio of 3:1, i.e. height to diameter was achieved. The quasi-static and dynamic experiments were performed using the Hysitron triboindenter with an 8 μm diamond flat-punch tip. The quasi-static experiments were done in displacement-controlled mode at a strain rate of $10^{-3}s^{-1}$ to a final total strain of 15% of the pillar height. The dynamic experiments were performed in the force-controlled mode at prescribed force oscillations of 50 μN. The experiments were conducted at room temperature at frequencies ranging from 5 to 20 Hz.

Dynamic mechanical properties such as complex modulus, storage modulus, loss modulus, and loss tangent were calculated from these experiments. The complex modulus measures the stiffness of a material. The storage and loss moduli represent the stored elastic energy and the energy dissipated as heat respectively, while the loss tangent represents the damping capacity or factor.

The complex modulus E^* is represented as $E^* = E' + iE''$ (6.1)

where E' is the storage modulus and E'' is the loss modulus.

The storage modulus is represented as $E' = \frac{\sigma_0}{\varepsilon_0}\cos\delta$ (6.2)

The loss modulus is represented $E'' = \frac{\sigma_0}{\varepsilon_0}\sin\delta$ (6.3)

where σ_0 is the stress amplitude and ε_0 is the strain amplitude and δ is the phase shift illustrated by the plot [10] below.

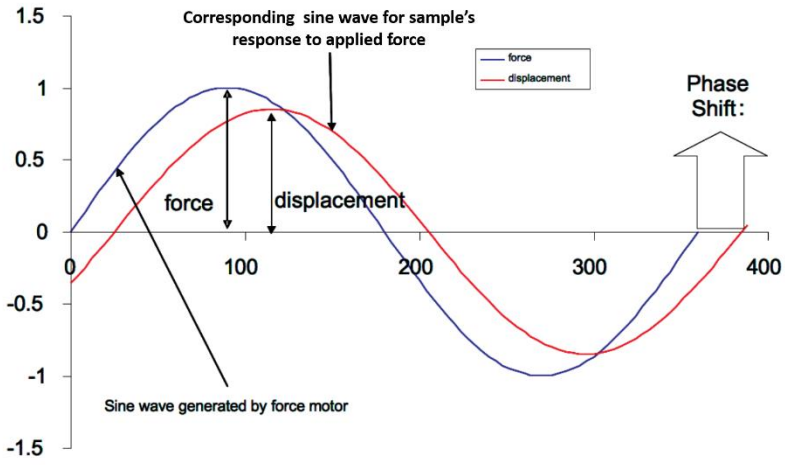

Figure 6.1: Sinusoidal plot relating the force/displacement amplitude and phase shift [10].

The loss tangent is represented as $\tan\delta = E''/E'$ (6.4)

6.3 Quasi-Static Experiments

6.3.1 FCC Phase

Figure 6.2 shows the mechanical response of 500 nm-sized [324] FCC nanopillars. Figure 6.2 (a) gives the load-displacement curve. The experiment was carried out in displacement control mode at a strain rate of 10^{-3} s^{-1} to a total strain of 15% of the pillar height. The maximum load measured during elastic regime is 213.40 μN. This maximum load was reached at 13.52 seconds at a depth of 18.6 nm of the nanopillars. It is essential to determine the maximum load the nanopillar can withstand in the elastic regime since the experiments were conducted in force control mode. For the dynamic experiments, we subjected the FCC pillar to a quasi-static load of 120 μN prior to the dynamic loading of 50 μN, indicating that our sample was still at the elastic regime before dynamic force was applied. Figure 6.2 (b) shows the post-compressed nanopillar having multiple parallel slip lines as shown previously (Chapters 3-5) for [324] compressed FCC nanopillars.

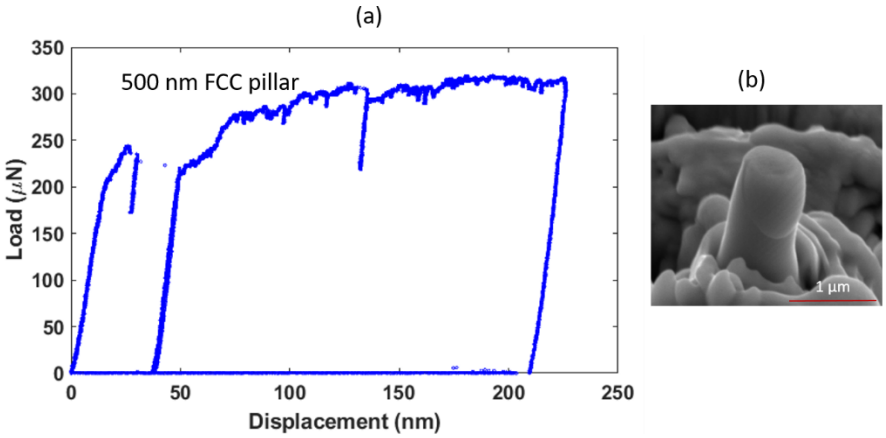

Figure 6.2: (a) Load versus displacement plot of the 500 nm sized [324] nanopillars of the FCC phase of the $Al_{0.7}$CoCrFeNi HEA and (b) the post-compressed pillars showing the slip lines.

6.3.2 BCC phase

Figure 6.3 shows the mechanical response of 500 nm sized [001] BCC nanopillars. Figure 6.3 (a) gives the load-displacement curve. The experiment was performed in displacement-control mode at a strain rate of 10^{-3} s^{-1} to a total strain of 15% of the pillar height. The maximum load measured during the elastic regime is 360.30 μN. This maximum load was reached at 30.47 seconds at a depth of 44.13 nm of the nanopillar. For the dynamic experiments, we subjected the FCC pillar to a quasi-static load of 250 μN prior to the dynamic loading of 50 μN. This indicated that our sample was still in the elastic regime before dynamic force was applied. Figure 6.2 (b) shows the post compressed nanopillar having wavy slip line as shown in previous chapters (3-5) for [001] compressed BCC nanopillars.

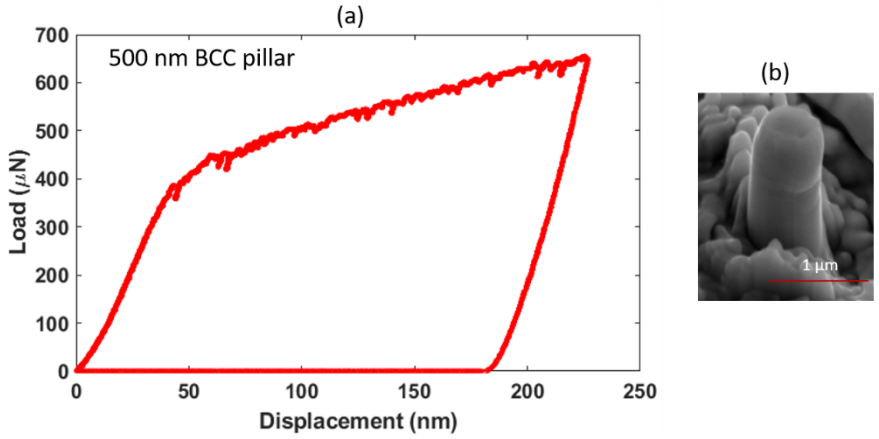

Figure 6.3: (a) The load versus displacement plot of the 500 nm sized [001] nanopillars of the BCC phase of the $Al_{0.7}$CoCrFeNi HEA (b) the post-compressed pillars showing the wavy slip line.

6.4 Dynamic mechanical response

To understand the damping capacity of FCC and BCC nanopillars of $Al_{0.7}CoCrFeNi$ HEA, frequency sweep (5 – 20 Hz) experiments were conducted on 500 nm-sized pillars fabricated from [324] FCC phase and [001] BCC phase. The experiments were conducted at room temperature. Sinusoidal stress of 50 μN was applied to the FCC and BCC nanopillar after quasi-static loading of 120 μN and 250 μN respectively.

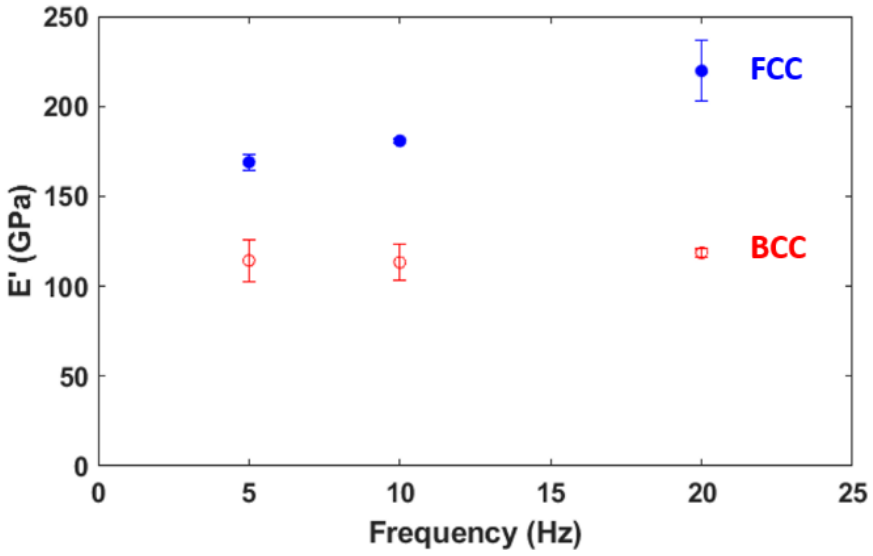

Figure 6.4 Storage modulus (E') calculated for 500 nm FCC nanopillars (in blue) and 500 nm sized BCC nanopillars (in red).

Using Equation 6.2, we calculated the storage modulus based on the phase shift (δ) and the load amplitude converted to stress amplitude and the displacement amplitude converted to the strain amplitude. From Figure 6.4, we observed that $E'$of FCC nanopillars increase from 160 GPa to 220 GPa as the frequency increases from 5 Hz to 20 Hz. The E' of the BCC nanopillars have a constant value of ~ 113 GPa at all frequencies studied. These

point to the ability of the FCC nanopillars to store more deformation energy in an elastic manner.

Additionally, we calculated the loss tangent ($\tan\delta$), i.e. the mechanical damping or damping factor of both FCC and BCC 500 nm sized nanopillars using Equation 6.4. From Figure 6.5, we observe that $\tan\delta$ of FCC nanopillars are in the range of (1 - 1.8 x 10^{-2}), while $\tan\delta$ of the BCC nanopillars ranges from (3 - 4 x 10^{-3}). This indicates that the damping capacity of the FCC nanopillar is higher than that of the BCC nanopillars.

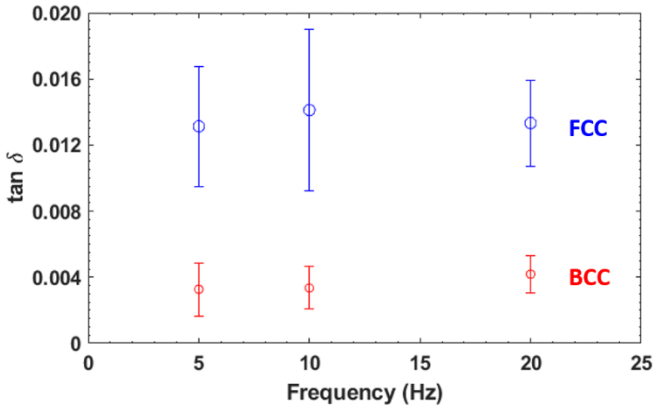

Figure 6.5 Plot of tan δ calculated for 500 nm sized FCC nanopillars (in blue) and 500 nm sized BCC nanopillars (in red).

Figure 6.6 shows the typical pre and post compressed images of [324] 500 nm-sized FCC nanopillars and [001] 500 nm sized BCC nanopillars. The post-compressed images (Figures 6.6 (b, d) showed that the dynamic mechanical experiments did not subject the nanopillars to permanent deformation as shown in Figure 6.2 (b) and 6.3 (b) for the quasi-static experiments up to 15% strain for FCC and BCC nanopillars respectively. These post – compression images indicate that the experiments were done prior to plastic deformation.

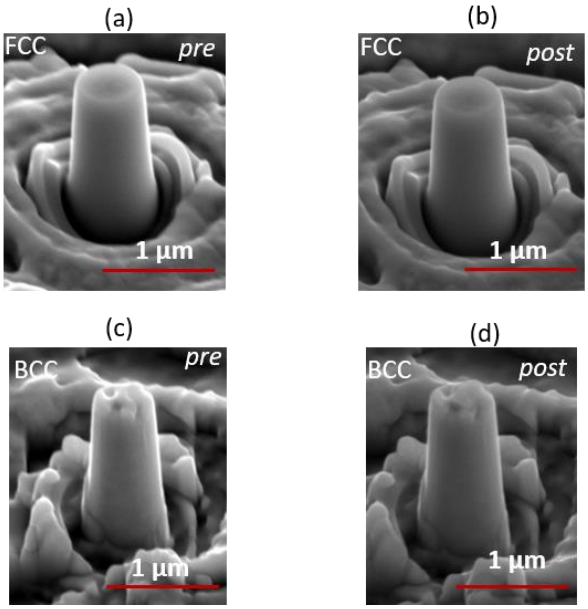

Figure 6.6: (a) [324] 500 nm-sized FCC nanopillar pre – dynamic experiment image (b) [324] 500 nm-sized FCC nanopillar post – dynamic experiment image(c) [001] 500 nm-sized BCC nanopillar pre – dynamic experiment image (d) [001] 500 nm-sized BCC nanopillar post-dynamic experiment image.

6.5. Discussion

Figure 6.5 shows the storage modulus E' vs frequency of 500 nm-sized FCC and BCC nanopillars fabricated from the [324] and [001] crystals of both phases respectively. The high E' values of the FCC nanopillars are related to the closely packed atomic structure of this crystal system. Materials with high level of cross linking (especially polymers) are known to have high storage modulus values. Apart from the closed atom packing in FCC phase, the BCC phase has more lattice resistance based on the elemental analysis (60 % Al and Ni compared to other constituent metals) of this phase, this prevents the atomic motion at the applied sinusoidal stress of 50 µN [7], [11]–[13]. It has been reported that a higher Al content in HEAs generally reduces the storage Modulus [5] due to enhanced interatomic-binding strength of Al and Transition Metals (TMs). This suggests that atomic motion is more restricted in the BCC phase of the HEA, which reduces the storage energy during elastic deformation. The FCC nanopillars exhibit increasing $E'$with increasing

frequency, while the BCC nanopillars give a constant E' at all the frequencies studied. This indicates that the BCC nanopillar is more kinetically stable than the FCC nanopillar. It can be inferred that FCC is very sensitive to external influences such as strain rate, temperature, frequency, etc. Higher mobility of the atoms and unpinning of the dislocation points can be more induced at higher frequencies.

Ma et al [5] studied the damping properties of bulk AlxCoCrFeNi (x = 0 – 1) at room temperature. Storage Modulus E' of 67 - 88 GPa was reported with x = 1 which is an entire BCC system having the least value of E'= 65 GPa, while the x = 0, which is an entire FCC alloy, has E' = 88 GPa, 500 nm-sized BCC pillars has $E'$of ~113 GPA which is double that of an AlCoCrFeNi BCC HEA. The FCC pillars have E' ranging from 160 - 220 GPa, which is also greater than bulk FCC HEAs ($Al_xCoCrFeNi$ where x = 0, 0.25 and 0.50) by a factor of ~ 2. Due to the larger surface area in small sized materials, surface atoms tend to vibrate more than the internal atoms, thereby increasing the atoms that vibrate more in the overall sample.

The tan δ of BCC nanopillars ranges from ($3 – 4 \times 10^{-3}$), while tan δ of the FCC nanopillars ranges from ($1.0 - 1.8 \times 10^{-2}$). The damping factor is higher in FCC than in BCC nanopillars. It is suggested that structural defects such as stacking faults can lead to ease of atom motion in the FCC nanopillars, unlike in BCC pillars.

The FCC nanopillars have a greater damping factor tan δ than bulk FCC HEAs ($Al_xCoCrFeNi$, x = 0, 0.25, 0.5), which ranges from ($3 – 7 \times 10^{-3}$). Tan δ of Bulk BCC HEA (AlCoCrFeNi) ranges from ($1 – 2 \times 10^{-3}$). The observed differences in the damping properties of the bulk FCC / BCC HEAs and FCC / BCC nanopillars of Al0.7CoCrFeNi

stem from surface effect during oscillatory deformation as external atoms undergo more vibrations than internal ones. This increases the overall damping properties of nanopillars.

6.6 Summary and Outlook

The preliminary study of the damping capacity on 500 nm-sized pillars of single crystal [324] FCC and [001] BCC of $Al_{0.7}$CoCrFeNi HEA was probed via oscillatory deformation in the low frequency range of 5 to 20 Hz at room temperature. We observed a frequency dependent storage modulus (E') of 160 - 220 GPa for the FCC pillars and frequency independent storage modulus (E') of 113 GPa for the BCC pillars. We attribute these differences to the intrinsic atomic structure of both phases. The FCC phase has more close atom packing than the BCC phase, which will allow ease of atom motion. The BCC phase has been previously described to have high interatomic bond strength due high Al content compared to the combining element, the higher atomic size of Aluminum and the high interatomic bond strength due to the covalent bonding of Al-TMs. This shows that the FCC has more capacity to store elastic energy than the BCC phase. The frequency dependence nature of the FCC nanopillar on the storage modulus (E') suggests that it is more sensitive to external factors like strain rate, etc.

The damping capacity (tan δ) for the FCC nanopillars is higher than the BCC. It is suggested that structural defects such as stacking faults and ease of unpinning of dislocations and atoms motions contributes to the high tan δ of this phase. Overall, we observed higher damping properties in the nano-sized HEAs when compared to bulk HEAs of similar composition. This suggests that in small-sized specimen, external atoms have more vibrations due to high surface to volume ratio compared to bulk samples.

More work needs to be done to establish the structural relaxation phenomena that may occur in single crystals of HEAs across a wider range of frequencies and also at different temperatures. Damping factor peaks which are usually obtained in plots of tan δ versus frequency/temperature can be pointers to dislocation relaxation, vacancy relaxation, solid solution peaks, etc. Additionally, it will be important to study the effect of material size on damping properties using several postulated models such as surface elasticity model and surface stress model for small-sized mechanical devices. Alloy composition can also be varied to include high damping metals such as Mg.

References

[1] J. Zhang, R. J. Perez, and E. J. Lavernia, "Documentation of damping capacity of metallic, ceramic and metal-matrix composite materials," *J. Mater. Sci.*, vol. 28, pp. 2395–2404, 1993.

[2] O. N. Senkov, C. Woodward, and D. B. Miracle, "Microstructure and Properties of Aluminum-Containing Refractory High-Entropy Alloys," *Jom*, vol. 66, no. 10, pp. 2030–2042, 2014.

[3] O. N. Senkov, J. M. Scott, S. V. Senkova, F. Meisenkothen, D. B. Miracle, and C. F. Woodward, "Microstructure and elevated temperature properties of a refractory TaNbHfZrTi alloy," *J. Mater. Sci.*, vol. 47, no. 9, pp. 4062–4074, 2012.

[4] I. G. Ritchie and Z.-L. Pan, "High-damping metals and alloys," *Metall. Trans. A*, vol. 22, no. 3, pp. 607–616, Mar. 1991.

[5] S. G. Ma, P. K. Liaw, M. C. Gao, J. W. Qiao, Z. H. Wang, and Y. Zhang, "Damping behavior of Al x CoCrFeNi high-entropy alloys by a dynamic mechanical analyzer," vol. 604, pp. 331–339, 2014.

[6] F. Cortés and M. Jesú S Elejabarrieta, "Modelling viscoelastic materials whose storage modulus is constant with frequency," 2006.

[7] A. M. Giwa, P. K. Liaw, K. A. Dahmen, and J. R. Greer, "Microstructure and small-scale size effects in plasticity of individual phases of Al0.7CoCrFeNi High Entropy alloy," *Extrem. Mech. Lett.*, vol. 8, pp. 220–228, 2016.

[8] J. R. Greer and J. T. M. De Hosson, "Plasticity in small-sized metallic systems: Intrinsic versus extrinsic size effect," *Prog. Mater. Sci.*, vol. 56, no. 6, pp. 654–724, 2011.

[9] S. Brinckmann, J. Y. Kim, and J. R. Greer, "Fundamental differences in mechanical behavior between two types of crystals at the nanoscale," *Phys. Rev. Lett.*, vol. 100, no. APRIL, pp. 1–4, 2008.

[10] PerkinElmer and Inc, "Dynamic Mechanical Analysis (DMA) A Beginner's Guide."

[11] S. Guo and C. T. Liu, "Phase stability in high entropy alloys : Formation of solid-solution phase or amorphous phase," *Prog. Nat. Sci. Mater. Int.*, vol. 21, no. 6, pp. 433–446, 2011.

[12] Y. Zhang, X. Yang, and P. K. Liaw, "Alloy Design and Properties Optimization of High-Entropy Alloys." *Jom*, vol. 64, no. 7, pp. 830–838, Jul. 2012.

[13] W.-R. Wang, W.-L. Wang, S.-C. Wang, Y.-C. Tsai, C.-H. Lai, and J.-W. Yeh, “Effects of Al addition on the microstructure and mechanical property of AlxCoCrFeNi high-entropy alloys,” *Intermetallics*, vol. 26, pp. 44–51, 2012.

Chapter 7 . Conclusions and Outlook

This work explored microstructure to mechanical properties of a novel metal system – High Entropy Alloys. We observed improved nanomechanical properties from the individual phases (FCC and BCC) of the $Al_{0.7}$CoCrFeNi compared to pure FCC and BCC metals, and this is due to the solid solution nature of the HEA, the surface contribution because of the small-sized specimen and the increased lattice resistance as a result of the elemental heterogeneity in the metal system. The calculated stresses scale with the pillar sizes in a power law relation $\sigma_y \propto D^{-m}$. The exponent *n* of the [324] FCC pillars shows the universal exponent of *m* = - 0.68 which is similar to commonly studied pure FCC metals. The size effect '*m'* reduces with decreasing temperature; we calculated *n* as - 0.38 at 40 K. The microstructural analysis of the deformed [324] FCC pillars suggests a dislocation-mediated mechanism at 293 K, 143 K and 40 K. For [001] BCC pillars, higher strengths were also observed in comparison to the FCC phase due to the cross slip behavior of the dislocation structure in this phase, and more complex elemental distribution which further increases the lattice resistance. Size effect exponent *n* of the BCC phase at all temperatures studied was - 0.33, and this suggests no change in the intrinsic dislocation structure with reducing temperature. The microstructural analysis of the deformed [001] BCC pillar reveals an additional twinning deformation.

The effect of phase boundary was studied via uniaxial compression of bi-phase pillars of different orientations. Slip transmission was observed across the 'interphase' in orientation configurations of both high symmetry BCC and FCC, suggesting no impedance to dislocation motion and homogeneous distribution of the dislocations sources, while bi-phase configuration of mixed low and high symmetries of both phases gave different

mechanical responses. These findings suggest the interplay of orientation effects and competing dislocation behavior of the combining phases as they deform simultaneously.

Preliminary dynamic experiments were carried out on 500 nm pillars of both phases at room temperature at a low frequency range of 5 to 20 Hz. FCC has a higher damping factor (tan δ) of (1.0 - 1.8 x 10^{-2}) while tan δ of BCC pillars ranges from (3.0 – 4.0 x 10^{-3}). Additionally, the storage modulus (E') in FCC pillars increases from 160 - 220 GPa as frequency increases from 5 to 20 Hz, while BCC pillars of the same size of 500 nm have a constant E' of ~113 GPa at the same frequency range. It is interesting to note that E' is higher in these pillars by a factor of 2 than previously studied Bulk FCC and BCC HEAs.

Most small-scale mechanical properties of HEAs have been studied via uniaxial compression experiments, but several other experiments need to be conducted, and this would involve exploring other fabrication routes apart from micromachining using Focused Ion Beam milling (FIB). Techniques such as co-sputtering, Ion-Beam Assisted deposition, electrodeposition, additive manufacturing, 2-photon lithography can be explored for appropriate geometries for tensile, fracture, fatigue experiments, etc. Limitations occur in probing small-scale mechanical properties of HEAs due to difficulty in the fabrication HEAs.

Additionally, crystal plastic theory of HEAs needs to be developed using atomistic and continuum approaches which incorporates the multi-principal nature of the alloy, solid solution effect, high distortion, and lattice resistance, etc. Phenomenon suggesting fundamental differences between HEAs and pure metals can be also explored. For example, significant Peierls stress in FCC HEAs.

Appendix A. Solid solution strengthening mechanism calculations.

According to [1], we can represent the line tension of a dislocation cutting through an array of particles as:

$$\tau_{max} = F_{max}/bL' \qquad \text{(A.1)}$$

where F_{max} is the force required to tear a dislocation from the solute atom, b is the Burgers vector, and L' is the spacing between precipitates on a slip plane. L' can be measured as $b/(2c)^{1/2}$ [1] where c is the concentration of the solute atoms which is Aluminum. From the EDX data obtained, the relative atomic concentration of Al is ~ 0.303. Hence,

$$\tau_{max} = G\ x\ (2c)^{1/2} \qquad \text{(A.2)}$$

where the shear modulus G = 70 GPa [2] and the Burgers vector b can be approximated as $(a\sqrt{3})/2$: $a = 0.2868\ nm$ [3]. The volume of Al in a unit cell is 0.303 x (0.2868 nm)^3 = 7.15 x 10^{-30} m^3. The volume of a typical cylindrical pillar with a 400 nm-diameter pillar can be estimated as $\pi r^2 h = 1.51 \times 10^{-19}\ m^3$, where h is the pillar height (1.2 μm) and r is its radius. The volume concentration fraction of Al, then can be calculated as (7.15 x 10^{-30} / 1.51 x 10^{-19}) = 4.74 X10^{-11}, which enables us to calculate the maximum shear stress required to pass a dislocation through an array of Al obstacles as:

$$\tau_{max} = G\ x\ (2c)^{1/2} = 70\ \text{GPa x}\ (2 \times 4.74 \times 10^{-11})^{1/2} = 0.68\ \text{MPa}$$

The Resolved Shear Stress (τ) from the highest yield strength of 2.2 GPa, obtained experimentally during a typical compression of a 400 nm-diameter pillar, is:

$$\tau_{max} = \sigma_y \cos\phi \cos\lambda \qquad \text{(A.3)}$$

The Schmid factor ($\cos\phi \cos\lambda$) for a {110} <111> slip system, typical for BCC metals, is 0.408, so the applied resolved shear stress to yield a typical 400 nm-diameter pillar is:

τ = 2.2 GPa x 0.408 = 0.90 GPa, which is ~an order of magnitude higher than the stress enhancement caused by solid-solution strengthening. These results imply that solid-solution strengthening is not the sole or dominant cause of the size effect, although it likely elevates the background stress of the HEA alloy by ~680 MPa.

Appendix B. Simulated stress vs. strain for compression FCC and BCC HEAs.

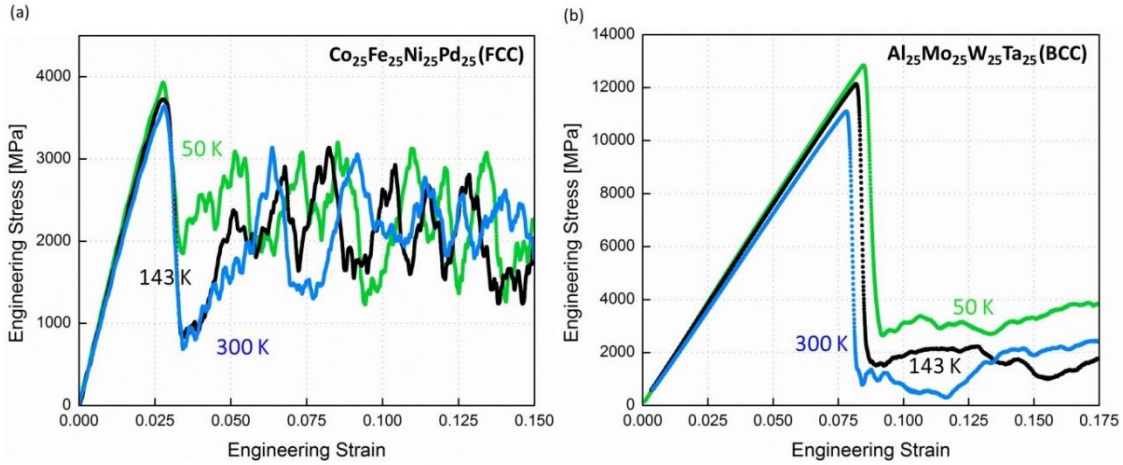

Figure B.1(a) *Simulated stress vs. strain for compression of a representative Co25Fe25Ni25Pd25 FCC HEA oriented along the [324] direction at 50 K, 143 K, and 300 K. The stress at initial failure decreases with increasing temperature while the flow stress is constant across all temperatures.* ***Figure B.1(b)*** *shows simulated stress vs. strain for compression of a representative Al25Mo25W25Ta25 BCC HEA oriented along the [001] direction at 50 K, 143 K, and 300 K.*

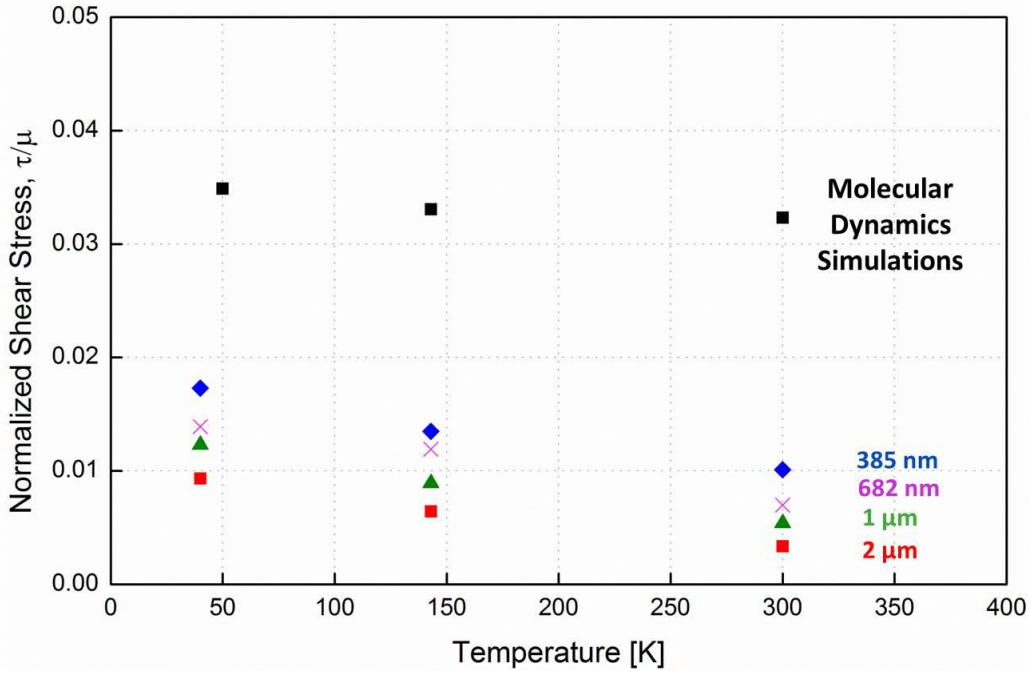

Figure B2 Normalized experimental shear strength of the FCC phase of the $Al_{0.7}$CoCrFeNi HEA compared to MD simulations of a representative FCC HEA. There is a large gap between the experimental data and simulated data consistent with the difference in dominant deformation mechanism.

References

[1] T. H. Courtney, *Mechanical behavior of materials*. Waveland Press, 2005.

[2] D. B. Miracle and R. Darolia, "NiAl and its Alloys," *Struct. Appl. Intermet. Compd.*, p. 20, 2000.

[3] W. R. Wang, W. L. Wang, and J. W. Yeh, "Phases, microstructure and mechanical properties of AlxCoCrFeNi high-entropy alloys at elevated temperatures," *J. Alloys Compd.*, vol. 589, pp. 143–152, 2014.